CHAPTER 4

SYNTHESIS, CHARACTERIZATION, AND MESOMORPHIC BEHAVIOUR OF UNSYMMETRICAL LIQUID CRYSTALLINE DIMERS WITH CYANOBIPHENYL AND AZO/AZOMETHINE NAPHTHALENE

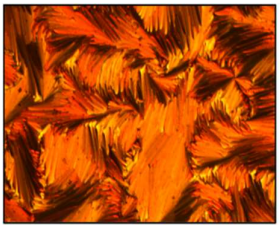

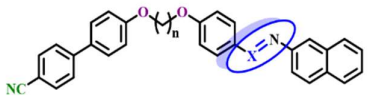

Series V-n: X = -N (Azo linkage)
Series VI-n: X = -CH (Azomethine linkage)
n= 2, 3, 4, 5, 6, 8, 9, 10, 11, 12

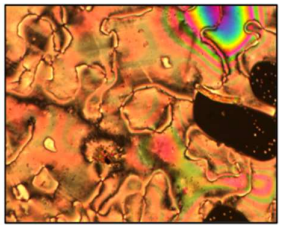

4.1 Introduction

The adaptability of cyanobiphenyl groups allows for facile modifications with polar lateral or terminal groups, enabling the induction of dipole moments and the enhancement of bulk dielectric anisotropy. This capability facilitates the fine-tuning of mesomorphic properties[1–3]. Commercially available liquid crystals such as 5-cyanobiphenyls (5-CB), owing to their dimeric structure, exhibit the desired nematic (N) phase even at room temperature[4]. In particular, the utilization of the nematic (N) and Twist-Bend Nematic (N_{TB}) phases in Liquid Crystal (LC) dimers and other systems has found practical applications, including the selective reflection of light controlled by electric and magnetic fields, along with advancements in the development of tuneable lasers[5].

Over the past decade, significant attention has been directed towards studying the N_{TB} phase which is generally obtained in the dimers containing cyanobiphenyl moiety. Initially proposed in theoretical research[6–8], the N_{TB} phase was later confirmed experimentally in bent LC dimers[9]. This phase is characterized by a helical precession of the director with a typical pitch of several tens of nanometres, which increases with temperature[10–12]. Interestingly, the helical structures observed in the N_{TB} phase share optical and physical properties resembling the layered Smectic phase rather than the typical Nematic phase, thus categorizing the N_{TB} phase as a pseudo-layered phase[13–16]. Despite progress, our understanding of the structure-property relationships in twist-bend nematogens remains at an early stage. Previous research efforts primarily focused on modifying the structures of mesogenic units and their attached terminal groups[17–20]. However, less attention has been paid to variations in spacer length and the chemical composition of links between the spacer and mesogenic units[21–26]. For instance, studies have demonstrated that liquid crystal dimers featuring a flexible spacer with an odd number of methylene groups directly attached to cyanobiphenyl groups, such as 1″,7″-bis(4′-cyanobiphenyl-4-yl) heptane (CB7CB), can form the N_{TB} phase[27]. Subsequent research has reported the formation of the twist-bend nematic phase by odd liquid crystal dimers with ether links to the mesogenic groups[28,29]. Additionally, several bent LC dimers have been identified to exhibit Iso-N_{TB} phase transitions in their single-component systems. Examples include imine-linked dimer homologues with a central propane spacer and terminal methoxy or ethoxy groups[30], propane- and ethylthio-linked

cyanobiphenyl-based dimers[31], and a phosphine-bridged bent cyanobiphenyl dimer [32]. **Fig. 4.1** depicts few examples of unsymmetrical cyanobiphenyl dimers.

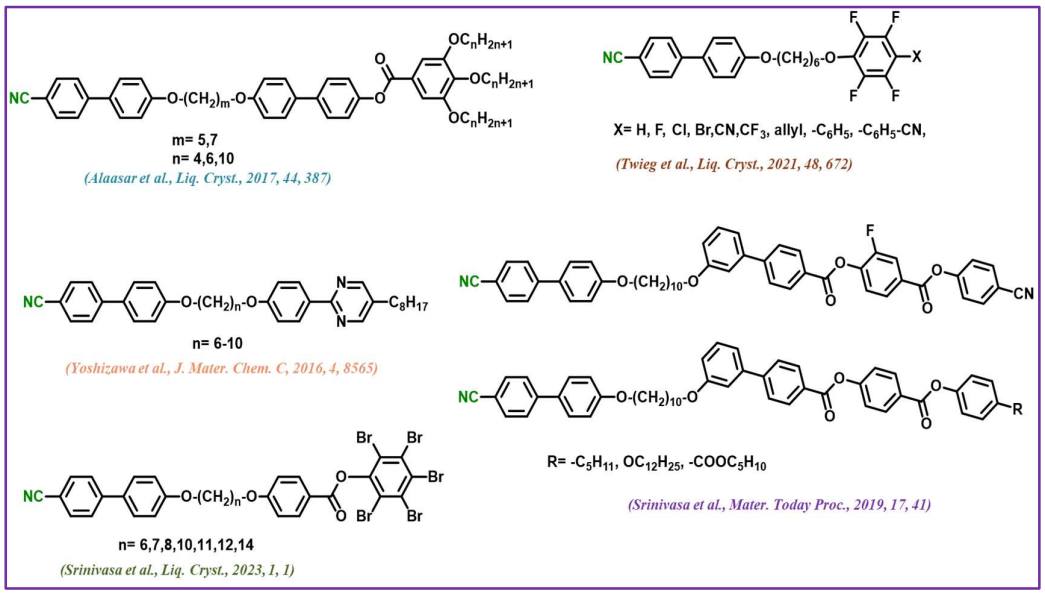

Fig. 4.1: Some examples of Unsymmetrical Cyanobiphenyl dimers

Alaasar and Tschierske have developed a new class of asymmetrical dimeric compounds featuring rigid segments connected by flexible spacers, with trialkoxy chains at one end and a biphenyl moiety capped with a polar cyano group at the other.[33] Yoshizawa and Hirose explored nematic mixtures containing asymmetric dimers composed of phenyl pyrimidine and cyanobiphenyl units linked by a flexible spacer.[34] Srinivasa and Rahman synthesized and characterized calamitic dimers, connecting pentabromophenol to cyanobiphenyl via a flexible alkyl chain, to investigate their mesomorphic properties.[35] They have also reported a novel series of mesogenic dimers, which are anchored by cyanobiphenyl on one end. On the other side, these mesogens are embellished with side arms composed of three to four phenyl rings, interconnected by alkyl spacers and ester functionalities.[36] Twieg et al. efficiently synthesized a series of cyanobiphenyl dimers with varied highly fluorinated aryloxyl terminals.[37]

Liquid crystal dimers incorporating cyanobiphenyl and azo groups represent a promising class of materials. These dimers typically feature two distinct segments: a cyanobiphenyl moiety, which provides a rigid core and imparts nematic behaviour, and an azo group, which introduces additional functionality and influences the mesomorphic properties. **Fig. 4.2** depicts few examples of unsymmetrical cyanobiphenyl dimers with cyanobiphenyl and azo moiety.

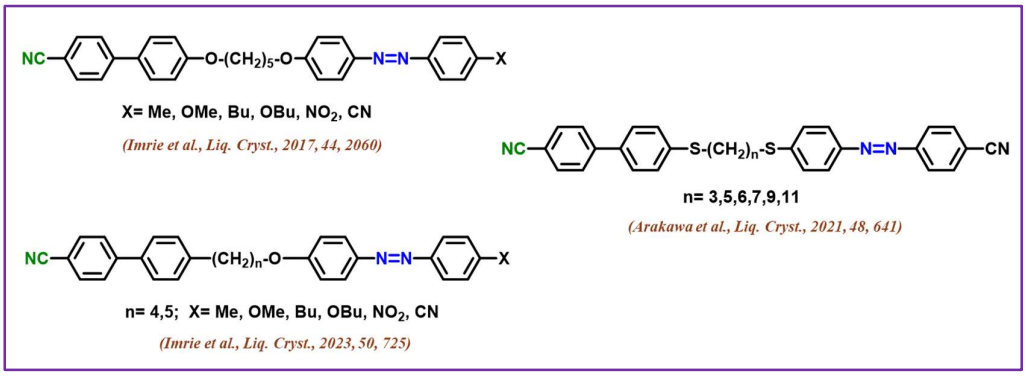

Fig. 4.2: Examples of Unsymmetrical dimers with Cyanobiphenyl and azo moiety

Imrie et al. presented two sets of novel non-symmetric liquid crystal dimers. These dimers exhibited twist-bend nematic (N_{TB}) and nematic (N) phases, with varying terminal substituents. They also introduced a non-symmetric series with sulfur linkages based on 4-cyanoazobenzene and 4-cyanobiphenyl arms, showing supercooled N_{TB} phases.[38–40]

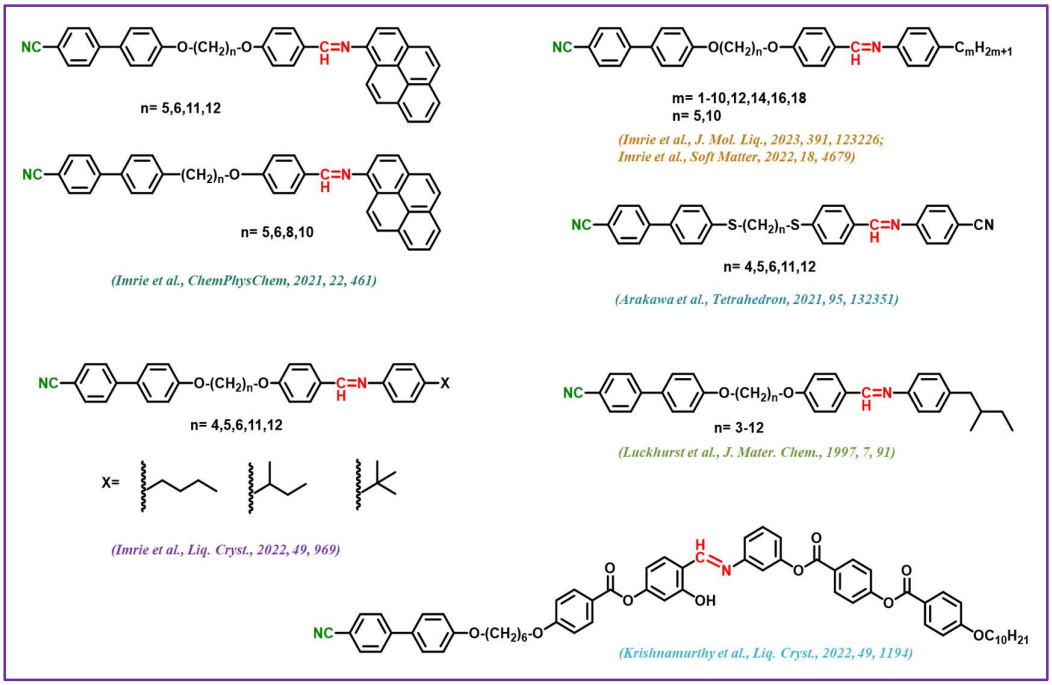

Fig. 4.3: Reports on Unsymmetrical dimers with Cyanobiphenyl and azomethine/ Schiff base moiety

Cyanobiphenyl and Schiff base-containing liquid crystal dimers are notable for their unique molecular structures and mesophase properties. These dimers typically consist of a cyanobiphenyl unit combined with a Schiff base moiety, with a flexible spacer between them. The presence of the cyanobiphenyl group provides rigidity to the

molecule, while the Schiff base adds flexibility and responsiveness to external stimuli. The mesophase properties of these dimers are influenced by various factors, including the length and nature of the spacer, as well as the terminal substituents. The introduction of different functional groups on the terminal ends of the dimers can further modulate their phase behaviour and thermal stability. **Fig. 4.3** shows a few examples of unsymmetrical cyanobiphenyl dimers with cyanobiphenyl and azomethine moiety.

Imrie et al. synthesized pyrene-based liquid crystal dimers with spacers of different lengths, natures, and parities.[41] These dimers included methylene-ether or diether-linked spacers of varying lengths and parities. Luckerhuust et al. examined a liquid crystal dimer, exploring how the length and type of spacer influence its mesophase properties.[42] They varied spacer lengths from n=3 to 12, revealing insights into structure-property relationships and the impact of terminal alkyl chain branching on phase behaviour. Imrie et al. synthesized and studied two sets of nonsymmetric dimers with varying flexible spacers.[43] They found that tert-butyl homologues had higher melting points than sec-butyl or n-butyl substituted dimers, indicating improved packing efficiency due to chain branching. They have expanded the understanding of unsymmetrical liquid crystalline dimers, focusing on varying terminal substituents and spacer lengths.[44,45] Arakawa et al. explored the synthesis and characterization of thioether-linked benzylideneaniline-based liquid crystal dimer homologues, offering insights into the influence of alkylene spacer length on mesophase behaviour.[46] Krishnamurthy et al have reported calamitic-bent core liquid crystalline dimer with cyanobiphenyl moiety.[47]

4.2 Objectives

To deepen our understanding of the relationships between structure and properties in dimers based on Cyanobiphenyl and incorporating naphthalene entities, and to evaluate how different flexible spacers influence their phase behaviour, we synthesized a new series of Calamitic-Calamitic dimers. These dimers contain cyanobiphenyl ether and naphthyl azo/ azomethine groups. The mesogenic units in these compounds are linked via ether bonds, with flexible spacers ranging from 2-6, 8-12 methylene groups in length. The abbreviated name CBOH represents compounds where "CB" denotes the cyanobiphenyl group. In, NpAzOH, the word “NpAz” indicates the rodlike azonaphthyl. In NpAmOH, “NpAm” denotes naphthyl azomethine or Schiff base mesogenic group. ***Series V-n*** dimers are dimers in which one end bears

cyanobiphenylgroup and the other end bears azonaphthyl moiety and ***VI-n*** have azomethine naphthyl moiety at the other end. "n" signifies the length of the flexible spacer for these unsymmetrical dimers.

4.3 Results and Discussion

4.3.1 Synthesis

The synthesis of liquid crystalline dimers from series-***V-n*** and series-***VI-n*** was carried out following a standardized method outlined in **Scheme 4.1** and **Scheme 4.2**, respectively.

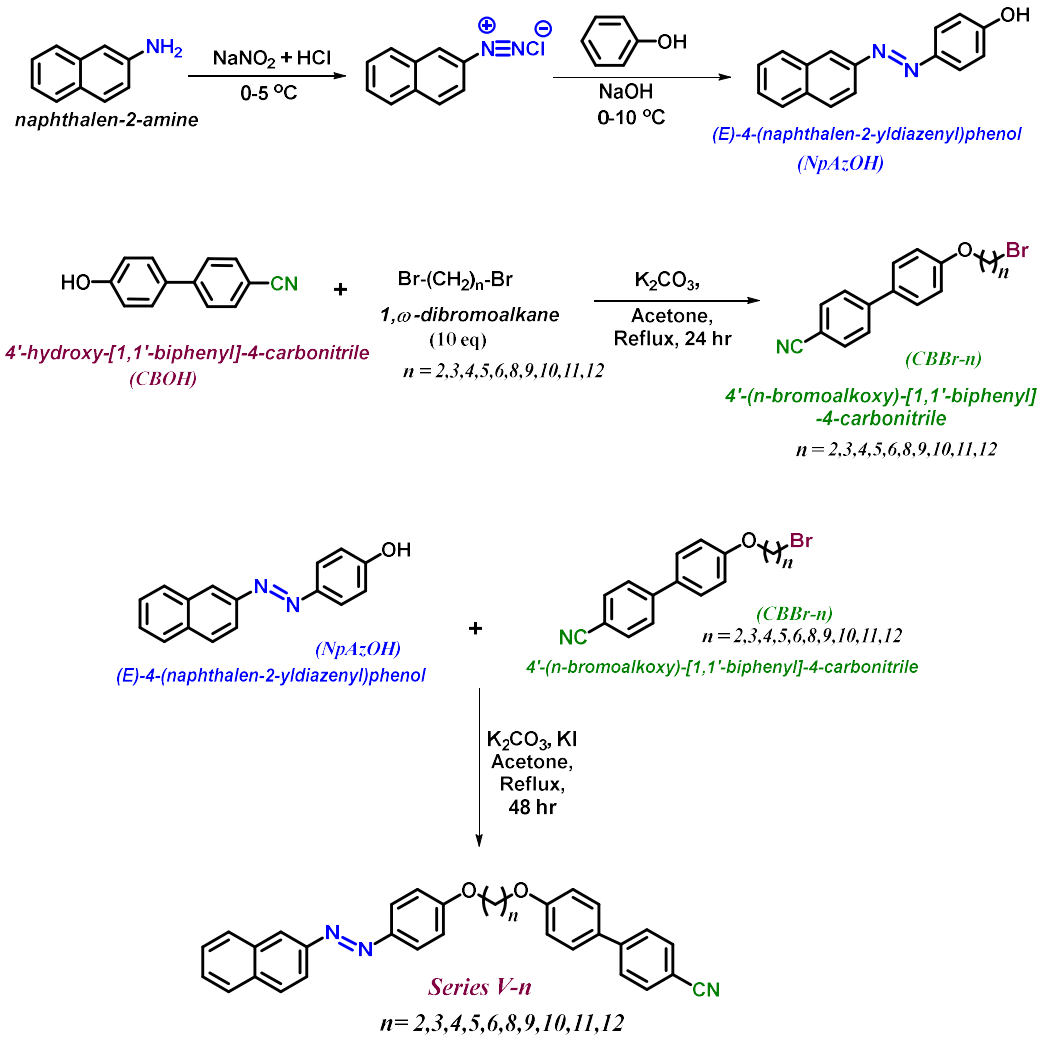

Scheme 4.1: Synthesis scheme for the dimers of *Series V-n*

The preparation of key intermediates including (E)-4-(naphthalen-2-yldiazenyl)phenol (NpAzOH) and (E)-4-((naphthalen-2-ylimino)methyl)phenol (NpAmOH) was detailed in chapter 2A, Section 2A.5.3. CBBr-n was synthesized by refluxing a mixture

containing 4'-hydroxy-[1,1'-biphenyl]-4-carbonitrile (CBOH) and α,ω-dibromoalkanes and potassium carbonate, in acetone for 24 hours, followed by filtration and purification using column chromatography. (detailed in section 4.5) CBBr-n where n is the number of carbons present in the flexible spacer. Subsequently, a Williamson etherification reaction between CBBr-n and NpAzOH/ NpAmOH in the presence of anhydrous potassium carbonate and potassium iodide in acetone led to the formation of ***V-n*** and ***VI-n*** (n = 2-6,8-12).

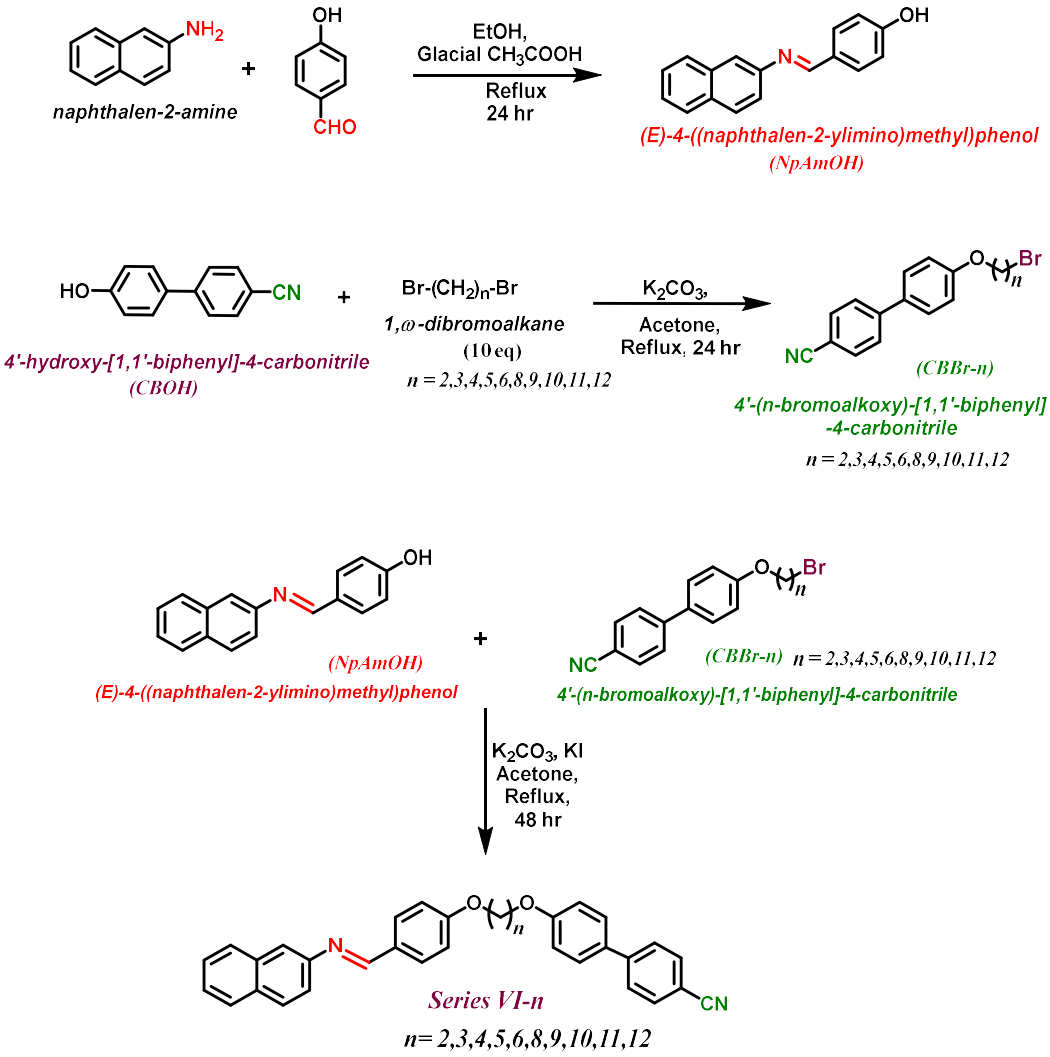

Scheme 4.2: Synthesis scheme for the dimers of series *VI-n*

4.3.2 Chemistry

Through the use of various analytical methods, including FT-IR, ^{1}H NMR, ^{13}C NMR and elemental analysis, the correct structures were verified. The structures of ***V-6*** and ***VI-6*** described in detail as representative of the series. FT-IR spectra of dimer ***V-6***

shows the C-H stretching bands for both alkyl and benzylic groups between 2800-3080 cm^{-1}. The medium intensity bands at the frequency range 1610–1595 cm^{-1} could be attributed to azo (-N=N-) group stretching. Similarly, the aromatic (-C=C-) stretching bands were observed at the frequency range of 1550–1500 cm^{-1}. Medium intensity band for nitrile group (-C≡N) appeared around 2220-2228 cm^{-1}.

The ^{1}H NMR of ***V-6*** showed triplets for at δ 4.35-3.95 ppm for the protons on carbon which is attached to oxygen atom. The other methylene protons were observed as multiplet in between δ 2.50-1.25 ppm. Aromatic protons were appeared in between δ 6.80-8.50 ppm. In the ^{13}C NMR of ***V-6***, signal for methylene protons of flexible spacer were observed around δ 25 to 30 ppm. For the carbon which is directly attached to oxygen signal was found around δ 65-69 ppm. All aromatic carbons were found around δ value of 110-165 ppm. The characteristic peak for the nitrile carbon (-C≡N) appeared around δ 117-119 ppm. The presence of the cyano group (-C≡N) is confirmed by the observation of a distinct peak at δ 121 ppm due to nitrile carbon.

Dimers of ***Series VI-n*** has Imine linkage instead of azo linkage and the rest structure is similar to that of ***Series V-n.*** So, the FT-IR spectra of ***VI-6*** showed the medium intensity bands at the frequency range 1605–1595 cm^{-1} which could be attributed to imine (-CH=N-) group stretching. The imine proton of Schiff base linkage in ^{1}H NMR spectrum was appeared as a singlet at δ 8.4-8.6 ppm. The imine carbon of –CH=N- linkage was observed at δ 161 ppm in ^{13}C NMR spectrum. The mass spectrum was recorded using a Time-of-Flight Mass Spectrometer (TOF-MS) in positive ion mode. The spectrum showcases various peaks, each corresponding to different ionized fragments. The presence of a peak at m/z 525.15 for ***V-6*** and m/z 524.17 for ***VI-6*** as a molecular ion peak $[M+H]^{+}$ confirms the molecular weight of the compounds.

4.3.3 Mesomorphic Behaviour

The phase transition temperatures and mesomorphic behaviour of all the compounds were investigated using Differential Scanning Calorimetry (DSC) while the textures of mesophase were observed using Polarizing Optical Microscope (POM).

4.3.3.1 Differential scanning calorimetry study (DSC)

The thermograms were calculated utilising DSC (DSC-822, Mettler Toledo having Stare software). During both heating and cooling cycles, all phase transitions of the compounds were monitored at a rate of 10 ºC min^{-1}. Transition temperatures (in °C) and associated enthalpy of transition (ΔH) in (kJ mol^{-1}) of dimers ***V-n*** are as presented in

Table 4.1 and dimers ***VI-n*** are as presented in **Table 4.2**. For all of the compounds, DSC curves and POM observations produced distinct transition temperatures and textures, and they exhibited good agreement throughout the numerous heating/cooling cycles. In order to determine the phase transition temperatures and enthalpy values, the DSC analysis of dimers of both the ***Series V-n*** and ***VI-n*** were performed during heating and cooling cycles.

Table 4.1: Transition temperatures (in °C) and associated enthalpy of transition (ΔH) in (kJ mol^{-1}) of *V*-n

Dimer ***V*-n**	n	Transition Temperatures (°C) and ΔH (kJmol^{-1})	
		Heating	Cooling
***V*-2**	2	Cr 250.64 (55.22) N 268.70 (2.57) Iso	Iso 265.38 (-2.52) N 197.05 (-50.99) Cr
***V*-3**	3	Cr 196.98 (39.33) Iso	Iso 168.32 (-0.80) N 150.30 (-36.39) Cr
***V*-4**	4	Cr 208.06 (58.65) N 248.74 (2.91) Iso	Iso 245.97 (-2.70) N 173.14 (-56.58) Cr
***V*-5**	5	Cr 182.76 (45.50) Iso	Iso 170.58 (-1.30) N 132.38 (-37.60) Cr
***V*-6**	6	Cr 178.04 (51.57) N 225.60 (2.48) Iso	Iso 222.11 (-2.21) N 163.38 (-0.44) SmC 147.52 (-49.93) Cr
***V*-8**	8	Cr 162.88 (53.62) N 198.65 (2.98) Iso	Iso 195.65 (-2.96) N 155.87 (-0.94) SmC 138.13 (-55.09) Cr
***V*-9**	9	Cr 146.76 (46.58) N 173.28 (1.69) Iso	Iso 169.93 (-1.40) N 114.73 (-46.19) Cr
***V*-10**	10	Cr 157.40 (45.80) N 194.54 (2.43) Iso	Iso 192.63 (-2.42) N 148.14 (-0.24) SmC 118.33 (-43.27) Cr
***V*-11**	11	Cr 143.93 (42.72) N 169.64 (2.39) Iso	Iso 166.06 (-2.64) N 124.60 SmC (-0.37) 113.08 (-46.08) Cr
***V*-12**	12	Cr 150.58 (41.53) N 185.50 (2.16) Iso	Iso 183.79 (-2.05) N 144.31 (-0.22) SmC 120.64 (-42.69) Cr

SmC: Smectic C; N, Nematic; Iso, Isotropic liquid; Cr, Crystalline solid

Table 4.2: Transition temperatures (in °C) and associated enthalpy of transition (ΔH) in (kJ mol^{-1}) of *VI-n*

Dimer *VI*-n	n	Transition Temperatures (°C) and ΔH (kJmol^{-1})	
		Heating	Cooling
***VI*-2**	2	Cr 221.33 (49.63) N 264.26 (2.47) Iso	Iso 256.97 (-2.41) N 158.74 (-36.16) Cr
***VI*-3**	3	Cr 174.34 (53.52) Iso	Iso 106.82 (-0.32) N 73.15 (-38.24) Cr
***VI*-4**	4	Cr 174.62 (39.37) N 245.35 (2.71) Iso	Iso 241.28 (-2.67) N 140.28 (-36.20) Cr
***VI*-5**	5	Cr 159.37 (28.75) Iso	Iso 148.31 (-0.55) N 96.73 (-14.04) Cr
***VI*-6**	6	Cr 174.30 (32.45) N 223.60 (2.59) Iso	Iso 220.85 (-2.43) N 158.90 (-0.42) SmC 141.99 (-30.39) Cr
***VI*-8**	8	Cr 163.57 (37.99) N 206.71 (2.95) Iso	Iso 203.13 (-2.78) N 147.89 (-0.47) SmC 122.60 (-33.31) Cr
***VI*-9**	9	Cr 128.10 (23.37) N 156.94 (0.83) Iso	Iso 153.78 (-0.82) N 83.51 (-14.19) Cr
***VI*-10**	10	Cr 139.02 (30.88) N 190.19 (2.82) Iso	Iso 186.80 (-2.55) N 131.47 (-0.39) SmC 95.80 (-25.31) Cr
***VI*-11**	11	Cr 128.19 (39.23) N 151.43 (2.24) Iso	Iso 149.11 (-2.23) N 109.98 (-0.64) SmC 72.93 (-28.82) Cr
***VI*-12**	12	Cr 137.53 (32.37) N 173.65 (2.51) Iso	Iso 171.09 (-2.49) N 122.01 (-0.53) SmC 97.76 (-29.98) Cr

SmC: Smectic C; N, Nematic; Iso, Isotropic liquid; Cr, Crystalline solid

The corresponding DSC thermograms for dimers ***V-6*** can be found in **Fig. 4.4 (a).** Cr to N transition occurs at 178.04 °C with an associated enthalpy change (ΔH) of 51.57 kJ mol^{-1} and the subsequent transition to the isotropic liquid state occurs at 225.60 °C with ΔH of 2.48 kJ mol^{-1}. It's worth noting that a reversed phenomenon is observed during the cooling scan, indicating the reversibility of these transitions with extra SmC

phse. Dimer ***V-6*** have shown three exothermic transitions (Iso-to-N, N-to-SmC and SmC-to-Cr) in cooling cycle at 222.11 °C, 163.38 °C and 147.52 °C respectively.

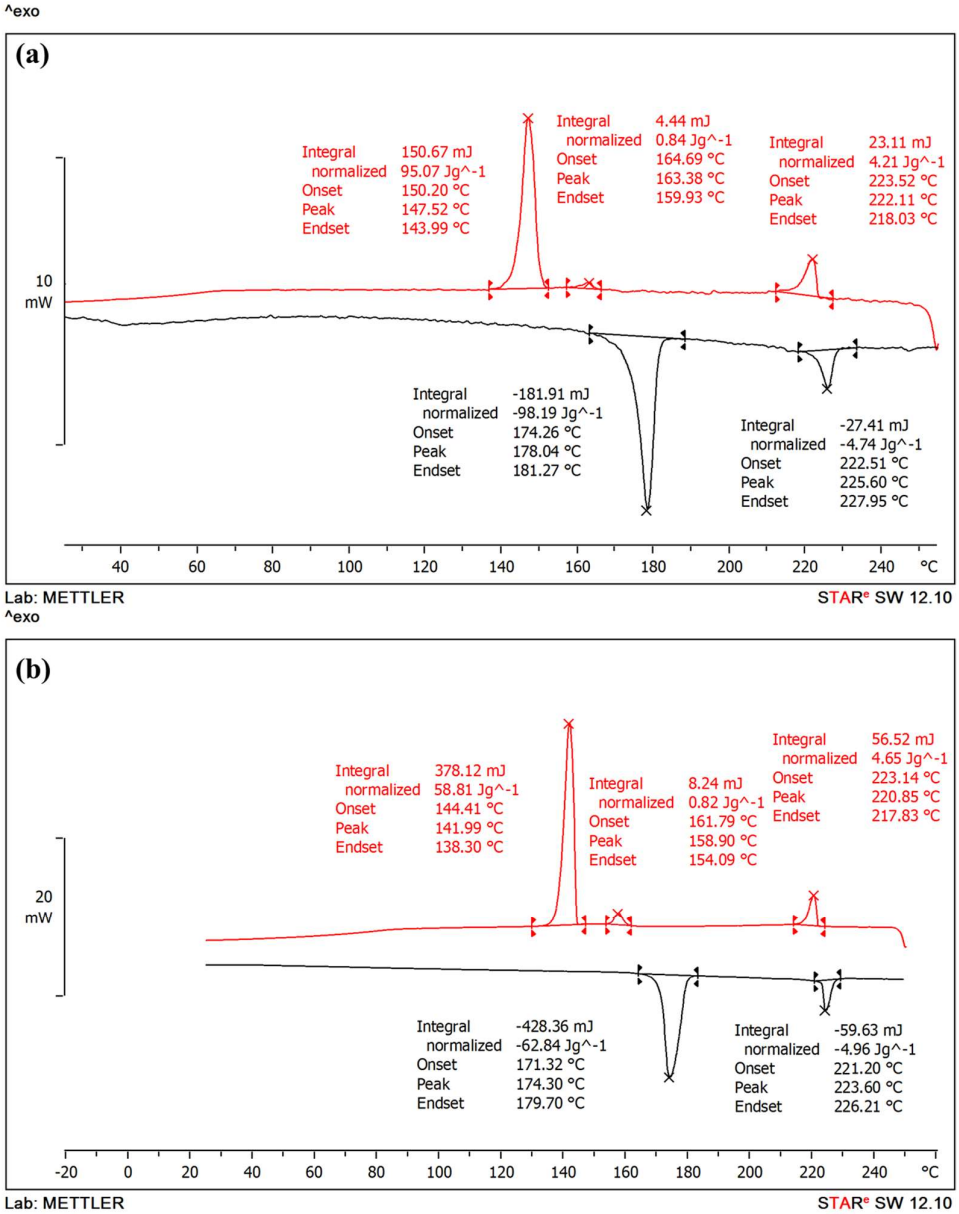

Fig. 4.4: DSC thermogram of Dimers (a) *V-6* and (b) *VI-6*

Almost the majority of dimers of ***Series VI-n*** show enantiotropic nematic (N) and in addition to that some of them show monotropic SmC mesophase. ***VI-6*** shows endothermic transitions Cr-to-N and N-to-Iso at 174.30 °C (ΔH=32.45 kJ mol^{-1}) and 223.60°C (ΔH=2.59 kJ mol^{-1}) on heating and on cooling, it shows three exothermic peaks at 220.85 °C (ΔH=2.43 kJ mol^{-1}), 158.90 (ΔH=0.42 kJ mol^{-1}) and 141.99 °C

(ΔH=30.39 kJ mol^{-1}) for Iso-to-N, N-to-SmC and SmC-to-Cr transitions respectively (**Fig. 4.4b**).

4.3.3.2 Polarising optical microscopy (POM)

To ascertain the liquid crystalline properties of the dimers under investigation, compounds were carefully sandwiched between coverslips and observed under Polarized Optical Microscopy (POM). They were then heated to reach the isotropic state and subsequently subjected to a slow cooling process (i.e., 10 °C min^{-1}) from the isotropic state.

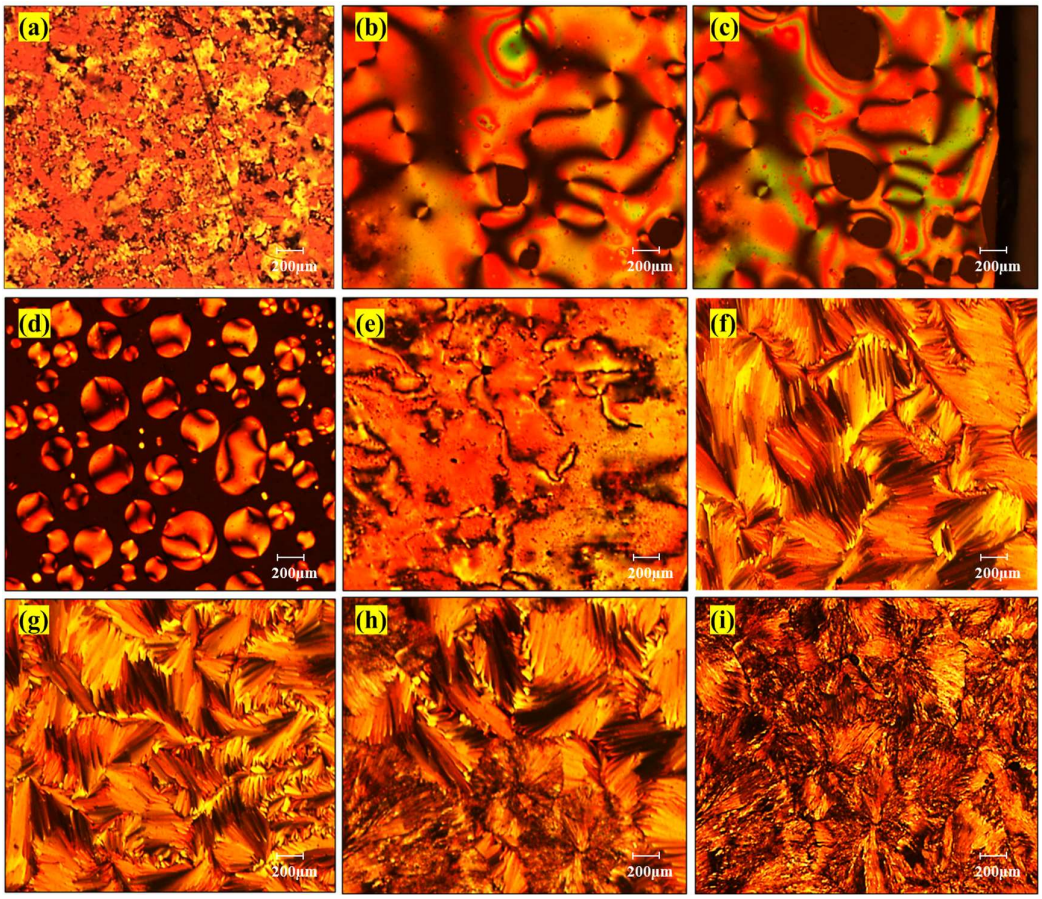

Fig. 4.5: Optical microphotographs of dimer *V-6* (a) Nematic phase at 178 °C during heating, (b) Schlieren texture at 181 °C, (c) N-Iso transition at 225 °C, (d) Nematic droplets at 222 °C upon cooling, (e) Schlieren texture at 218 °C, (f) N-SmC transition at 164 °C, (g) broken focal conic texture of SmC phase at 162 °C, (h) SmC-Cr transition at 148 °C, (i) Crystalline state at 143 °C

Fig. 4.5 displays an optical microphotograph of the nematic phase for dimer ***V-6*** during the first heating and cooling cycle. initially, at 178 °C during heating (**Fig. 4.5a**), a

change in the phase is observed, indicating a transition from a crystalline (Cr) phase to a nematic (N) phase. Subsequently, at 181 °C (**Fig. 4.5b**), a Schlieren texture emerges, followed by a N-Iso transition at 225 °C (**Fig. 4.5c**), marking the shift from a nematic phase to an isotropic (Iso) phase. Upon cooling, at 222 °C (**Fig. 4.5d**), nematic droplets form, indicating the presence of a nematic phase. This is followed by another Schlieren texture at 218 °C (**Fig. 4.5e**). Notably, at 164 °C (**Fig. 4.5f**), a transition from the nematic phase to the smectic C phase occurs, accompanied by a focal conic texture at 162 °C (**Fig. 4.5g**), characteristic of the SmC phase. Further cooling leads to the SmC-Cr transition at 148 °C (**Fig. 4.5h**), transitioning from the smectic C phase to the crystalline phase, as evidenced by the crystalline state observed at 143 °C (**Fig. 4.5i**).

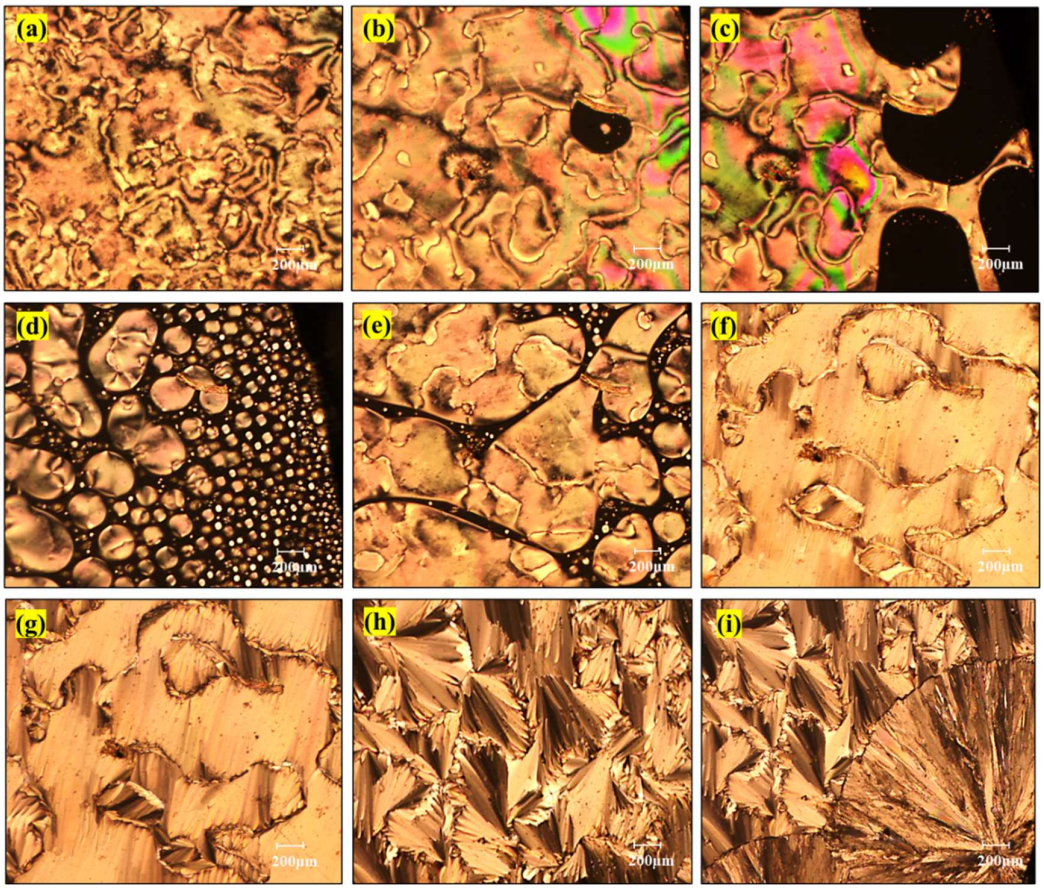

Fig. 4.6: Optical microphotographs of dimer *VI-6* (a) Nematic phase at 174 °C during heating, (b) Schlieren texture at 179 °C, (c) N-Iso transition at 223 °C, (d) Nematic droplets at 220 °C upon cooling, (e) Coalescence of nematic droplets at 217 °C, (f) Schlieren texture transition at 161 °C, (g) N-SmC at 158 °C, (h) focal conic texture of SmC phase at 154 °C, (i) SmC-Cr transition at 142 °C

A sequence of phase transitions in dimer ***VI-***6 was captured by the POM. The major phase changes were depicted by their corresponding microphotographs, elucidated in **Fig. 4.6.** Initially, at 174 °C during heating (**Fig. 4.6a**), the microscope reveals a nematic (N) phase. Subsequently, at 179 °C (**Fig. 4.6b**), a distinct Schlieren texture emerges, marking the transition, followed by a N-Iso transition at 223 °C (**Fig. 4.6c**), indicating the change from a nematic phase to an isotropic (Iso) phase. Upon cooling, at 220 °C (**Fig. 4.6d**), the microscope captures the formation of nematic droplets, a characteristic feature of the nematic phase, and at 217 °C (**Fig. 4.6e**), the coalescence of these droplets. At 161 °C (**Fig. 4.6f**), a transition in the Schlieren texture is observed. Notably, at 158 °C (**Fig. 4.6g**), the transition from the nematic phase to the smectic C (SmC) phase is depicted, accompanied by the appearance of a broken focal conic texture at 154 °C (**Fig. 4.6h**), a characteristic texture of the SmC phase. Finally, at 142 °C (**Fig. 4.6i**), the microscope captures the SmC-Cr transition, indicating the shift from the smectic C phase to the crystalline phase.

4.3.3.3 Structure-property relationship

To visually represent the trends in the properties of liquid crystal dimers described, a line graph can effectively illustrate how various factors, such as spacer chain length and odd-even effects, influence clearing temperatures and phase behaviour.

The x-axis of the graph represents the number of carbons in the flexible spacer chain (n), while the y-axis would depict the transition temperatures (°C). Each data point on the graph corresponds to a specific dimer, with its clearing temperature plotted against its spacer chain length. (**Fig. 4.7**) Firstly, as the number of carbons in the flexible spacer increases, the clearing temperatures or melting points tend to decrease. This phenomenon occurs due to the increased flexibility and decreased intermolecular forces associated with longer spacer chains. As a result, the molecules are less likely to align and exhibit ordered phases at higher temperatures, leading to lower clearing temperatures.

Secondly, odd-membered dimers often exhibit comparatively lower clearing temperatures, a characteristic known as the odd-even effect. This effect arises due to the differing molecular arrangements and intermolecular interactions between odd and even members. Odd-membered dimers, such as those with n=3 and n=5, typically demonstrate monotropic behaviour, particularly in the nematic phase. This behaviour

stems from the asymmetry introduced by the odd number of carbon atoms, which affects the packing and alignment of molecules in the liquid crystal phase.

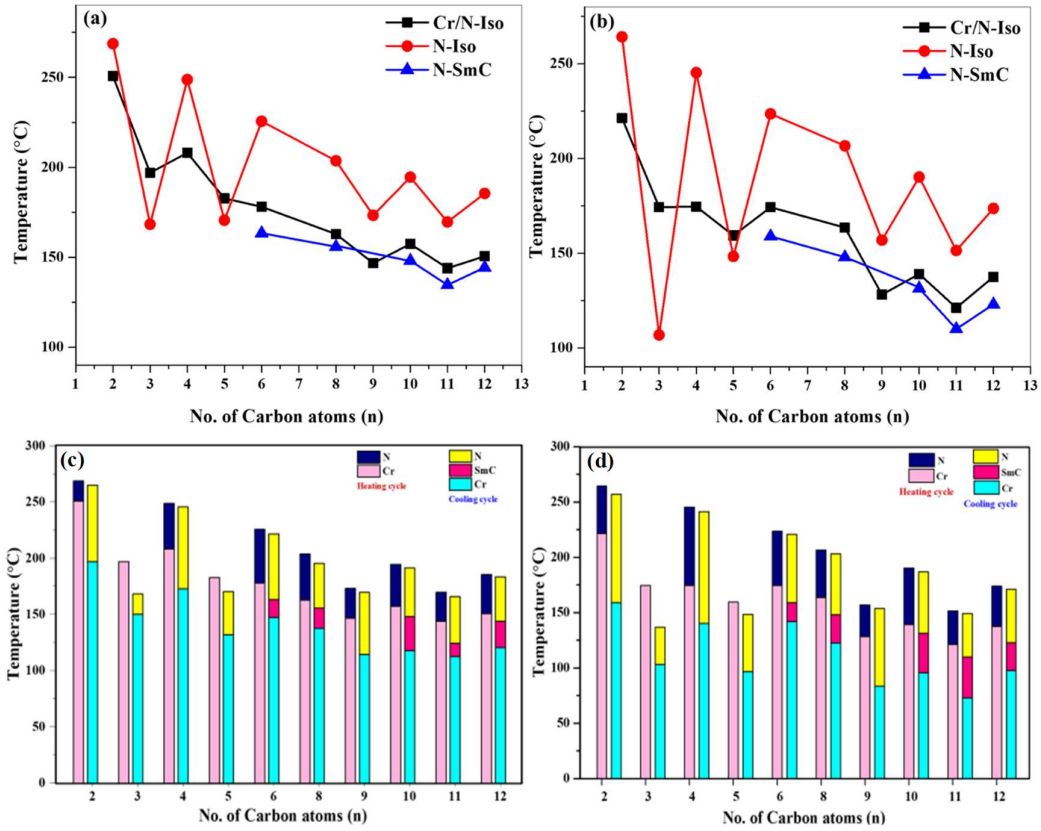

Fig. 4.7: Line graph of the transition temperature vs. no. of carbons in flexible spacer for dimers of (a) *Series V-n* and (b) *VI-n.* Bar graph showing mesophase stability for dimers of (c) *Series V-n* and (d) *VI-n*

Furthermore, in odd-membered dimers, such as those with n=3 and n=5, monotropic behaviour in the nematic phase is observed due to the asymmetry in molecular structure, which hinders the formation of stable ordered phases. On the other hand, for n=9, an enantiotropic nematic phase is observed, indicating reversible transitions between the nematic and isotropic phases. Interestingly, for n=11, both nematic and smectic phases are observed in the cooling cycle as the odd-even effect is not so pronounced for the longer chain.

Lastly, an increase in chain length often leads to the emergence of smectogenic behaviour. Higher-membered dimers, typically ranging from n=6 to n=12, exhibit smectic phases in the cooling cycle, indicative of layered structures with long-range positional order. In contrast, lower-membered dimers, ranging from n=2 to n=5,

predominantly display the nematic phase, as their shorter chains limit the development of layered smectic structures. This trend underscores the pivotal role of molecular structure, particularly chain length, in dictating the phase behaviour of liquid crystal dimers, with longer chains favouring smectic phases and shorter chains favouring nematic phases.

In **Fig. 4.7 (c, d)**, the bar graph illustrates the mesophase stability for dimers belonging to ***Series V-n*** and ***VI-n***. Mesophase stability refers to the propensity of a liquid crystal material to maintain its ordered mesophase, such as the nematic or smectic phase, over a range of temperatures during both heating and cooling cycle.

From **Fig. 4.7 (c, d)**, it is evident that ***V-n*** dimers display greater thermal stability (N-Iso transition temperature) when compared to ***VI-n*** dimers. Moreover, it illustrates that the mesophase stability of the dimers is more pronounced during the cooling cycle as opposed to the heating cycle, suggesting that the ordered phases are more persistent upon cooling. Additionally, it is observed that azomethine dimers exhibit comparatively higher nematic mesophase length in comparison to azo dimers, indicating a difference in the nematic mesophase length between these two types of dimers. (**Fig. 4.8**)

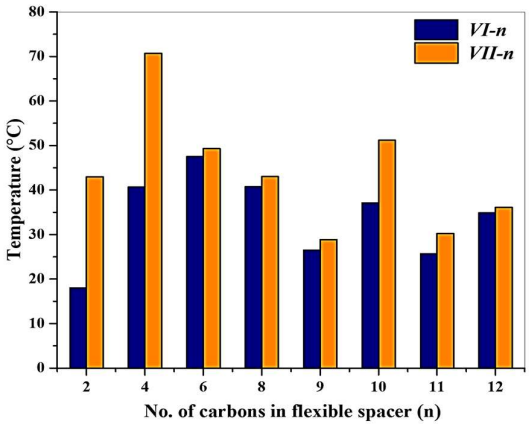

Fig. 4.8: Bar graph showing mesophase length of dimers in heating cycle for *Series V-n* and *VI-n*

The variations in transition temperatures between ***Series V-n*** and ***VI-n*** can be ascribed to the structural disparities inherent in the azo and azomethine linkages present in the dimers. In ***Series V-n***, the inclusion of the central –N=N– linkage fosters a more coplanar molecular arrangement, facilitating efficient packing and yielding slightly higher thermal stabilities. This coplanarity allows molecules to organize themselves more closely. Conversely, Series ***VI-n***, containing the central –CH=N– linkage, exhibits

a less coplanar configuration, hindering efficient packing and resulting in lower thermal stabilities compared to ***Series V-n***.

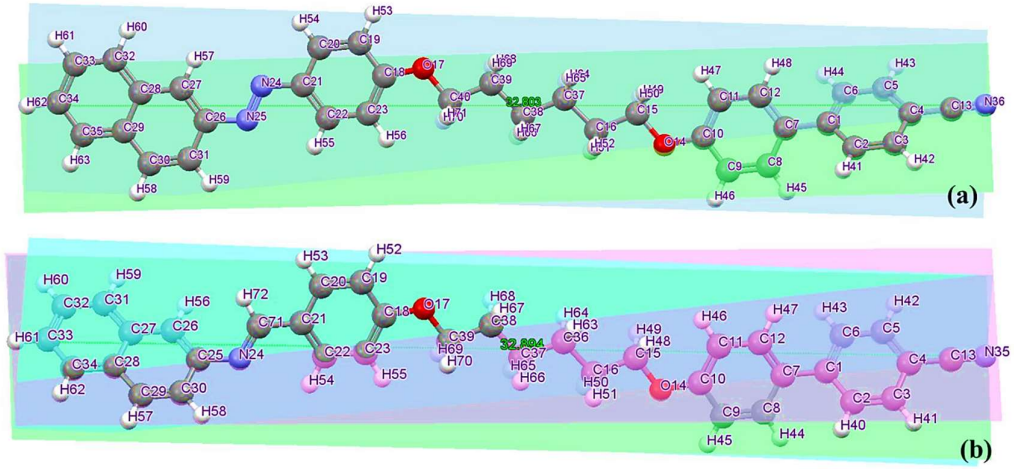

Fig. 4.9: Geometrical difference between the structure for (a) *V-6* and (b) *VI-6* shown by its planar structure

Moreover, the thermal stability of a mesophase significantly influences mesomorphic behaviour in relation to chemical constitution. Structural geometry depicted in **Fig. 4.9** reveals that in Series ***VI-n*** (***VI-6***), the naphthalene ring is slightly tilted and resides in different planes, diminishing packing efficiency and leading to lower clearing temperatures compared to ***Series V-n.*** The relatively high biaxiality associated with naphthalene-based units likely contributes to the observed low enthalpy values.

Table 4.3 presents an outline of transition temperatures (in °C) and comparative geometry data, contrasting the ***VI-n*** series with a closely related series with comparable structures.

The dimers within series ***VI-n*** exhibit both enantiotropic (n=6,11,12) and monotropic (n=5) mesogenic behaviour. Particularly, ***VI-5*** demonstrates monotropic mesophase behaviour similar to ***CBO5O.Py*** from series **A**. Comparing with series **A**, dimers in our current series demonstrate comparatively higher thermal and mesophase stability.

Table: 4.3 Comparison of transition temperatures (°C) of present series *VI-n* and structurally related series A[48]

No. of C in chain (n)	Series A (CBOnO.Py)		Series *VI-n*	
	Transition Temperatures (°C)			
	$T_{Cr\text{-}N/Iso}$	$T_{N\text{-}Iso}$	$T_{Cr\text{-}N/Iso}$	$T_{N\text{-}Iso}$
5	152	(148)	159.37	(148.31)
6	172	208	174.30	223.60
11	149	151	128.19	151.43
12	126	167	137.53	173.65

N, Nematic; Iso, Isotropic liquid; Cr, Crystalline solid; (_) denotes a monotropic transition.

The main difference between ***CBOnO.Py*** and series ***VI-n*** lies in their aromatic core composition, with ***VI-n*** containing a naphthalene moiety and series **A** featuring a pyrene ring. Here length to breadth ratio will increase for the dimers of series A due to broadening of molecule. Whereas in present series it only contains naphthalene ring which contribute collectively to enhanced thermal and mesophase stability within our present series. In our current study, both series of dimers exhibit small nematic-isotropic enthalpies for even-membered dimers. This trend mirrors findings from pyrene-based dimers, where similar or even lower enthalpy values were observed.

4.3.4 Thermogravimetric analysis (TGA)

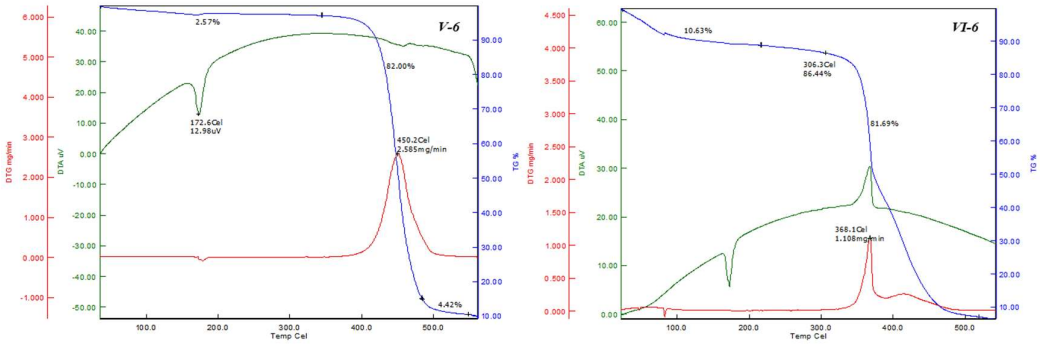

Fig. 4.10: TGA graph for *V-6* and *VI-6*

The TGA analysis reveals a substantial mass loss of 80-82% at 450.2 °C for ***V-6*** and at 368.1 °C for ***VI-6***, indicating the main thermal decomposition of the compound. (**Fig. 4.10**) This is further corroborated by the DTG curve, which shows a peak corresponding to this decomposition. Notably, the ***V-n*** series dimers exhibit greater thermal stability compared to those in the ***VI-n*** series.

4.3.5 Computational studies

Density Functional Theory (DFT) was applied in our study, utilizing Becke's three-parameter hybrid functional (B3LYP) in conjunction with the 6-31 G basis set level. The computational framework employed Gaussian 09 software to conduct theoretical calculations essential for understanding molecular properties, such as optimized structures and vibrational frequencies. We initiated the process by optimizing the energy of various conformations until a minimum-energy geometrical structure was obtained. Subsequently, this optimized structure served as the basis for calculating frequencies and thermodynamic properties.

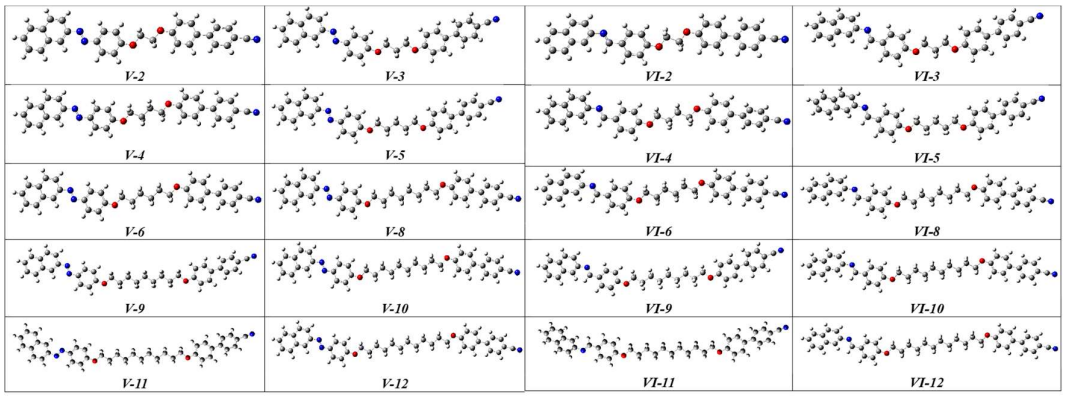

Fig. 4.11: Optimized molecular structures of dimers of *Series V-n* and *VI-n*

Our depiction of molecular structures adheres to a specific color scheme: carbon atoms are represented in grey, nitrogen in blue, oxygen in red, and hydrogen in white. These atoms are connected via sigma and pi bonds, thus forming the intricate three-dimensional arrangements of the molecules under investigation. For visualization purposes, **Fig. 4.11** illustrates the optimized molecular structures for dimers across both series, providing valuable insights into their structural characteristics as determined through our DFT-based computational approach. **Table 4.4** illustrates the stabilization energy or energy minima values (measured in Hartree) for each dimer. It is evident that the energy minima decreases with the increasing number of carbons in the flexible

spacer chain of the dimers. When comparing the two series, it is observed that the dimers in ***Series V-n*** demonstrate higher energetic stability compared to those in Series ***VI-n***.

Table 4.4: Quantum mechanical descriptors

Dimer	*Energy minima (Hartree)*	*HOMO*	*LUMO*	*I* (eV)	*A* (eV)	*ΔE* (eV)	*η*	*δ*	*χ*	*ω*
				Series V-n						
V-2	-1509.842	-0.209	-0.083	5.678	2.251	3.427	1.714	0.584	3.965	4.586
V-3	-1549.160	-0.208	-0.082	5.648	2.225	3.423	1.712	0.584	3.936	4.526
V-4	-1588.478	-0.206	-0.081	5.615	2.193	3.422	1.711	0.584	3.904	4.454
V-5	-1627.795	-0.206	-0.080	5.597	2.177	3.420	1.710	0.585	3.887	4.418
V-6	-1667.111	-0.205	-0.079	5.578	2.159	3.419	1.709	0.585	3.869	4.378
V-8	-1745.745	-0.204	-0.079	5.556	2.139	3.417	1.708	0.585	3.847	4.332
V-9	-1785.061	-0.203	-0.077	5.548	2.119	3.429	1.714	0.583	3.833	4.285
V-10	-1824.378	-0.204	-0.078	5.541	2.125	3.416	1.708	0.585	3.833	4.301
V-11	-1863.695	-0.203	-0.077	5.536	2.104	3.432	1.716	0.582	3.820	4.252
V-12	-1903.011	-0.203	-0.078	5.532	2.116	3.416	1.708	0.586	3.824	4.280
				Series VI-n						
VI-2	-1493.835	-0.204	-0.060	5.556	1.622	3.933	1.967	0.508	3.589	3.275
VI-3	-1533.152	-0.203	-0.059	5.534	1.599	3.935	1.968	0.508	3.566	3.232
VI-4	-1572.470	-0.202	-0.058	5.507	1.576	3.932	1.966	0.509	3.542	3.190
VI-5	-1611.787	-0.202	-0.057	5.493	1.562	3.932	1.966	0.509	3.528	3.165
VI-6	-1651.104	-0.201	-0.057	5.478	1.550	3.928	1.965	0.509	3.514	3.144
VI-8	-1729.737	-0.201	-0.056	5.459	1.534	3.925	1.963	0.510	3.497	3.115
VI-9	-1769.054	-0.200	-0.056	5.453	1.528	3.924	1.962	0.509	3.491	3.104
VI-10	-1808.371	-0.200	-0.056	5.447	1.524	3.923	1.962	0.510	3.486	3.097
VI-11	-1847.687	-0.200	-0.056	5.444	1.523	3.920	1.960	0.510	3.484	3.096
VI-12	-1887.004	-0.200	-0.056	5.439	1.518	3.921	1.961	0.510	3.478	3.085

I, Ionization Potential; *A*, Electron Affinity; *ΔE*, Energy gap; *η*, Global hardness; *δ*, Global softness; *χ*, Chemical reactivity; *ω*, Electrophilicity index

4.3.5.1. Frontier molecular orbitals (FMOs) and Molecular electrostatic potential (MEP)

The electronic characteristics, specifically the energies of the Highest Occupied Molecular Orbital (HOMO) and the Lowest Unoccupied Molecular Orbital (LUMO), were determined for the optimized structures. An analysis of the frontier molecular

orbitals (FMOs) was conducted to forecast the chemical reactivity and stability of the compounds. To assess the potential for electron transfer in the compounds, the energy gap between the HOMO and LUMO was computed. In ***Series V-n***, the HOMO and LUMO are primarily constituted by the π-orbitals from the naphthyl ring, with a minor contribution from the azo linker (-N=N-) (**Fig. 4.12**). In Series ***VI-n*** dimers, the HOMO is mainly localized in the π-orbitals of the naphthyl unit, with a smaller contribution from the π-orbitals of the -CH=N- linker. The LUMO is associated with the corresponding anti-bonding orbital of the biphenyl ring containing a cyano substituent. There is a slight difference in the HOMO-LUMO energy values, with Series ***VI-n*** dimers showing marginally higher values than ***Series V-n***. Additionally, the length of the flexible spacer does not impact the spatial distribution of electron densities within the molecular orbitals (MOs).

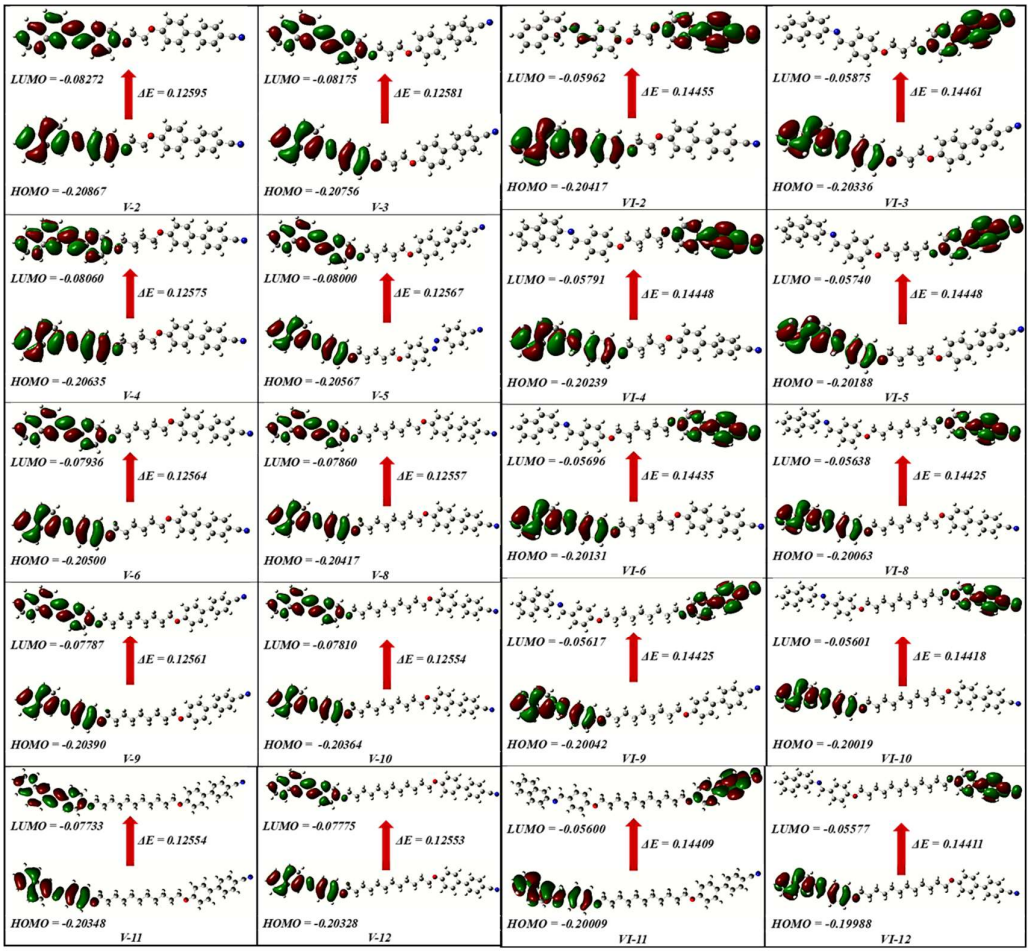

Fig. 4.12: FMOs for the dimers of *Series V-n* and *VI-n* (Values of HOMO, LUMO and ΔE are in a.u.)

Extending the length of the flexible spacer does not significantly affect the energy gap, as demonstrated in **Table 4.4**. This consistency in the energy gap can be explained by the high concentration of charge density around the cores of the dimers, as shown in **Fig. 4.12**. Notably, the dimers studied displayed almost identical values for parameters such as chemical hardness (η) and softness (δ), regardless of the length of the flexible spacer chains.

Table 4.5: Optical properties and dimensional parameters of the dimers

Dimer	*Dipole Moment μ (debye)*	*Polarizability α (a.u.)*	*Length (L) Å*	*Width (D) Å*	*Aspect ratio (L/D)*	*Mesophase range (ΔT) °C*
			Series V-n			
V-2	5.202	439.038	27.798	5.569	4.991	18.06
V-3	4.987	449.331	28.340	7.779	3.643	-
V-4	5.098	461.590	30.295	5.569	5.439	40.68
V-5	4.922	472.091	30.882	7.776	3.971	-
V-6	5.045	484.010	32.803	5.568	5.891	47.56
V-8	5.011	506.503	35.323	5.567	6.345	40.77
V-9	4.867	517.544	36.008	7.689	4.683	26.52
V-10	4.991	529.138	37.847	5.565	6.800	37.14
V-11	4.615	540.735	38.391	7.625	5.034	25.71
V-12	4.978	551.819	40.376	5.563	7.257	34.92
			Series VI-n			
VI-2	4.445	423.041	27.906	4.998	5.583	42.93
VI-3	4.709	433.422	28.369	7.149	3.968	-
VI-4	4.388	445.647	30.399	4.997	6.083	70.73
VI-5	4.720	456.199	30.902	7.148	4.323	-
VI-6	4.355	468.032	32.894	4.997	6.582	49.3
VI-8	4.336	490.603	35.403	4.991	7.093	43.14
VI-9	4.713	501.649	36.022	7.143	5.042	28.84
VI-10	4.324	513.251	37.921	4.989	7.600	51.17
VI-11	3.583	524.961	38.402	7.140	5.378	30.24
VI-12	4.315	535.930	40.445	4.986	8.111	36.12

In the series of dimers, each molecule has a dipole moment ranging from approximately 4.6 to 5.2 Debye (**Table 4.5**). Typically, molecular interactions significantly impact dipole moments. Notably, odd-membered dimers in ***Series V-n*** have lower dipole moments than even-membered dimers, while the opposite is true for Series ***VI-n***. **Table 4.5** also shows the polarizability values for both ***Series V-n*** and ***VI-n***, revealing a significant correlation between polarizability and the length of the flexible spacer.

As the chain length increases, polarizability also increases proportionally. The odd-membered dimers have a greater molecular breadth due to their bent shape, resulting in lower aspect ratio values. Dimers with tetramethylene and hexamethylene spacers exhibit a higher mesophase range compared to other dimers. Furthermore, odd-membered dimers do not display liquid crystal properties during the heating cycle.

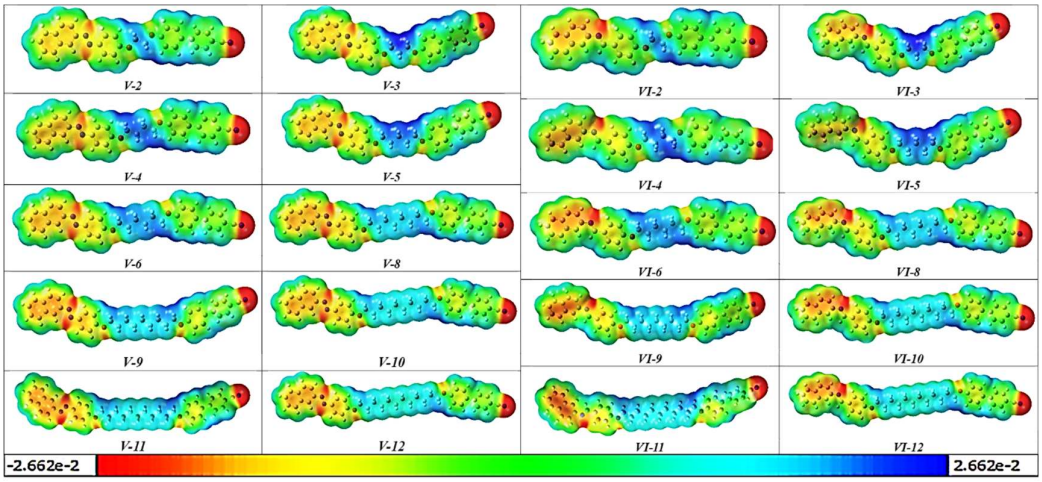

Fig. 4.13: MEP contours of the dimers of *Series V-n* and *VI-n*

The molecular electrostatic potential (MEP) surface was generated to visualize electron density distribution, aiding in the prediction of electrophilic and nucleophilic attack sites. Additionally, mesophase formation in these compounds is impacted by molecular packing arrangements, which are likely influenced by charge distribution. In this study, the charge distribution was analyzed using the DFT/B3LYP method with a 6-31G basis set. **Fig. 4.13** illustrates the MEP surface, which is crucial for understanding these interactions. Electrophiles are attracted to regions with higher negative charge (red areas), whereas nucleophiles are drawn to regions with less negative charge (blue areas). Red regions are mainly located around the cyano groups and nitrogen atoms of azo groups, while blue regions typically appear along the carbon chain of the flexible

spacer. The charge separation within the dimers promotes end-to-end interactions, leading to the formation of a nematic mesophase with limited lateral ordering.

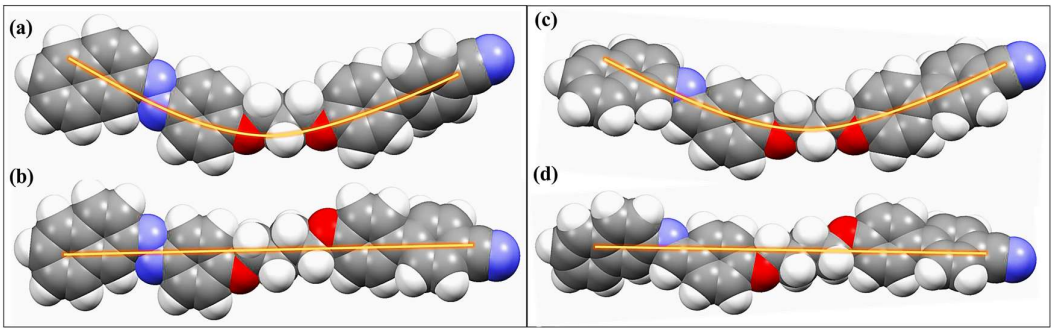

Fig. 4.14: Space-filling model of (a) *V-3* (Odd membered dimer) and (b) *V-4* (even membered) (c) *VI-3* (d) *VI-4* showcasing the spacer in the all-trans conformation.

The distinct odd-even effects seen in the transitional properties of dimers are driven by their molecular configuration, which depends on the number of atoms linking the mesogenic units. Dimers with an even number of atoms usually adopt a linear shape, while those with an odd number of atoms generally have a bent shape. This structural difference affects how well they fit into the molecular arrangement in the nematic phase, leading to variations in their transitional behaviours, such as changes in nematic-isotropic transition temperatures and melting points. (**Fig. 4.14**).

4.3.5.2 Vibrational studies

The calculated vibrational frequencies of the compounds were compared with the experimental values obtained from FT-IR spectra. The theoretical frequencies showed good agreement with the experimental values, confirming the accuracy of the DFT calculations. The obtained geometries were further confirmed by the vibrational frequency analysis, which yielded no imaginary frequency. Fig. 4.15 depicts the plot which shows the comparison of the vibrational frequency obtained from the experiment and calculated at B3LYP-6-31G level theory for dimers ***V-6*** and ***VI-6***. The vibrational modes of phenyl rings and naphthalene rings include C-H stretching vibrations (3000-2800 cm^{-1}), out-of-plane and in-plane C-H bending vibrations (850-700 cm^{-1}), and -C=C- stretching vibrations (1570-1500 cm^{-1}), with good agreement between theoretical and experimental values. C-C stretching vibrations are observed between 1450-1300 cm^{-1}, while in-plane C-C bending vibrations occur around at 1010-1030 cm^{-1}. Vibrations at 1600 cm^{-1} indicate a -N=N- double bond. -CH=N- vibrations (imine

groups) are seen at 1600 cm^{-1}. The cyano group (nitrile) exhibits C-N stretching vibrations at 2220 cm^{-1}. Ether groups display C-O stretching vibrations (1260-1200 cm^{-1}) and O-C-O bending vibrations (720-640 cm^{-1}) in line with theoretical calculations.

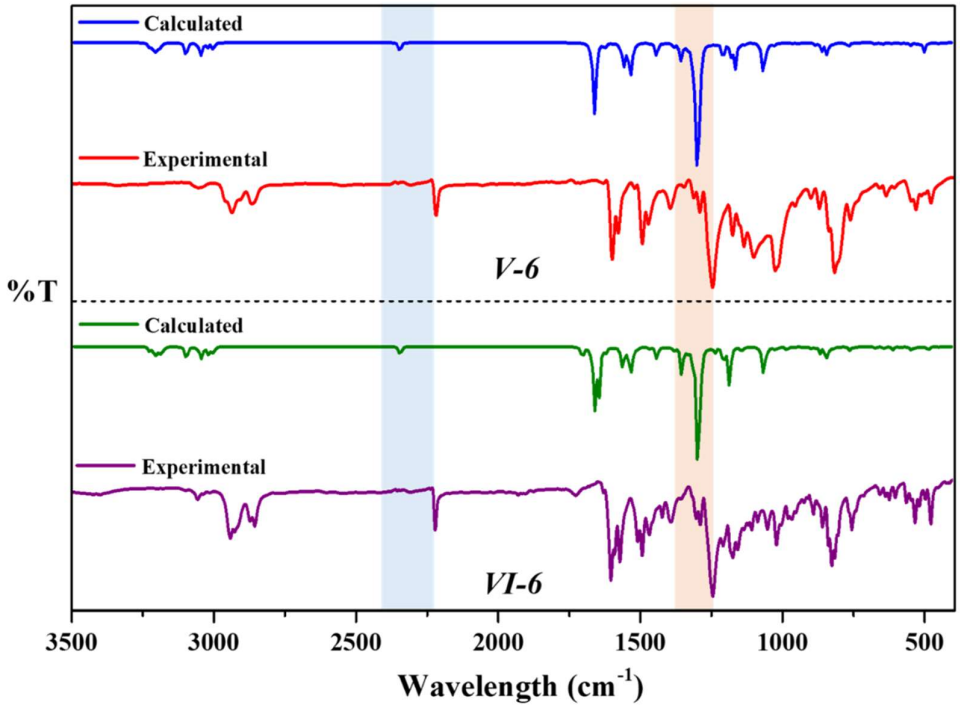

Fig. 4.15: Comparison of the vibrational frequency obtained from the experiment and calculated at B3LYP-6-31G level theory (gas phase) for dimers *V-6* and *VI-6*

4.3.6 Photo switching behaviour

The absorption spectra for *trans-cis* photoisomerization and *cis-trans* thermal back relaxation were recorded for the solution. The studies of the said compounds were carried out in a dark room at room temperature (27 ±1ºC). The compounds were dissolved in chloroform with a fixed concentration of ~1.0×10^{-5} mol L^{-1}. The prepared samples were taken in a quartz cuvette (Optical length; 1cm) and placed in the sample holder, it was then irradiated with UV light of intensity ~1 mW/cm^2 using an OMNICURE series 2000 UV light source equipped with a heat filter to prevent heat radiation from the source and 365nm UV filter. The absorption spectra of the compounds were first recorded under UV irradiation at various exposure times, and subsequently, the absorption spectra of compounds undergoing thermal back relaxation were recorded at various time intervals.

The influence of different terminal groups (***V-2*** to ***V-12***) and varying chain lengths (n=2-12) on the photo-switching behaviour of azobenzene molecules was investigated. The absorption spectra of all compounds before UV illumination showed a prominent peak around 358-361 nm due to the symmetry-allowed π-π* transition with respect to the azo moiety and a weak peak at 450 nm due to symmetry-forbidden n-π* transition. However, after UV irradiation, the compounds undergo *trans-cis* photoisomerization and the absorbance maxima around 365 nm corresponding to *trans-cis* conversion decreased gradually with a slight increase in the peak at ~450 nm observed. One can see from **Table 4.6** and **Fig. 4.16** that all the compounds had a similar photo saturation time of ~45-50 seconds, indicating that it depends only on the UV intensity and is not influenced by the terminal groups or flexible spacer chain length. The changes in the absorption peaks due to UV exposure are illustrated in **Fig. 4.16a-j** and the peak absorbance values were plotted as a function of time in **Fig. 4.16k.**

Table 4.6: Showing the *E-Z* and *Z-E* relaxation along with conversion efficiency.

Dimer	*Time for E-Z in seconds (~)*	*Time for Z-E in minutes*	*CE (%)*
V-2	49	600	88.70 %
V-3	50	660	86.55 %
V-4	50	720	95.19 %
V-5	49	660	96.09 %
V-6	48	600	94.23 %
V-8	49	660	94.79 %
V-9	47	600	94.77 %
V-10	49	720	95.01 %
V-11	48	600	96.13 %
V-12	50	660	95.85 %

One can observe from the **Table 4.6** that all the compounds show similar conversion efficiency rate of 88-95% indicting the high sensitivity for the molecules under UV irradiation. Out of all ***V-11*** showing the highest conversion efficiency of 96% and ***V-2*** among the lowest conversion efficiency of 88%.

Within 50 seconds of illumination, entire trans molecules converted to cis molecules indicating high conversion efficiency in such systems. The extent of photoisomerization

can be determined by calculating the photo-conversion efficiency as given by Equation 1.

$$PCE = \frac{A(t_0) - A(t_\infty)}{A(t_0)} \times 100 \quad (1)$$

Here $A(t_0)$ is the initial absorbance (before UV exposure) and $A(t_\infty)$ is the final absorbance (after UV exposure).

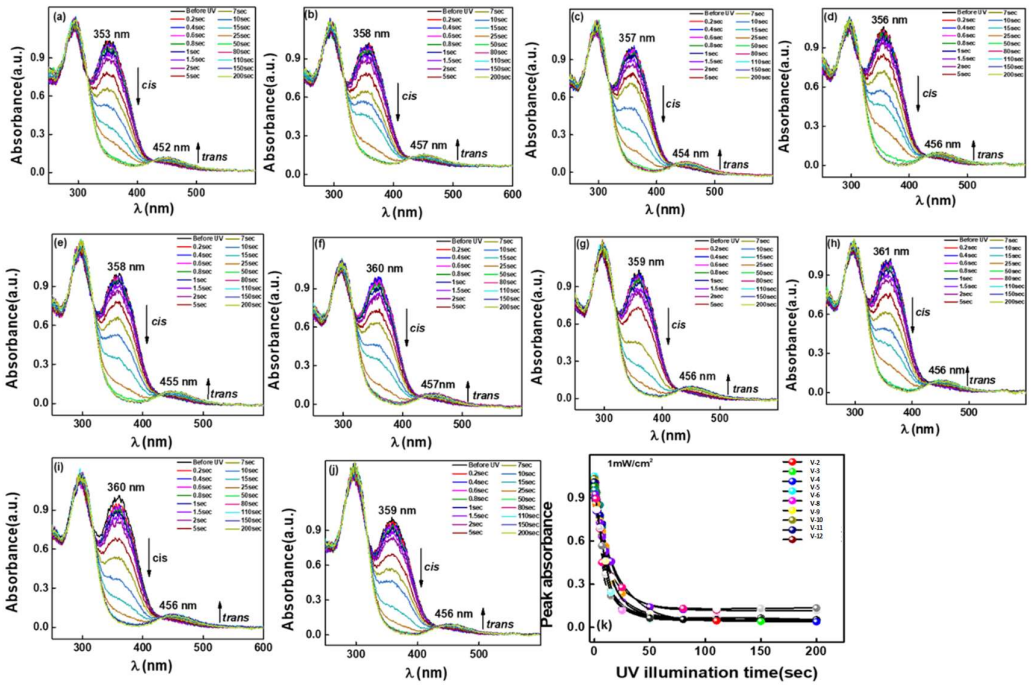

Fig. 4.16: Absorption spectra with respect to UV exposure time for: (a) *V-2* (b) *V-3* (c) *V-4* (d) *V-5* (e) *V-6* (f) *V-8* (g) *V-9* (h) *V-10* (i) *V-11* (j) *V-12* (k) Peak absorbance picked up from Fig. (a) to (j) v/s UV irradiation time. Intensity of light is 1 mW/cm^2 and heat filter is inserted between solution and the light to avoid any heat effect arising from the UV light.

When the photo-induced saturation condition is reached, the conformations, depending on the molecule structure, remain in the same condition for a reasonable amount of time. However, the conversion from *cis* to *trans* can be induced by irradiating with white light of 450 nm wavelength or by keeping in the dark which is also called as thermal back relaxation. Since the recovery of the conformation without irradiating white light is crucial for optical storage devices, thermal back relaxation is recommended.

To evaluate the back-relaxation time without the impact of any external light source, the absorbance spectra for solutions were recorded in the dark, without the influence of any external light. **Fig. 4.17a-j** demonstrate the changes in absorbance that occur during the thermal back-relaxation process, and the peak absorbance values are plotted as a function of time in **Fig. 4.17k**. The impact on the thermal back relaxation time could be attributed to the presence of terminal group and spacer length of the dimers.

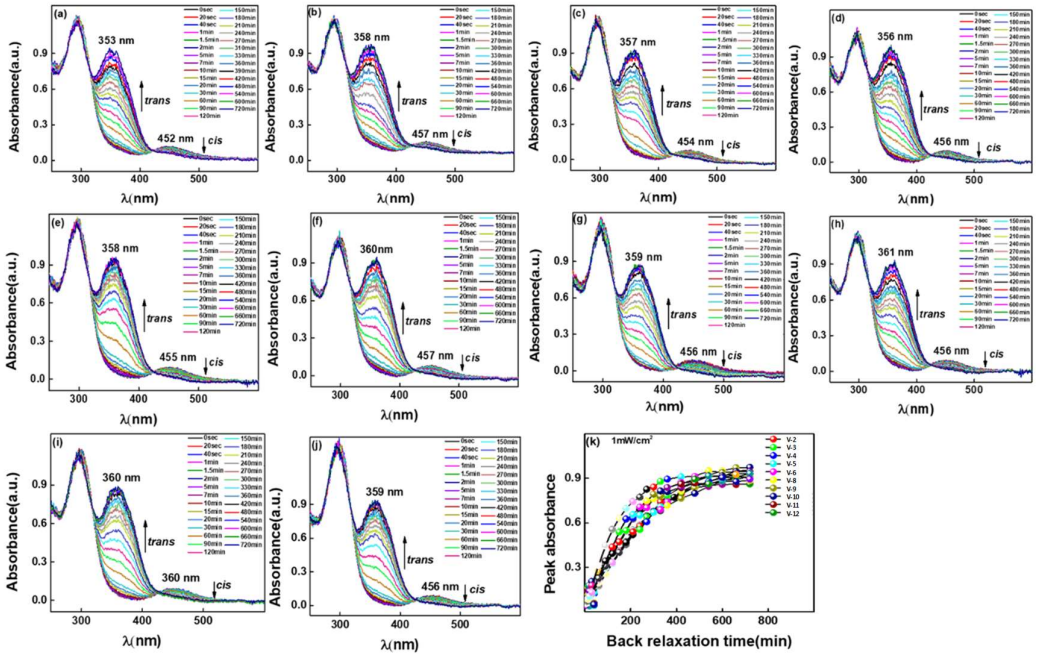

Fig. 4.17: Thermal Back relaxation studies after UV irradiation of *V-n* series from 2-12 depicted in "a to j". The plot of peak absorbance Vs. time of thermal back relaxation obtained from a-j is depicted in k. One can see that within 500 minutes most of the *cis* molecules are converted back to *trans* molecules.

4.3.6.1 Kinetic studies

The influence of time and temperature on thermal isomerization can be comprehended by studying the kinetics involved during the process. The first order plot of $-k_{C-t}t$ vs the thermal relaxation time for the investigated compounds at room temperature can be obtained by calculating $-k_{C-t}t$ using Equation 2

$$ln\frac{A_\infty - A_t}{A_\infty - A_0} = -k_{C-t}t \qquad (2)$$

Where A_0, A_t and A_∞ are the peak absorbance values at time zero, t and infinity, respectively.

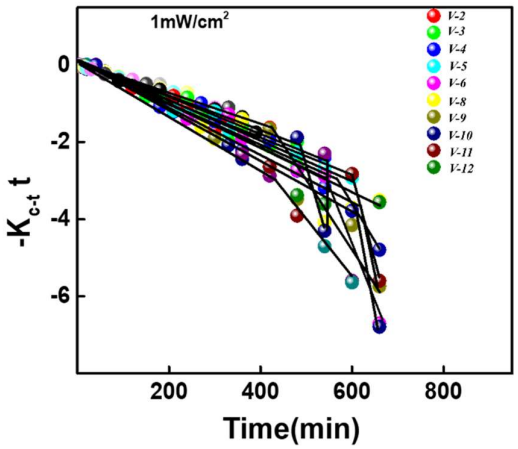

Fig. 4.18: First order and second order plots of the azobenzene systems studied for *cis-trans* thermal isomerization

Fig. 4.18 shows the first-order to second order plot for the compounds *V-n* series. Until 400 minutes system follow first-order kinetics, as indicated by the linear plot. However, it was noted that the dimers with prolonged thermal back relaxation times deviated from first-order kinetics, which may be due to the influence of mild temperature changes that occur during the study over time.

4.3.6.2 Reason behind the Phenomenon

The study of liquid crystal materials incorporating azobenzene moieties with increasing chain length in the middle of the structures are always intriguing due to the competing effects that occur when light of the appropriate wavelength is shine on them. Before light illumination, the molecules have a rod-like shape. However, when exposed to UV light of 365 nm wavelength, they change their structure and take on a distorted bent. When these molecules are part of a guest-host system in a real device, they orient themselves as rod-shaped molecules with the host liquid crystals. But when exposed to UV light of 365 nm wavelength, they change orientation and prefer to adopt a distorted bent shape due to their flexible nature in the middle of the core molecular structure. In this scenario, the host liquid crystals become trapped in the distorted bent shape giving them more time to escape, and typically have longer thermal back relaxation times. In view of this we tried here to explain the observed phenomena using three distinct cases (see **Fig. 4.19** for the cartoon diagram). Here we chose three cases such as n=2, n=6 and n=12 to understand the influence of the spacer length on the guest-host systems.

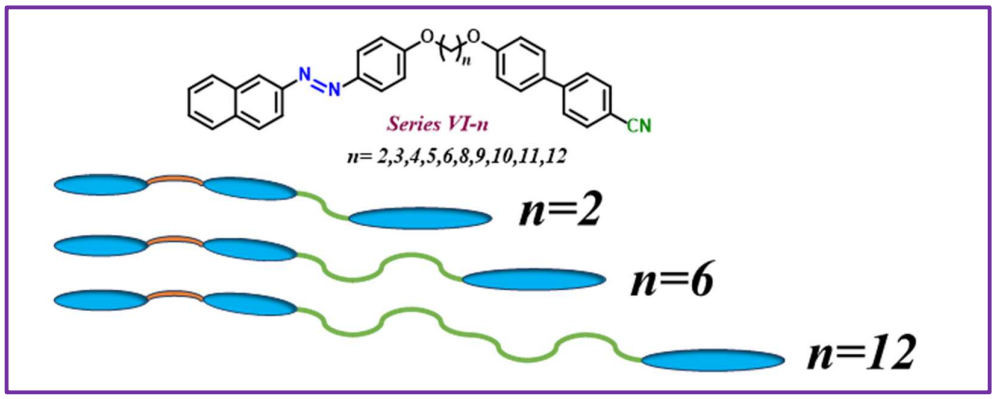

Fig. 4.19: Cartoon diagram showing the distribution of spacer length along with the chemical structure.

Case 1: *n*=2

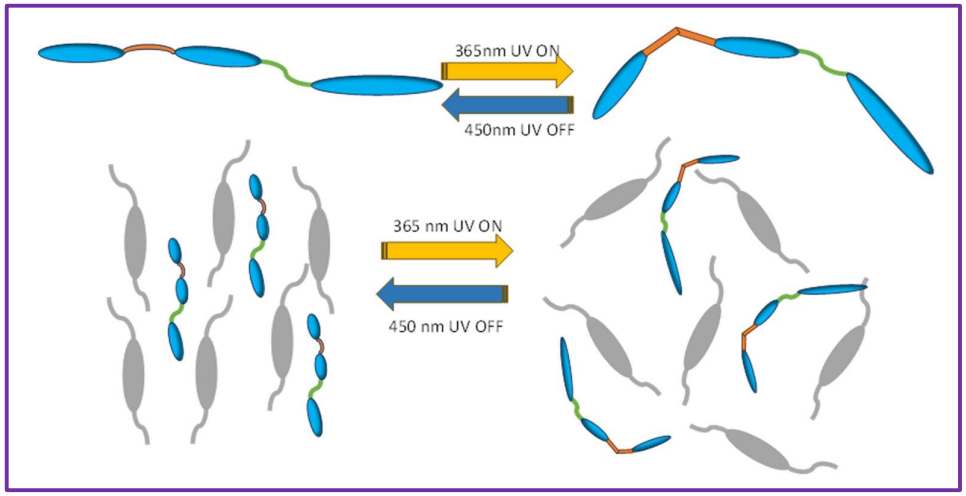

Fig. 4.20: Picture depicting the situation where spacer length is fixed at *n*=2.

When spacer length *n*=2 in the guest-host system, both liquid crystal host molecules and the guest unsymmetrical dimers are happy to be in the rod shape. As soon as UV light of wavelength ~365 nm is shined on them, host liquid crystal molecules changing from an ordered nematic phase to a disordered isotropic phase whereas dimers will change their configuration. Near to the -*N*=*N*- linkage they slightly bend and this bending will dictate the remaining structure to follow. Due to this some kind of rope structure is formed (as shown in **Fig. 4.20**) which preventing the host liquid crystalline molecules to relax back quickly to their original configuration.

Case 2: *n*=6

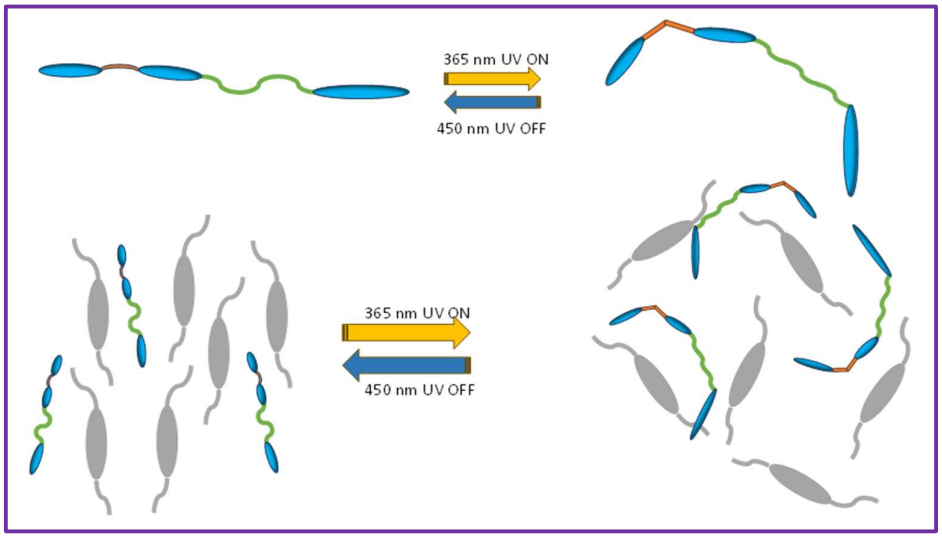

Fig. 4.21: Picture depicting the situation where spacer length is fixed at *n*=6.

When spacer length *n*=6 in the guest-host system, both liquid crystal host molecules and the guest unsymmetrical dimers are happy to be in the rod shape before shining the UV light on them. As soon as UV light of wavelength ~365 nm is shined on them, host liquid crystal molecules changing again from an ordered nematic phase to a disordered isotropic phase whereas unsymmetrical dimers will change their configuration. Near to the -*N*=*N*- linkage they bend substantially due to the longer spacer length and this bending will dictate the remaining structure to follow. Due to this some kind of coiled structure is formed (as shown in **Fig. 4.21**) which prevents the host liquid crystalline molecules from relaxing back quickly to their original configuration.

Case 3: *n*=12

When spacer length *n*=12 in the guest-host system, both liquid crystal host molecules and the guest unsymmetrical dimers are happy to be in the rod shape before shining the UV light on them. As soon as UV light of wavelength ~365 nm is shined on them, host liquid crystal molecules change again from an ordered nematic phase to a disordered isotropic phase whereas unsymmetrical dimers will change their configuration. Near to the -*N*=*N*- linkage they bend drastically due to the longer spacer length and this bending will dictate the remaining structure to follow. Due to this a completely coiled structure is formed (as shown in **Fig. 4.22**) which prevents the host liquid crystalline molecules to relax back quickly to their original configuration.

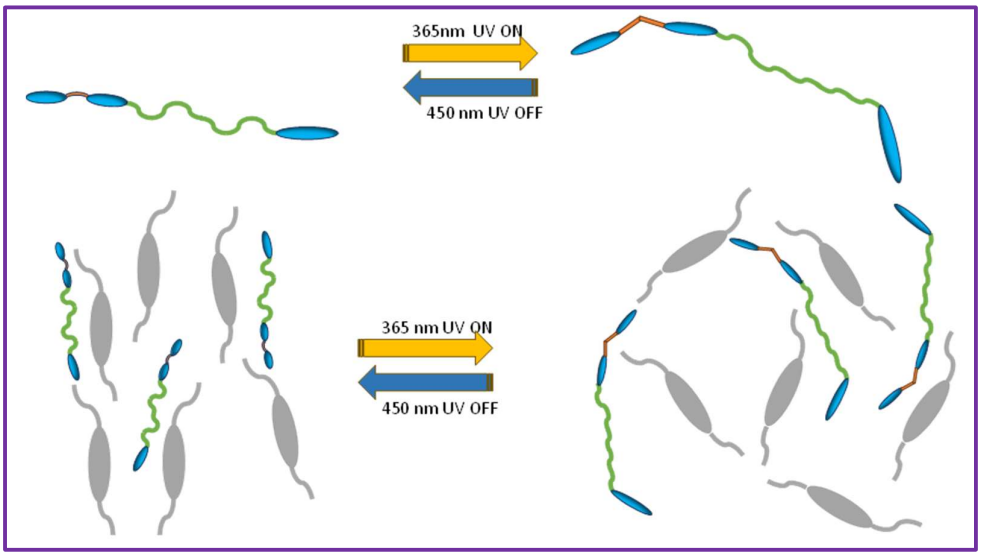

Fig. 4.22: Picture depicting the situation where spacer length is fixed at *n*=12.

In all three cases, always unsymmetrical dimers create difficult situations for the host molecules to relax back to the original configuration. Since this bending is happening at one end and the spacer changing length happening at the other end, the overall chemical structure remains more or less the same except for the flexibility in the middle of the structure. Perhaps, in the future one can add the spacer length at the end of the benzene ring may lead to different back relaxation times with respect to the change in the spacer length. A study on this is in progress and will be reported elsewhere.

4.3.6.3 Device Fabrication

The optical storage device is fabricated using unsymmetrical dimer (n=11 which showed the highest conversion efficiency) as the guest molecule and the E7, room temperature liquid crystal as the host molecules. Here we mixed 5% of the guest unsymmetrical dimers in 95% of the host E7 molecules. Previously prepared ITO-coated rubbed polyimide cell is filled with the guest-host mixture using capillary action. After filling, the suitable mask is kept on top of the liquid crystal cell and UV light of wavelength 5mW/cm^2 is shined for 2 minutes. After that, the mask was removed and the device was seen through crossed polarizers.

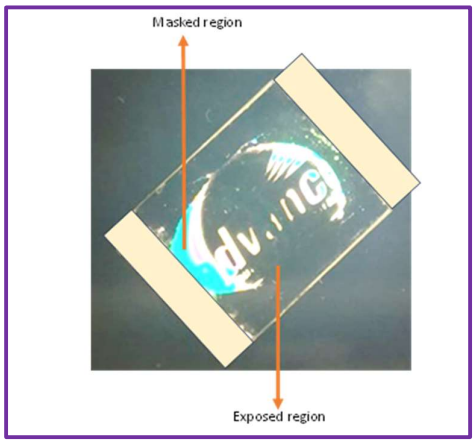

Fig. 4.23: Optical storage device fabricated using unsymmetrical dimers with n=12, where dimers were used as the guest molecule and the liquid crystal E7 is used as the host molecule. One can see from the device that exposed region is corresponding to the UV illumination (dark state) and the masked region corresponds to that UV-protected area through a mask (dark state).

One can see from **Fig. 4.23** that, wherever the mask is protected, liquid crystal molecules remain in the ordered nematic phase (bright state) and wherever UV is exposed on them, they turn to the isotropic phase (dark state). One can clearly see the excellent contrast between the dark and the white states from the unsymmetrical dimers incorporated in the system.

The current study depicts that, proper tuning of the spacers inside the chemical structure can enhance the device performances drastically and also the strong structure-property relationship is the key to success in the area of optical storage devices.

4.3.7 Physical properties (Birefringence and dielectric constant)

Interestingly ***VI-9*** possesses a relatively higher dipole moment (**Table 4.5**) compared to other homologues exhibiting enantiotropic nematic phase with relatively low nematic to isotropic transition temperature. Also, even though the estimated value aspect ratio of odd dimers in the series goes on increasing the estimated dipole moment is ~4.7 micro-Debye for n=3 to 9 and suddenly it reduces to ~ 3.58 micro-Debye for n=11 homologue, which exhibits monotropic smectic C phase in addition to nematic phase. So, we have taken up the physical property measurements on this interesting particular homologue ***VI-9.***

4.3.7.1 Experimental Setup

For the experimental studies, cells were fabricated using transparent and conducting ITO (indium tin oxide) coated glass plates. The planar alignment of these substrates was achieved by spin-coating with a polyimide (PI2555) layer and rubbing unidirectionally using a soft cloth. The ITO plates were arranged such that the rubbing direction of each plate was antiparallel to the other and stuck together. The thickness of the empty cells was measured using the Fiber optic spectrometer (ocean optics) by interferometry technique, and the cells of thickness ~ 13µm were used for further studies. Before filling the cells, the empty capacitance of the cell is measured using a Lock-in amplifier (SR830 DSP). The liquid crystal ***VI-9*** was filled in these cells in the isotropic phase. The temperature of the LC cell is controlled using a hot stage (MICRO OPTIC, MTDC600) having a sensitivity of ±0.1ºC. The optical textures of the prepared LC cell were recorded using a polarising optical microscope (POM; OLYMPUS BX53M) as a function of temperature, starting from the isotropic phase.

Electrooptic studies were carried out using an electro-optic setup in which a He-Ne laser of 632nm passes through the LC cell kept in a hostage between crossed polarizers. The rubbing direction of the planar aligned LC cell mounted between the cross polarizers is maintained at 45ºC with respect to that of both polarizer and analyzer. The transmitted intensity was detected using a photodiode (THORLABS, DET 10A) which was measured using a digital multimeter (KEYSIGHT, 34461A). The transmitted intensity as a function of temperature has been collected and used to calculate the birefringence of the LC. The transmitted intensity (I_{tr}) of a LC cell is given as[49]

$$\boldsymbol{I_{tr} = \frac{I_0}{2}(1 - \cos \Delta\phi)}$$

Where I_0 is the intensity of incident light and $\Delta\phi$ is the optical phase difference introduced by the cell. After calculating the $\Delta\phi$ the birefringence (Δn) can be calculated as[50]

$$\boldsymbol{\Delta n = \frac{\lambda \Delta\phi}{2\pi d}}$$

Where d is the thickness of the cell and λ is the wavelength of incident light.

The dielectric constant(ε) measurements as a function of voltage at 1KHz frequency were carried out using a Lock-in amplifier (SR830 DSP). The measurements are recorded through a PC using the LAB View programme. Dielectric permittivity at applied voltage of 0.5V and 5V was estimated. Dielectric spectroscopy measurements

were carried out using LCR meter (HIOKI, IM3536-01). The parameters such as capacitance, resistance, impedance*(Z)* and dielectric loss(tanδ) as a function of frequency (8Hz to 8MHz, V_{app} = 0.05V) at different temperatures were measured. From the measured data various other parameters such as the real part of dielectric permittivity (ε'), the imaginary part of dielectric permittivity (ε") and ac conductivity (σ) as a function of frequency were calculated.

4.3.7.2 Results and Discussion of the study

The birefringence (Δn) of ***VI-9*** as a function of reduced temperature is shown in **Fig. 4.24(a)**. The temperature variation of birefringence observed for ***VI-9*** is similar to that of cyanobiphenyl dimers exhibiting uniaxial nematic phase.

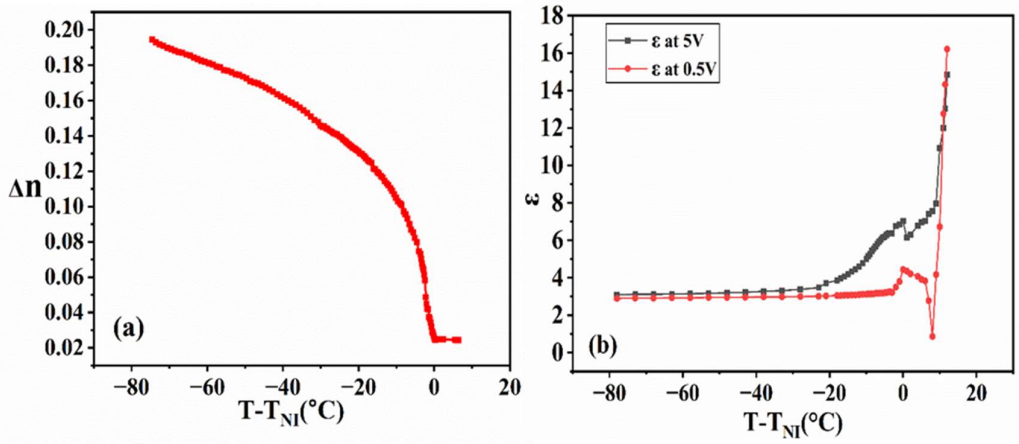

Fig. 4.24: (a) Variation of birefringence(Δn) as a function of temperature (T-T_{NI}) of *VI-9* (b) Variation of dielectric permittivity at 0.5V and 5V as a function of temperature (T-T_{NI}) of *VI-9* at applied frequency 1KHz.

The dielectric permittivity of ***VI-9*** enclosed in planar aligned cell measured at 1 KHz measured at 0.5V and 5V are shown in **Fig. 4.24(b)**. The dielectric permittivity of ***VI-9*** in the isotopic phase is larger than that observed in the nematic phase. Just above the NI transition even in isotropic phase of ***VI-9***, dielectric anisotropy can be observed might be due to the formation of small domains with effective dipole moment contributing to a higher value. As the sample is cooled below the dielectric permittivity measured at 0.5V in nematic phase starts decreasing with decrease in temperature and the variation slows down and attains 2.9. Whereas the dielectric permittivity measured at 5V in the nematic phase initially increases and starts decreasing as it cooled further and attains a value of ~3.1. This behaviour may be observed due to the rearrangement

of molecular domains with effective dipole moment of opposite nature. In CBnCB dimers such behaviour is observed, it is reported that the increase of the orientational order in the deep nematic phase favours the extended conformers with a statistically lower net longitudinal dipole moment, leading to monotonically decreasing values of ε at 5V. Furthermore, experiments have to be carried out to further explore this point.[51]

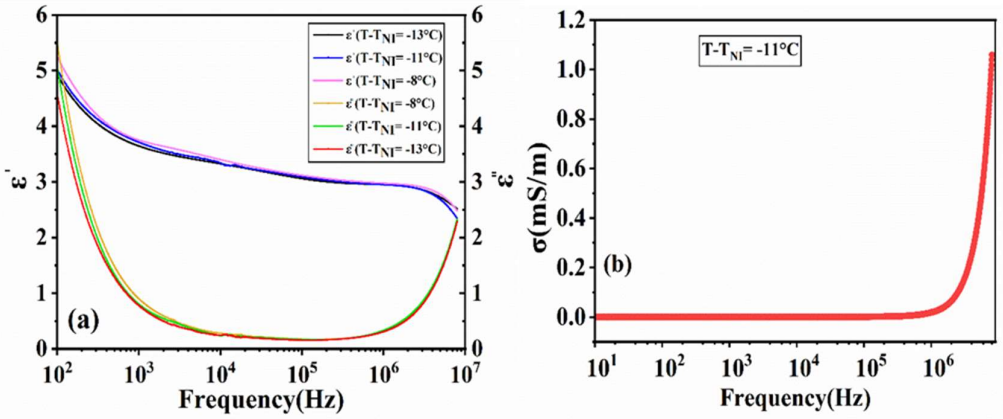

Fig. 4.25: (a) Variation of conductivity as a function of the frequency of *VI-9* (b) Variation of the real and imaginary part of dielectric permittivity (Ɛ' and Ɛ") as a function of the frequency of *VI-9*

The real and imaginary part of dielectric permittivity, ac conductivity measured in the nematic phase are shown in **Fig. 4.25(a)** and **Fig. 4.25(b)** respectively. The relaxation phenomenon might take place somewhere in the region ~ 10MHz or above and hence has not been observed in these measurements. However, one can clearly observe that the real part of dielectric permittivity starts reducing and simultaneously one can observe the rise in the imaginary part of dielectric permittivity.

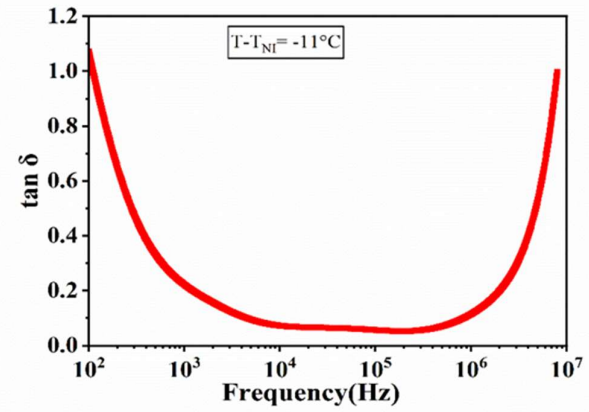

Fig. 4.26: Variation of dielectric loss (tan δ) as a function of frequency of *VI-9* at T-T_{NI}= -11 °C.

The dielectric loss (tanδ) measured in the planar aligned cell of ***VI-9*** as a function of frequency is shown in **Fig. 4.26**. The dielectric loss which is the measure of the ratio of imaginary part of dielectric permittivity (ε'') to that of the real part of dielectric permittivity (ε') is very low compared to the conventional nematic LCs. Further investigation using other measurement techniques might throw light on this.

4.4 Conclusion

Both the series (***V-n*** and ***VI-n***) of unsymmetrical dimers of cyanobiphenyl and azo/azomethine naphthalene demonstrated mesogenic behaviour, characterized by enantiotropic nematic phases and, in certain cases, the presence of smectic C phases. The study revealed that the length of the flexible spacer significantly influences the thermotropic properties, with longer spacers leading to lower transition temperatures due to increased flexibility and reduced intermolecular forces. The odd-even effect further impacted the mesophase behaviour, where odd-membered dimers, particularly those with n=3 and n=5, exhibited lower clearing temperatures and monotropic nematic phase. Interestingly, in the case of n=11, both nematic and smectic phases were observed, suggesting a diminishing odd-even effect with longer chains. Additionally, photoswitching studies via UV-Visible spectroscopy for series ***V-n*** showed consistent conversion efficiencies of 88-95% across all dimers, highlighting their high sensitivity to UV irradiation along with thermal back relaxation time of ~ 500 minutes (irrespective of the spacer length). These findings underscore the critical role of molecular architecture in determining the mesogenic and photochromic properties of these liquid crystal dimers. Optical storage device was also fabricated showing excellent dark and bright contract depicting the feasibility of the materials for the further investigations. Physical properties like birefringence and dielectric constant were studied for ***VI-9*** dimer.

4.5 Experimental Section

4.5.1 Materials

All the starting materials and reagents were purchased from (S.R.L. Chemicals, Mumbai) and used without further purification. Solvents like acetone, ethyl acetate and petroleum ether (60-80) were de-moisturized and purified before use.

4.5.2. Measurements

The instruments used are the same as in section **2A.5.2.** For Photophysical studies, UV light of intensity ~1 mW/cm^2 using an OMNICURE series 2000 was used for irradiation. UV light source equipped with a heat filter to prevent heat radiation from the source and 365nm UV filter. For the study of Physical properties like Birefringence and dielectric constant different instruments were used. The temperature of the LC cell is controlled using a hot stage (MICRO OPTIC, MTDC600) having a sensitivity of ±0.1ºC. The optical textures of the prepared LC cell were recorded using a polarising optical microscope (POM; OLYMPUS BX53M). The transmitted intensity was detected using a photodiode (THORLABS, DET 10A) which was measured using a digital multimeter (KEYSIGHT, 34461A). Dielectric spectroscopy measurements were carried out using LCR meter (HIOKI, IM3536-01). The dielectric constant(ε) measurements as a function of voltage at 1KHz frequency were carried out using a Lock-in amplifier (SR830 DSP).

4.5.3. Synthesis and Characterization

4.5.3.1. (E)-4'-(ω-(4-(Naphthalen-2-yldiazenyl)phenoxy)alkoxy)-[1,1'-biphenyl]-4-carbonitrile (V-n)

4.5.3.1.1 (E)-4-(Naphthalen-2-yldiazenyl)phenol (NpAzOH)

The synthesis of (E)-4-(naphthalen-2-yldiazenyl)phenol (NpAzOH) is described in Chapter 2, Section 2A.5.3.1.

4.5.3.1.2 (E)-4-{4-[(ω-Bromoalkyl)oxy]phenyl}benzonitrile (CBBr-n)[41]

4-Cyano-4'-hydroxybiphenyl (1 eq.), the required 1,ω-dibromoalkane (10 eq.) and anhydrous potassium carbonate (3 eq.) were added to acetone (250 mL), and the reaction mixture was refluxed for 24 h. The mixture was filtered and the inorganic residue was washed with copious amounts of acetone. The solvent was removed in vacuo and the resulting liquid was poured into ice-cold petroleum ether (350 mL). After several hours, the resulting precipitate was collected and washed with petroleum ether.

The crude product was purified via column chromatography (Pet ether: ethylacetate 96:4) to give the title compound as a white solid. Yields in the range of 66-72 % were obtained. All the compounds were synthesised and confirmed with the reported melting points.

4.5.3.1.3 Synthesis of (E)-4'-(ω-(4-(naphthalen-2-yldiazenyl)phenoxy)alkoxy)-[1,1'-biphenyl]-4-carbonitrile (V-n)

In a round bottom flask with a reflux system and stirring for 15 minutes, (E)-4-(naphthalen-2-yldiazenyl) phenol (**NpAzOH**) (0.52 mmol) and **CBBr-n** (0.5 mmol) were dissolved in acetone. Additions of anhydrous K_2CO_3 (15.7 mmol) and a catalytic amount of KI were made to the reaction mixture, and the system was refluxed for about 48 h (monitored by TLC). The hot solution was filtered and washed with acetone after the reaction was finished. The filtrate was then collected and evaporated in a rotary evaporator. Cold petroleum ether was added to the concentrated extracts, and the resulting precipitate was filtered and washed two times with this same solvent. Column chromatography is used to purify the resulting compound. (96:4 pet ether: ethyl acetate)

4.5.3.1.4 Characterization of dimers V-n

(E)-4'-(2-(4-(Naphthalen-2-yldiazenyl)phenoxy)ethoxy)-[1,1'-biphenyl]-4-carbonitrile

(*V-2*):

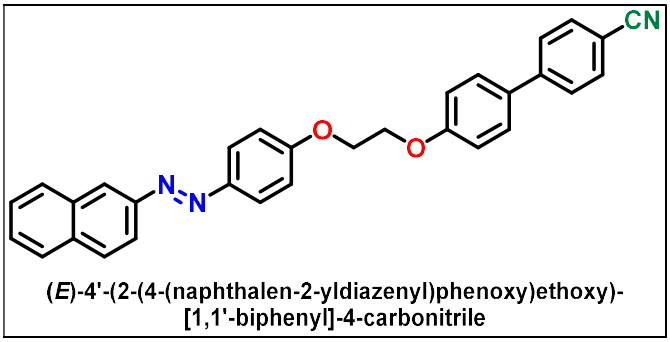

(*E*)-4'-(2-(4-(naphthalen-2-yldiazenyl)phenoxy)ethoxy)-[1,1'-biphenyl]-4-carbonitrile

Orange crystals, Yield: 67%; **IR** ν_{max}/cm^{-1}: 3058.51, 2937.18 (C_{sp3}-H), 2868.76, 2223.41 (C≡N), 1601.95 (-N=N-), 1243.02 (C-O), 1182.79 (C-N), 1069.78, 819.98; **^{1}H NMR (400 MHz, $CDCl_3$): δ (In ppm)**: 8.33 (s, 1H, Ar-H), 7.98 (d, *J* = 8.4 Hz, 1H, Ar-H), 7.92 (d, *J* = 8.4 Hz, 1H, Ar-H), 7.89 (d, *J* = 8.8 Hz, 2H, Ar-H), 7.83 (d, *J* = 9.2 Hz, 2H, Ar-H), 7.61 (d, *J* = 8.4 Hz, 2H, Ar-H), 7.56 (d, *J* = 8.4 Hz, 2H, Ar-H), 7.48 (d, *J* = 2.8 Hz, 2H, Ar-H), 7.45 (d, *J* = 8.8 Hz, 2H, Ar-H), 6.94 (d, *J* = 8.8 Hz, 2H, Ar-H), 6.88 (d, *J* = 8.8 Hz, 2H, Ar-H), 4.01 (t, *J* = 6.0 Hz, 2H, -O-CH_2-), 3.96 (t, *J* = 6.0 Hz,

2H, -O-C<u>H</u>$_2$-); **^{13}C NMR (400MHz, CDCl$_3$): δ (In ppm):** 161.31 (Ar <u>C</u>-O-), 159.44, 150.31, 147.17, 145.15, 134.61, 133.57, 132.65, 131.62, 129.14, 128.42, 127.13, 126.69, 124.81, 119.15, 117.25, 115.16, 114.77, 110.10, 65.26 (Ar-O-<u>C</u>-); **Elemental Analysis**: $C_{31}H_{23}N_3O_2$:(cal): C, 79.30; H, 4.94; N, 8.95; found C, 79.19; H, 4.91; N, 8.91; %;

***(E)-4'-(3-(4-(Naphthalen-2-yldiazenyl)phenoxy)propoxy)-[1,1'-biphenyl]-4-carbonitrile* (*V-3*):**

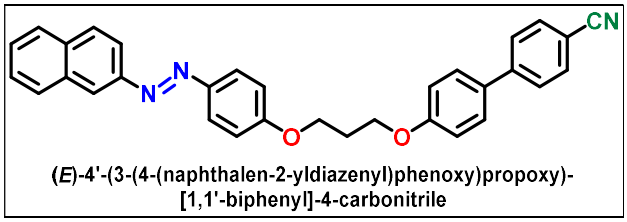

(*E*)-4'-(3-(4-(naphthalen-2-yldiazenyl)phenoxy)propoxy)-[1,1'-biphenyl]-4-carbonitrile

Orange crystals, Yield: 65%; **IR** ν_{max}/cm^{-1}: 3066.43, 2933.33 (C_{sp3}-H), 2868.38, 2224.00 (C≡N), 1598.77 (-N=N-), 1245.98 (C-O), 1181.69 (C-N), 1048.64, 822.09; **^{1}H NMR (400 MHz, CDCl$_3$): δ (In ppm)**: 8.33 (s, 1H, Ar-<u>H</u>), 8.08 (d, *J* = 8.4 Hz, 1H, Ar-<u>H</u>), 8.06 (d, *J* = 8.4 Hz, 1H, Ar-<u>H</u>), 8.0 (d, *J* = 8.8 Hz, 2H, Ar-<u>H</u>), 7.91 (d, *J* = 9.2 Hz, 2H, Ar-<u>H</u>), 7.71 (d, *J* = 8.0 Hz, 2H, Ar-<u>H</u>), 7.65 (d, *J* = 8.0 Hz, 2H, Ar-<u>H</u>), 7.58 (d, *J* = 3.2 Hz, 2H, Ar-<u>H</u>), 7.56 (d, *J* = 8.8 Hz, 2H, Ar-<u>H</u>), 7.08 (d, *J* = 8.8 Hz, 2H, Ar-<u>H</u>), 7.05 (d, *J* = 8.0 Hz, 2H, Ar-<u>H</u>), 4.31 (t, *J* = 6.0 Hz, 2H, -O-C<u>H</u>$_2$-), 4.27 (t, *J* = 6.0 Hz, 2H, -O-C<u>H</u>$_2$-), 2.40-2.34 (m, 2H, -O-C-<u>CH$_2$</u>-); **^{13}C NMR (400MHz, CDCl$_3$): δ (In ppm):** 161.32 (Ar <u>C</u>-O-), 159.45, 150.30, 147.15, 145.19, 134.57, 133.61, 132.61, 131.65, 129.15, 128.43, 127.14, 126.69, 124.81, 119.16, 117.25, 115.11, 114.78, 110.11, 64.55 (Ar-O-<u>C</u>-), 29.23; **Elemental Analysis**: $C_{32}H_{25}N_3O_2$:(cal): C, 79.48; H, 5.21; N, 8.69; found C, 79.39; H, 5.19; N, 8.61; %;

(E)-4'-(4-(4-(Naphthalen-2-yldiazenyl)phenoxy)butoxy)-[1,1'-biphenyl]-4-carbonitrile

(*V-4*):

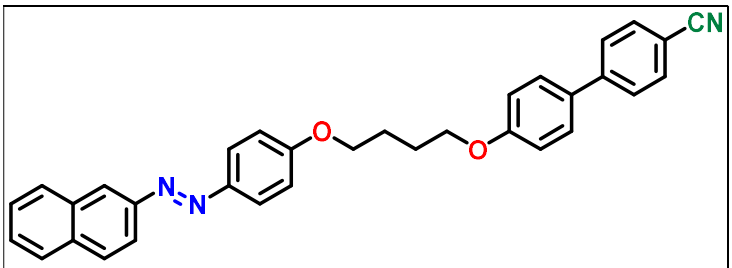

(*E*)-4'-(4-(4-(naphthalen-2-yldiazenyl)phenoxy)butoxy)-[1,1'-biphenyl]-4-carbonitrile

Orange crystals, Yield: 69%; **IR** ν_{max}/cm^{-1}: 3055.39, 2941.96 (Csp3-H), 2869.95, 2222.95 (C≡N), 1601.40 (-N=N-), 1257.46 (C-O), 1177.44 (C-N), 1027.12, 819.32; **^{1}H NMR (400 MHz, $CDCl_3$): δ (In ppm)**: 8.33 (s, 1H, Ar-H), 8.08 (d, *J* = 8.4 Hz, 1H, Ar-H), 8.05 (d, *J* = 8.4 Hz, 1H, Ar-H), 8.02 (d, *J* = 8.8 Hz, 2H, Ar-H), 7.91 (d, *J* = 9.2 Hz, 2H, Ar-H), 7.72 (d, *J* = 8.0 Hz, 2H, Ar-H), 7.66 (d, *J* = 8.0 Hz, 2H, Ar-H), 7.58 (d, *J* = 3.2 Hz, 2H, Ar-H), 7.56 (d, *J* = 8.8 Hz, 2H, Ar-H), 7.06 (d, *J* = 8.8 Hz, 2H, Ar-H), 7.03 (d, *J* = 8.0 Hz, 2H, Ar-H), 4.31 (t, *J* = 6.0 Hz, 2H, -O-CH_2-), 4.18 (t, J = 6.0 Hz, 2H, -O-CH2-), 4.14 (t, J = 6.0 Hz, 2H, -O-CH2-), 2.12-2.08 (m, 4H, -O-C-CH_2- X 2); **^{13}C NMR (400MHz, $CDCl_3$): δ (In ppm):** 161.35 (Ar C-O-), 159.43, 150.30, 147.11, 145.20, 134.53, 133.71, 132.61, 131.60, 129.15, 128.43, 127.15, 126.69, 124.82, 119.10, 117.25, 115.16, 114.78, 110.14, 64.70 (Ar-O-C-), 27.20; **Elemental Analysis**: $C_{33}H_{27}N_3O_2$:(cal): C, 79.66; H, 5.47; N, 8.44; found C, 79.72; H, 5.45; N, 8.39; %;

***(E)-4'-((5-(4-(Naphthalen-2-yldiazenyl)phenoxy)pentyl)oxy)-[1,1'-biphenyl]-4-carbonitrile* (*V-5*):**

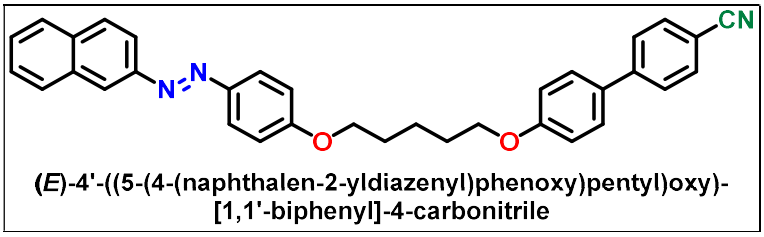

(*E*)-4'-((5-(4-(naphthalen-2-yldiazenyl)phenoxy)pentyl)oxy)-[1,1'-biphenyl]-4-carbonitrile

Orange crystals, Yield: 65%; **IR** ν_{max}/cm^{-1}: 3055.32, 2941.91 (C_{sp3}-H), 2868.99, 2222.98 (C≡N), 1601.48 (-N=N-), 1259.46 (C-O), 1177.44 (C-N), 1027.12, 819.39; **^{1}H NMR (400 MHz, $CDCl_3$): δ (In ppm)**: 8.32 (s, 1H, Ar-H), 7.97 (d, *J* = 8.4 Hz, 1H, Ar-H), 7.92 (d, *J* = 8.4 Hz, 1H, Ar-H) 7.89 (d, *J* = 8.8 Hz, 2H, Ar-H), 7.82 (d, *J* = 9.2 Hz, 2H, Ar-H), 7.59 (d, *J* = 8.0 Hz, 2H, Ar-H), 7.54 (d, *J* = 8.0 Hz, 2H, Ar-H), 7.47 (d, *J* = 3.2 Hz, 2H, Ar-H), 7.44 (d, *J* = 8.8 Hz, 2H, Ar-H), 6.95 (d, *J* = 8.8 Hz, 2H, Ar-H), 6.90 (d, *J* = 9.4 Hz, 2H, Ar-H), 3.97 (t, J = 6.0 Hz, 2H, -O-CH_2-), 3.93 (t, J = 6.0 Hz,

2H, -O-C$\underline{H_2}$-), 1.75-1.74 (m, 4H, -O-C-$\underline{CH_2}$- X 2), 1.58 (m, 2H, -O-C-C-$\underline{CH_2}$-); **^{13}C NMR (400MHz, $CDCl_3$): δ (In ppm):** 161.66 (Ar $\underline{C}$-O-), 158.72, 149.25, 145.86, 144.23, 133.45, 132.54, 131.51, 130.18, 128.19, 127.29, 126.87, 126.10, 125.60, 116.24, 113.99, 113.68, 109.01, 65.21 (Ar-O-$\underline{C}$-), 28.31, 24.43; **Elemental Analysis**: $C_{34}H_{29}N_3O_2$:(cal): C, 79.82; H, 5.71; N, 8.21; found C, 79.80 H, 5.70; N, 8.31; %;

***(E)-4'-((6-(4-(Naphthalen-2-yldiazenyl)phenoxy)hexyl)oxy)-[1,1'-biphenyl]-4-carbonitrile* (*V-6*):**

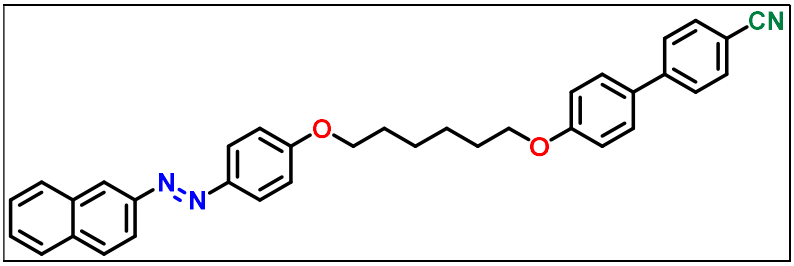

Orange crystals, Yield: 67%; **IR** ν_{max}/cm^{-1}: 3056.36, 2938.38 (C_{sp3}-H), 2868.08, 2220.20 (C≡N), 1600.49 (-N=N-), 1247.71 (C-O), 1177.28 (C-N), 1027.70, 818.60; **^{1}H NMR (400 MHz, $CDCl_3$): δ (In ppm)**: 8.42 (s, 1H, Ar-$\underline{H}$), 7.98 (d, *J* = 8.4 Hz, 1H, Ar-$\underline{H}$), 7.92 (d, *J* = 8.4 Hz, 1H, Ar-$\underline{H}$), 7.89 (d, *J* = 8.8 Hz, 2H, Ar-$\underline{H}$), 7.83 (d, *J* = 9.2 Hz, 2H, Ar-$\underline{H}$), 7.60 (d, *J* = 8.0 Hz, 2H, Ar-$\underline{H}$), 7.55 (d, *J* = 8.0 Hz, 2H, Ar-$\underline{H}$), 7.47 (d, *J* = 3.2 Hz, 2H, Ar-$\underline{H}$), 7.44 (d, *J* = 8.8 Hz, 2H, Ar-$\underline{H}$), 6.95 (d, *J* = 8.8 Hz, 2H, Ar-$\underline{H}$), 6.91 (d, *J* = 9.4 Hz, 2H, Ar-$\underline{H}$), 4.01 (t, J = 6.0 Hz, 2H, -O-C$\underline{H_2}$-), 3.96 (t, J = 6.0 Hz, 2H, -O-C$\underline{H_2}$-), 1.81-1.80 (m, 4H, -O-C-$\underline{CH_2}$- X 2), 1.53-1.52 (m, 4H, -O-C-C-$\underline{CH_2}$- X 2); **^{13}C NMR (400MHz, $CDCl_3$): δ (In ppm):** 161.56 (Ar $\underline{C}$-O-), 158.65, 149.25, 145.91, 144.19, 133.46, 132.54, 131.54, 130.26, 128.10, 127.31, 126.87, 126.10, 125.61, 118.13, 116.19, 113.67, 108.94, 66.90 (Ar-O-$\underline{C}$-), 29.95, 28.10, 24.80; **Elemental Analysis**: $C_{35}H_{31}N_3O_2$:(cal): C, 79.97; H, 5.94; N, 7.99; found C, 79.91; H, 5.92; N, 7.94; %;

***(E)-4'-((8-(4-(Naphthalen-2-yldiazenyl)phenoxy)octyl)oxy)-[1,1'-biphenyl]-4-carbonitrile* (*V-8*):**

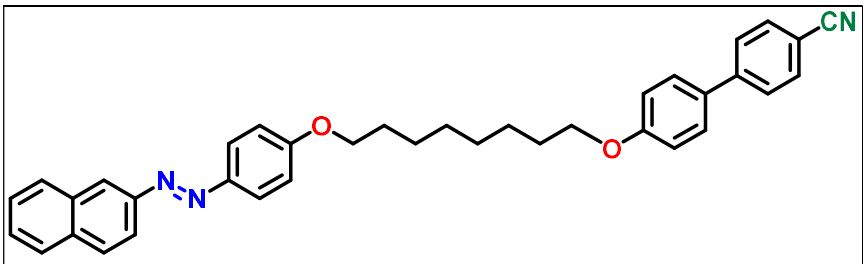

(*E*)-4'-((8-(4-(naphthalen-2-yldiazenyl)phenoxy)octyl)oxy)-[1,1'-biphenyl]-4-carbonitrile

Orange crystals, Yield: 64%; **IR** ν_{max}/cm^{-1}: 3052.31, 2936.43 (C_{sp3}-H), 2851.05, 2219.72 (C≡N), 1600.67 (-N=N-), 1251.29 (C-O), 1177.29 (C-N), 1018.16, 820.49; **^{1}H NMR (400 MHz, $CDCl_3$): δ (In ppm)**: 8.32 (s, 1H, Ar-H), 7.97 (d, *J* = 8 .0 Hz, 1H, Ar-H), 7.92 (d, *J* = 8.8 Hz, 1H, Ar-H), 7.89 (d, *J* = 8.8 Hz, 2H, Ar-H), 7.82 (d, *J* = 8.4 Hz, 2H, Ar-H), 7.59 (d, *J* = 8.0 Hz, 2H, Ar-H), 7.55 (d, *J* = 8.0 Hz, 2H, Ar-H), 7.47 (d, *J* = 3.2 Hz, 2H, Ar-H), 7.45 (d, *J* = 8.0 Hz, 2H, Ar-H), 6.94 (d, *J* = 8.4 Hz, 2H, Ar-H), 6.90 (d, *J* = 8.0 Hz, 2H, Ar-H), 3.97 (t, J = 6.0 Hz, 2H, -O-CH_2-), 3.93 (t, J = 6.0 Hz, 2H, -O-CH_2-), 1.76-1.74 (m, 4H, -O-C-CH_2- X 2), 1.43-1.35 (m, 8H, -O-C-C-(CH_2)$_4$-); **^{13}C NMR (400MHz, $CDCl_3$): δ (In ppm):** 160.61 (Ar C-O-), 158.69, 149.25, 145.87, 144.19, 133.59, 132.54, 131.52, 130.19, 128.18, 127.28, 126.87, 126.11, 125.60, 118.13, 116.06, 113.67, 108.91, 67.13 (Ar-O-C-), 29.94, 28.24, 28.13, 24.91; **Elemental Analysis**: $C_{37}H_{35}N_3O_2$:(cal): C, 80.26; H, 6.37; N, 7.59; found C, 80.23; H, 6.35; N, 7.53; %;

***(E)-4'-((9-(4-(Naphthalen-2-yldiazenyl)phenoxy)nonyl)oxy)-[1,1'-biphenyl]-4-carbonitrile* (*V-9*):**

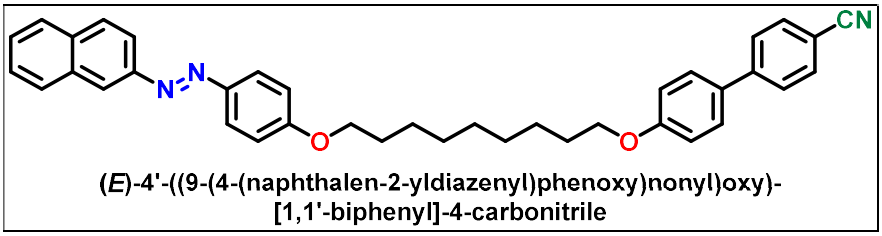

(*E*)-4'-((9-(4-(naphthalen-2-yldiazenyl)phenoxy)nonyl)oxy)-[1,1'-biphenyl]-4-carbonitrile

Orange crystals, Yield: 66%; **IR** ν_{max}/cm^{-1}: 3060.86, 2941.07 (C_{sp3}-H), 28750.51, 2225.19 (C≡N), 1600.24 (-N=N-), 1257.66 (C-O), 1182.03 (C-N), 1028.58, 821.41; **^{1}H NMR (400 MHz, $CDCl_3$): δ (In ppm)**: 8.32 (s, 1H, Ar-H), 8.08 (d, *J* = 8.4 Hz, 1H, Ar-H), 8.06 (d, *J* = 8.4 Hz, 1H, Ar-H), 8.00 (d, *J* = 8.8 Hz, 2H, Ar-H), 7.91 (d, *J* = 9.2 Hz, 2H, Ar-H), 7.69 (d, *J* = 8.0 Hz, 2H, Ar-H), 7.63 (d, *J* = 8.4 Hz, 2H, Ar-H), 7.57 (d, *J* = 3.2 Hz, 2H, Ar-H), 7.55 (d, *J* = 8.0 Hz, 2H, Ar-H), 7.05 (d, *J* = 8.8 Hz, 2H, Ar-H),

7.00 (d, *J* = 8.4 Hz, 2H, Ar-H), 4.07 (t, J = 6.0 Hz, 2H, -O-CH$_2$-), 4.01 (t, J = 6.4 Hz, 2H, -O-CH$_2$-), 1.87-1.80 (m, 4H, -O-C-CH$_2$- X 2), 1.52-1.41 (m, 10H, -O-C-C-(CH$_2$)$_5$-); **^{13}C NMR (400MHz, CDCl$_3$): δ (In ppm):** 160.72 (Ar C-O-), 159.81, 150.37, 146.99, 145.27, 133.64, 132.57, 131.26, 129.24, 128.33, 127.24, 126.93, 126.65, 124.78, 119.15, 117.36, 115.09, 110.03, 68.24 (Ar-O-C-), 29.45, 29.27, 29.19, 26.01; **Elemental Analysis**: $C_{38}H_{37}N_3O_2$:(cal): C, 80.39; H, 6.57; N, 7.40; found C, 80.32; H, 6.55; N, 7.37; %;

***(E)-4'-((10-(4-(Naphthalen-2-yldiazenyl)phenoxy)decyl)oxy)-[1,1'-biphenyl]-4-carbonitrile* (*V-10*):**

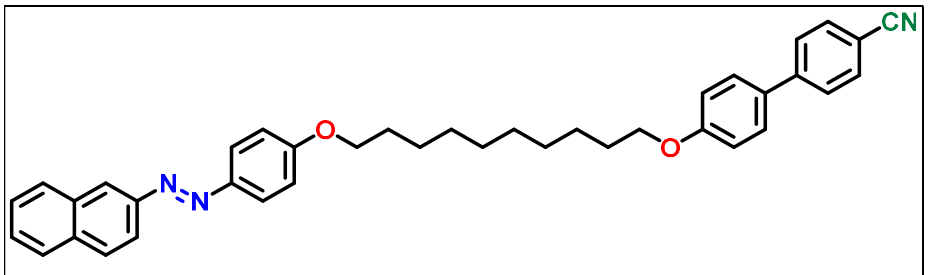

(*E*)-4'-((10-(4-(naphthalen-2-yldiazenyl)phenoxy)decyl)oxy)-[1,1'-biphenyl]-4-carbonitrile

Orange crystals, Yield: 69%; **IR** ν_{max}/cm^{-1}: 3058.20, 2924.34 (C_{sp3}-H), 2853.42, 2219.34 (C≡N), 1600.33 (-N=N-), 1257.71 (C-O), 1181.17 (C-N), 1028.29, 822.54; **^{1}H NMR (400 MHz, CDCl$_3$): δ (In ppm)**: 8.34 (s, 1H, Ar-H), 7.96 (d, *J* = 8.4 Hz, 1H, Ar-H), 7.90 (d, *J* = 8.4 Hz, 1H, Ar-H), 7.89 (d, *J* = 8.8 Hz, 2H, Ar-H), 7.82 (d, *J* = 9.2 Hz, 2H, Ar-H), 7.60 (d, *J* = 8.0 Hz, 2H, Ar-H), 7.54 (d, *J* = 8.0 Hz, 2H, Ar-H), 7.45 (d, *J* = 3.2 Hz, 2H, Ar-H), 7.44 (d, *J* = 8.4 Hz, 2H, Ar-H), 6.95 (d, *J* = 8.4 Hz, 2H, Ar-H), 6.90 (d, *J* = 8.4 Hz, 2H, Ar-H), 3.97 (t, J = 6.0 Hz, 2H, -O-CH$_2$-), 3.92 (t, J = 6.0 Hz, 2H, -O-CH$_2$-), 1.75-1.73 (m, 4H, -O-C-CH$_2$- X 2), 1.40-1.28 (m, 12H, -O-C-C-(CH$_2$)$_6$-); **^{13}C NMR (400MHz, CDCl$_3$): δ (In ppm):** 161.64 (Ar C-O-), 158.71, 149.26, 145.87, 144.21, 133.45, 132.54, 131.53, 130.17, 128.18, 127.28, 126.87, 126.09, 125.60, 116.21, 113.99, 113.68, 108.91, 67.19 (Ar-O-C-), 29.49, 28.43, 28.17, 24.97; **Elemental Analysis**: $C_{39}H_{39}N_3O_2$:(cal): C, 80.52; H, 6.76; N, 7.22; found C, 80.51; H, 6.72; N, 7.18; %;

***(E)-4'-((11-(4-(Naphthalen-2-yldiazenyl)phenoxy)undecyl)oxy)-[1,1'-biphenyl]-4-carbonitrile* (*V-11*):**

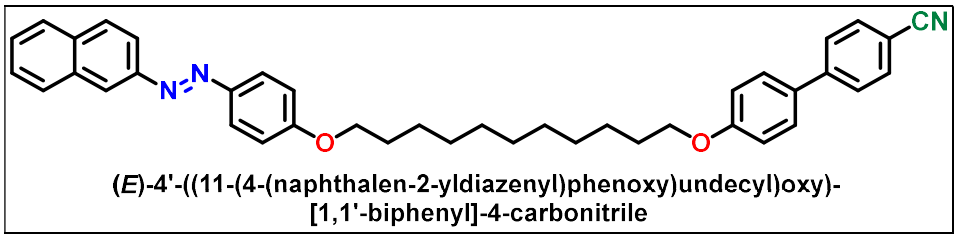

(*E*)-4'-((11-(4-(naphthalen-2-yldiazenyl)phenoxy)undecyl)oxy)-[1,1'-biphenyl]-4-carbonitrile

Orange crystals, Yield: 68%; **IR** ν_{max}/cm^{-1}: 3067.60, 2920.86 (C_{sp3}-H), 2856.29, 2223.37 (C≡N), 1600.78 (-N=N-), 1256.02 (C-O), 1182.12 (C-N), 1022.63, 820.68; **^{1}H NMR (400 MHz, $CDCl_3$): δ (In ppm)**: 8.32 (s, 1H, Ar-H), 7.96 (d, *J* = 8.4 Hz, 1H, Ar-H), 7.90 (d, *J* = 8.4 Hz, 1H, Ar-H), 7.89 (d, *J* = 8.8 Hz, 2H, Ar-H), 7.83 (d, *J* = 9.2 Hz, 2H, Ar-H), 7.60 (d, *J* = 8.0 Hz, 2H, Ar-H), 7.54 (d, *J* = 8.0 Hz, 2H, Ar-H), 7.47 (d, *J* = 3.2 Hz, 2H, Ar-H), 7.44 (d, *J* = 8.0 Hz, 2H, Ar-H), 6.95 (d, *J* = 8.4 Hz, 2H, Ar-H), 6.91 (d, *J* = 8.4 Hz, 2H, Ar-H), 3.97 (t, J = 6.0 Hz, 2H, -O-CH_2-), 3.92 (t, J = 6.0 Hz, 2H, -O-CH_2-), 1.74-1.72 (m, 4H, -O-C-CH_2- X 2), 1.40-1.29 (m, 14H, -O-C-C-(CH_2)$_7$-); **^{13}C NMR (400MHz, $CDCl_3$): δ (In ppm):** 161.74 (Ar C-O-), 159.80, 150.32, 146.94, 145.27, 134.51, 132.59, 131.22, 129.23, 128.34, 127.24, 126.98, 126.65, 124.78, 119.19, 117.31, 115.07, 110.03, 67.93 (Ar-O-C-), 29.42, 29.29, 26.58, 26.43; **Elemental Analysis**: $C_{40}H_{41}N_3O_2$:(cal): C, 80.64; H, 6.94; N, 7.05; found C, 80.63; H, 6.89; N, 7.02; %;

***(E)-4'-((12-(4-(Naphthalen-2-yldiazenyl)phenoxy)dodecyl)oxy)-[1,1'-biphenyl]-4-carbonitrile* (*V-12*):**

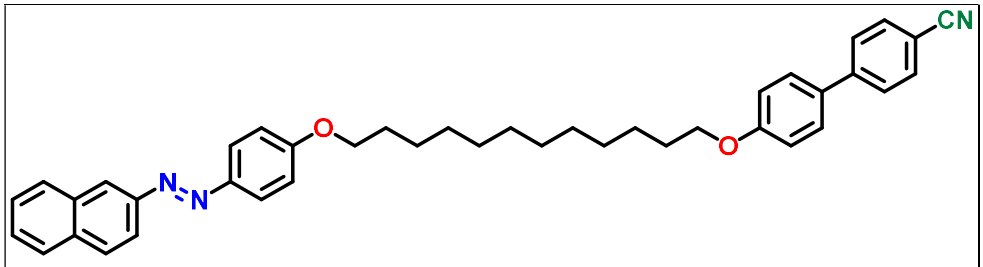

(*E*)-4'-((12-(4-(naphthalen-2-yldiazenyl)phenoxy)dodecyl)oxy)-[1,1'-biphenyl]-4-carbonitrile

Orange crystals, Yield: 66%; **IR** ν_{max}/cm^{-1}: 3058.63, 2920.27 (C_{sp3}-H), 2850.16, 2223.62 (C≡N), 1599.79 (-N=N-), 1256.02 (C-O), 1182.66 (C-N), 1028.23, 821.26; **^{1}H NMR (400 MHz, $CDCl_3$): δ (In ppm)**: 8.32 (s, 1H, Ar-H), 7.97 (d, *J* = 8.4 Hz, 1H, Ar-H), 7.91 (d, *J* = 8.4 Hz, 1H, Ar-H), 7.89 (d, *J* = 8.8 Hz, 2H, Ar-H), 7.83 (d, *J* = 9.2 Hz, 2H, Ar-H), 7.60 (d, *J* = 8.0 Hz, 2H, Ar-H), 7.55 (d, *J* = 8.0 Hz, 2H, Ar-H), 7.47 (d, *J* = 3.2 Hz, 2H, Ar-H), 7.44 (d, *J* = 8.0 Hz, 2H, Ar-H), 6.95 (d, *J* = 8.4 Hz, 2H, Ar-H),

6.91 (d, *J* = 8.4 Hz, 2H, Ar-H), 3.97 (t, J = 6.4 Hz, 2H, -O-CH$_2$-), 3.92 (t, J = 6.0 Hz, 2H, -O-CH$_2$-), 1.77-1.72 (m, 4H, -O-C-CH$_2$- X 2), 1.41-1.23 (m, 16H, -O-C-C-(CH$_2$)$_8$-); **^{13}C NMR (400MHz, CDCl$_3$): δ (In ppm):** 161.73 (Ar C-O-), 159.80, 150.34, 146.94, 145.29, 134.52, 132.59, 131.24, 129.24, 128.34, 127.24, 126.98, 126.65, 124.77, 119.19, 117.31, 115.07, 110.00, 68.24 (Ar-O-C-), 29.58, 29.39, 29.24, 26.05; **Elemental Analysis**: $C_{41}H_{43}N_3O_2$:(cal): C, 80.75; H, 7.11; N, 6.89; found C, 80.72; H, 7.09; N, 6.84; %;

4.5.3.2 (E)-4'-(ω-(4-((Naphthalen-2-ylimino)methyl)phenoxy)alkoxy)-[1,1'-biphenyl]-4-carbonitrile (VI-n)

4.5.3.2.1 (E)-4-((Naphthalen-2-ylimino)methyl)phenol (NpAmOH)

The synthesis of (E)-4-((naphthalen-2-ylimino)methyl)phenol (NpAmOH) is described in Chapter 2, Section 2A.5.3.2.

4.5.3.2.2 (E)-4-{4-[(ω-Bromoalkyl)oxy]phenyl}benzonitrile (CBBr-n)[41]

The synthesis of (E)-4-{4-[(ω-Bromoalkyl)oxy]phenyl}benzonitrile (CBBr-n) is described in 4.5.3.1.2.

4.5.3.2.3 Synthesis of (E)-4'-(ω-(4-((naphthalen-2-ylimino)methyl)phenoxy)alkoxy) -[1,1'-biphenyl]-4-carbonitrile (VI-n)

In a round bottom flask with a reflux system and stirring for 15 minutes, (E)-4-((naphthalen-2-ylimino)methyl)phenol (**NpAmOH**) (0.52 mmol) and **CBBr-n** (0.5 mmol) were dissolved in acetone. Addition of anhydrous K_2CO_3 (15.7 mmol) and a catalytic amount of KI were made to the reaction mixture, and the system was refluxed for about 48 h (monitored by TLC). The hot solution was filtered and washed with acetone after the reaction was finished. The filtrate was then collected and evaporated in a rotary evaporator. Cold petroleum ether was added to the concentrated extracts, and the resulting precipitate was filtered and washed two times with this same solvent. To obtain the desired product, the crude precipitate was recrystallised twice from ethanol.

4.5.3.4. Characterization of dimers VI-n

***(E)-4'-(2-(4-((Naphthalen-2-ylimino)methyl)phenoxy)ethoxy)-[1,1'-biphenyl]-4-carbonitrile* (*VI-2*):**

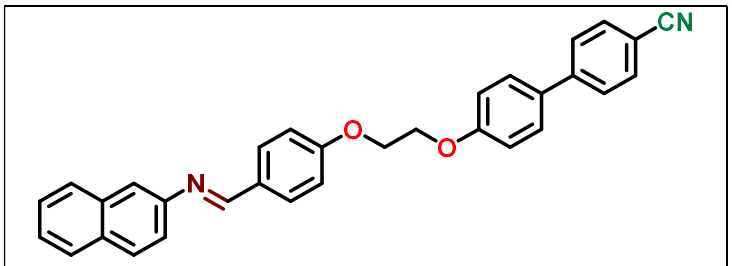

(*E*)-4'-(2-(4-((naphthalen-2-ylimino)methyl)phenoxy)ethoxy)-[1,1'-biphenyl]-4-carbonitrile

Orange crystals, Yield: 63%; **IR** ν_{max}/cm^{-1}: 3057.58, 2932.23 (C_{sp3}-H), 2868.23, 2224.18 (C≡N), 1604.21 (-CH=N-), 1244.45 (C-O), 1180.26 (C-N), 1064.68, 818.96; **^{1}H NMR (400 MHz, $CDCl_3$): δ (In ppm)**: 8.54 (s, 1H, -N=CH-), 7.92 (d, *J* = 8.0 Hz, 2H, Ar-H), 7.88 (d, *J* = 8.4 Hz, 2H, Ar-H), 7.71 (d, *J* = 8.0 Hz, 2H, Ar-H), 7.66 (d, *J* = 8.4 Hz, 2H, Ar-H), 7.60 (s, 1H, Ar-H), 7.56 (d, *J* = 8.4 Hz, 2H, Ar-H), 7.49 (d, *J* = 8.0 Hz, 2H, Ar-H), 7.47 (d, *J* = 8.0 Hz, 2H, Ar-H), 7.04 (d, *J* = 9.4 Hz, 2H, Ar-H), 7.02 (d, *J* = 9.2 Hz, 2H, Ar-H), 4.20 (t, J = 6.4 Hz, 2H, -O-CH_2-), 4.19 (t, J = 6.0 Hz, 2H, -O-CH_2-); **^{13}C NMR (400MHz, $CDCl_3$): δ (In ppm):** 161.95 (Ar C-O-), 160.01, 159.70, 150.01, 145.28, 134.18, 132.60, 131.26, 129.03, 128.35, 127.09, 126.98, 126.37, 125.18, 121.39, 119.22, 117.53, 115.07, 114.73, 109.99, 66.71 (Ar-O-C-); **Elemental Analysis**: $C_{32}H_{24}N_2O_2$:(cal): C, 82.03; H, 5.16; N, 5.98; found C, 81.98; H, 5.12; N, 5.94; %;

***(E)-4'-(3-(4-((naphthalen-2-ylimino)methyl)phenoxy)propoxy)-[1,1'-biphenyl]-4-carbonitrile* (*VI-3*):**

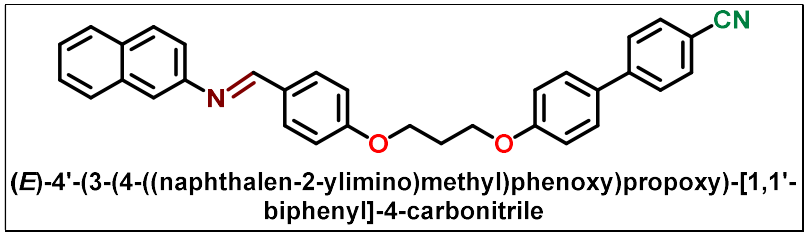

(*E*)-4'-(3-(4-((naphthalen-2-ylimino)methyl)phenoxy)propoxy)-[1,1'-biphenyl]-4-carbonitrile

Orange crystals, Yield: 62%; **IR** ν_{max}/cm^{-1}: 3054.78, 2935.62 (C_{sp3}-H), 2872.85, 2224.89 (C≡N), 1603.41 (-CH=N-), 1239.11 (C-O), 1172.13 (C-N), 1060.34, 825.86; **^{1}H NMR (400 MHz, $CDCl_3$): δ (In ppm)**: 8.54 (s, 1H, -N=CH-), 7.91 (d, *J* = 8.4 Hz, 2H, Ar-H), 7.88 (d, *J* = 8.0 Hz, 2H, Ar-H), 7.70 (d, *J* = 8.0 Hz, 2H, Ar-H), 7.65 (d, *J* = 8.4 Hz, 2H, Ar-H), 7.61 (s, 1H, Ar-H), 7.55 (d, *J* = 8.4 Hz, 2H, Ar-H), 7.49 (d, *J* = 8.0 Hz, 2H, Ar-H), 7.47 (d, *J* = 8.0 Hz, 2H, Ar-H), 7.06 (d, *J* = 9.4 Hz, 2H, Ar-H), 7.04 (d, *J* = 7.6 Hz, 2H, Ar-H), 4.27 (t, J = 6.4 Hz, 2H, -O-CH_2-), 4.25 (t, J = 6.0 Hz, 2H, -O-

C<u>H</u>$_2$-), 2.37-2.34 (m, 2H, -O-C-<u>CH</u>$_2$-); **^{13}C NMR (400MHz, CDCl$_3$): δ (In ppm):** 161.97 (Ar <u>C</u>-O-), 159.90, 159.76, 150.01, 145.26, 134.12, 132.64, 131.81, 129.09, 128.38, 127.74, 127.07, 126.33, 125.18, 121.38, 119.14, 117.47, 115.07, 114.75, 110.03, 66.21 (Ar-O-<u>C</u>-), 29.23; **Elemental Analysis**: $C_{33}H_{26}N_2O_2$:(cal): C, 82.13; H, 5.43; N, 5.81; found C, 82.11; H, 5.42; N, 5.80; %;

***(E)-4'-(4-(4-((naphthalen-2-ylimino)methyl)phenoxy)butoxy)-[1,1'-biphenyl]-4-carbonitrile* (*VI-4*):**

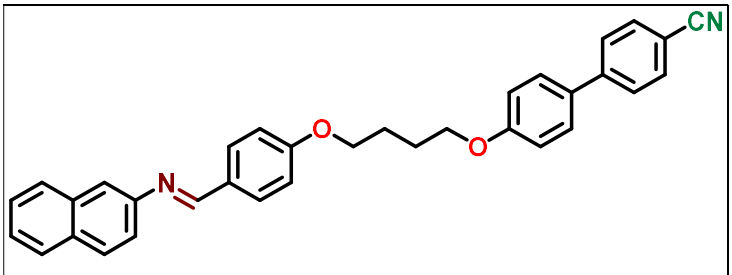

(*E*)-4'-(4-(4-((naphthalen-2-ylimino)methyl)phenoxy)butoxy)-[1,1'-biphenyl]-4-carbonitrile

Orange crystals, Yield: 64%; **IR** ν_{max}/cm^{-1}: 3058.60, 2932.14 (C_{sp3}-H), 2873.34, 2222.37 (C≡N), 1602.25 (-CH=N-), 1245.20 (C-O), 1174.47 (C-N), 1047.45, 824.27; **^{1}H NMR (400 MHz, CDCl$_3$): δ (In ppm)**: 8.54 (s, 1H, -N=C<u>H</u>), 7.92 (d, *J* = 8.0 Hz, 2H, Ar-<u>H</u>), 7.89 (d, *J* = 8.0 Hz, 2H, Ar-<u>H</u>), 7.71 (d, *J* = 8.0 Hz, 2H, Ar-<u>H</u>), 7.66 (d, *J* = 8.4 Hz, 2H, Ar-<u>H</u>), 7.60 (s, 1H, Ar-<u>H</u>), 7.56 (d, *J* = 8.4 Hz, 2H, Ar-<u>H</u>), 7.50 (d, *J* = 8.0 Hz, 2H, Ar-<u>H</u>), 7.47 (d, *J* = 8.0 Hz, 2H, Ar-<u>H</u>), 7.04 (d, *J* = 9.4 Hz, 2H, Ar-<u>H</u>), 7.02 (d, *J* = 9.2 Hz, 2H, Ar-<u>H</u>), 4.15 (t, J = 6.4 Hz, 2H, -O-C<u>H</u>$_2$-), 4.14 (t, J = 6.0 Hz, 2H, -O-C<u>H</u>$_2$-), 2.12-2.06 (m, 4H, -O-C-<u>CH</u>$_2$- X 2); **^{13}C NMR (400MHz, CDCl$_3$): δ (In ppm):** 161.73 (Ar <u>C</u>-O-), 159.86, 159.61, 149.98, 145.23, 134.18, 132.59, 131.84, 129.31, 128.40, 127.74, 127.11, 126.36, 125.19, 121.33, 119.13, 117.56, 115.10, 114.73, 110.11, 67.62 (Ar-O-<u>C</u>-), 25.97; **Elemental Analysis**: $C_{34}H_{28}N_2O_2$:(cal): C, 82.23; H, 5.68; N, 5.64; found C, 82.19; H, 5.64; N, 5.61; %;

***(E)-4'-((5-(4-((naphthalen-2-ylimino)methyl)phenoxy)pentyl)oxy)-[1,1'-biphenyl]-4-carbonitrile* (*VI-5*):**

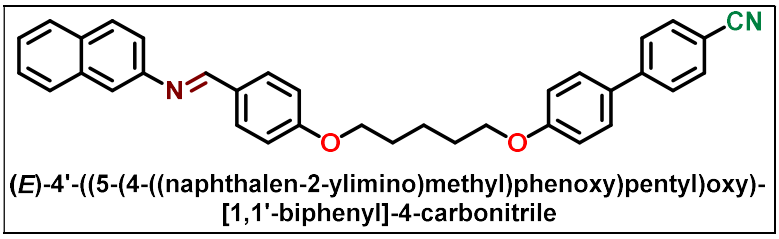

(*E*)-4'-((5-(4-((naphthalen-2-ylimino)methyl)phenoxy)pentyl)oxy)-[1,1'-biphenyl]-4-carbonitrile

Orange crystals, Yield: 65%; **IR** ν_{max}/cm^{-1}: 3053.66, 2926.27 (C_{sp3}-H), 2867.95, 2223.09 (C≡N), 1601.15 (-CH=N-), 1256.93 (C-O), 1181.38 (C-N), 1042.13, 826.14; **^{1}H NMR (400 MHz, $CDCl_3$): δ (In ppm)**: 8.53 (s, 1H, -N=CH), 7.91 (d, *J* = 8.4 Hz, 2H, Ar-H), 7.88 (d, *J* = 8.0 Hz, 2H, Ar-H), 7.70 (d, *J* = 8.0 Hz, 2H, Ar-H), 7.65 (d, *J* = 8.4 Hz, 2H, Ar-H), 7.60 (s, 1H, Ar-H), 7.54 (d, *J* = 8.4 Hz, 2H, Ar-H), 7.49 (d, *J* = 8.0 Hz, 2H, Ar-H), 7.46 (d, *J* = 8.0 Hz, 2H, Ar-H), 7.05 (d, *J* = 9.4 Hz, 2H, Ar-H), 7.01 (d, *J* = 8.0 Hz, 2H, Ar-H), 4.05 (t, J = 6.4 Hz, 2H, -O-CH_2-), 4.02 (t, J = 6.0 Hz, 2H, -O-CH_2-), 1.85-1.83 (m, 4H, -O-C-CH_2- X 2), 1.70-1.66 (m, 2H, -O-C-C-CH_2-); **^{13}C NMR (400MHz, $CDCl_3$): δ (In ppm):** 161.92 (Ar C-O-), 159.97, 159.75, 150.03, 145.22, 134.15, 132.60, 131.29, 129.08, 128.36, 127.77, 127.08, 126.36, 125.19, 121.38, 119.11, 117.55, 115.07, 114.73, 110.06, 68.15 (Ar-O-C-), 29.23, 29.17, 26.04; **Elemental Analysis**: $C_{35}H_{30}N_2O_2$:(cal): C, 82.33; H, 5.92; N, 5.49; found C, 82.30; H, 5.88; N, 5.46; %;

***(E)-4'-((6-(4-((naphthalen-2-ylimino)methyl)phenoxy)hexyl)oxy)-[1,1'-biphenyl]-4-carbonitrile* (*VI-6*):**

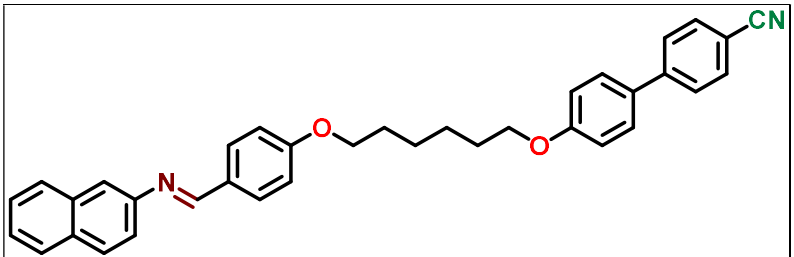

(*E*)-4'-((6-(4-((naphthalen-2-ylimino)methyl)phenoxy)hexyl)oxy)-[1,1'-biphenyl]-4-carbonitrile

Orange crystals, Yield: 66%; **IR** ν_{max}/cm^{-1}: 3057.07, 2927.32 (C_{sp3}-H), 2856.54, 2221.35 (C≡N), 1603.41 (-CH=N-), 1245.19 (C-O), 1175.01 (C-N), 1052.88, 827.02; **^{1}H NMR (400 MHz, $CDCl_3$): δ (In ppm)**: 8.54 (s, 1H, -N=CH), 7.91 (d, *J* = 8.4 Hz, 2H, Ar-H), 7.88 (d, *J* = 8.0 Hz, 2H, Ar-H), 7.69 (d, *J* = 8.0 Hz, 2H, Ar-H), 7.66 (d, *J* = 8.4 Hz, 2H, Ar-H), 7.60 (s, 1H, Ar-H), 7.55 (d, *J* = 7.8 Hz, 2H, Ar-H), 7.50 (d, *J* = 8.0 Hz, 2H, Ar-H), 7.46 (d, *J* = 8.0 Hz, 2H, Ar-H), 7.03 (d, *J* = 8.4 Hz, 2H, Ar-H), 7.01 (d,

J = 9.2 Hz, 2H, Ar-H), 4.07 (t, J = 6.0 Hz, 2H, -O-CH_2-), 4.07 (t, J = 6.0 Hz, 2H, -O-CH_2-), 2.20-2.07 (m, 4H, -O-C-CH_2- X 2), 1.70-1.61 (m, 4H, -O-C-C-CH_2- X 2); **^{13}C NMR (400MHz, $CDCl_3$): δ (In ppm):** 161.88 (Ar C-O-), 159.90, 159.75, 150.00, 145.26, 134.19, 132.59, 131.35, 129.19, 128.36, 127.74, 127.09, 126.36, 125.18, 121.35, 119.14, 117.56, 115.10, 114.75, 110.06, 68.00 (Ar-O-C-), 29.18, 29.14, 25.87; **Elemental Analysis**: $C_{36}H_{32}N_2O_2$:(cal): C, 82.41; H, 6.15; N, 5.34; found C, 82.50; H, 6.23; N, 5.32; %;

***(E)-4'-((8-(4-((naphthalen-2-ylimino)methyl)phenoxy)octyl)oxy)-[1,1'-biphenyl]-4-carbonitrile* (*VI-8*):**

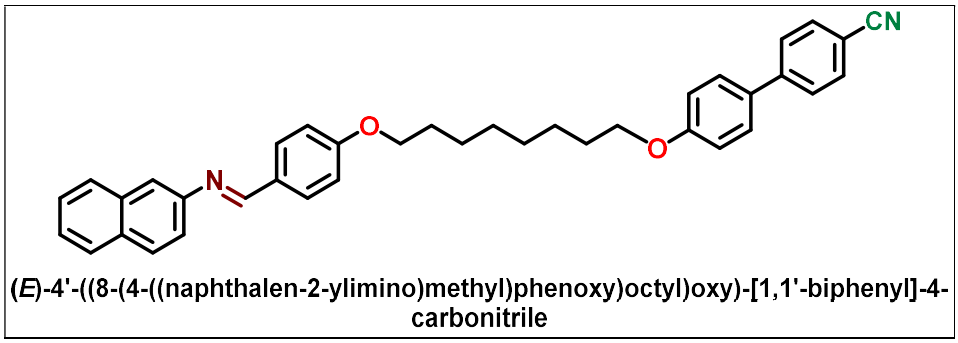

(*E*)-4'-((8-(4-((naphthalen-2-ylimino)methyl)phenoxy)octyl)oxy)-[1,1'-biphenyl]-4-carbonitrile

Orange crystals, Yield: 67%; **IR** ν_{max}/cm^{-1}: 3057.36, 2934.83 (C_{sp3}-H), 2854.44 2221.94 (C≡N), 1601.67 (-CH=N-), 1248.12 (C-O), 1156.58 (C-N), 1033.37, 822.91; **^{1}H NMR (400 MHz, $CDCl_3$): δ (In ppm)**: 8.53 (s, 1H, -N=CH), 7.91 (d, *J* = 8.0 Hz, 2H, Ar-H), 7.87 (d, *J* = 8.0 Hz, 2H, Ar-H), 7.70 (d, *J* = 8.4 Hz, 2H, Ar-H), 7.65 (d, *J* = 8.8 Hz, 2H, Ar-H), 7.60 (s, 1H, Ar-H), 7.54 (d, *J* = 8.8 Hz, 2H, Ar-H), 7.50 (d, *J* = 8.0 Hz, 2H, Ar-H), 7.47 (d, *J* = 8.0 Hz, 2H, Ar-H), 7.03 (d, *J* = 8.4 Hz, 2H, Ar-H), 7.01 (d, *J* = 8.8 Hz, 2H, Ar-H), 4.06 (t, J = 6.4 Hz, 2H, -O-CH_2-), 4.03 (t, J = 6.0 Hz, 2H, -O-CH_2-), 1.87-1.84 (m, 4H, -O-C-CH_2- X 2), 1.53-1.45 (m, 8H, -O-C-C-(CH_2)$_4$-); **^{13}C NMR (400MHz, $CDCl_3$): δ (In ppm):** 161.92 (Ar C-O-), 160.00, 159.77, 149.99, 145.26, 134.17, 132.60, 131.26, 129.08, 128.37, 127.75, 127.09, 126.38, 125.20, 121.39, 119.21, 117.57, 115.07, 114.73, 109.99, 68.12 (Ar-O-C-), 29.33, 29.23, 29.18 25.99; **Elemental Analysis**: $C_{38}H_{36}N_2O_2$:(cal): C, 82.58; H, 6.57; N, 5.07; found C, 82.53; H, 6.54; N, 5.06; %;

***(E)-4'-((9-(4-((naphthalen-2-ylimino)methyl)phenoxy)nonyl)oxy)-[1,1'-biphenyl]-4-carbonitrile* (*VI-9*):**

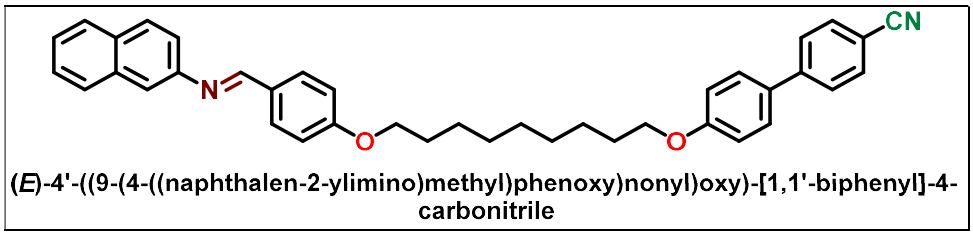

(*E*)-4'-((9-(4-((naphthalen-2-ylimino)methyl)phenoxy)nonyl)oxy)-[1,1'-biphenyl]-4-carbonitrile

Orange crystals, Yield: 66%; **IR** ν_{max}/cm^{-1}: 3040.14, 2934.15 (C_{sp3}-H), 2852.80 2220.39 (C≡N), 1604.05 (-CH=N-), 1245.06 (C-O), 1165.27 (C-N), 1015.61, 822.05; **^{1}H NMR (400 MHz, $CDCl_3$): δ (In ppm)**: 8.53 (s, 1H, -N=CH), 7.91 (d, *J* = 8.4 Hz, 2H, Ar-H), 7.88 (d, *J* = 8.0 Hz, 2H, Ar-H), 7.70 (d, *J* = 8.0 Hz, 2H, Ar-H), 7.65 (d, *J* = 8.4 Hz, 2H, Ar-H), 7.59 (s, 1H, Ar-H), 7.54 (d, *J* = 8.4 Hz, 2H, Ar-H), 7.49 (d, *J* = 8.0 Hz, 2H, Ar-H), 7.46 (d, *J* = 8.0 Hz, 2H, Ar-H), 7.02 (d, *J* = 9.4 Hz, 2H, Ar-H), 7.00 (d, *J* = 8.8 Hz, 2H, Ar-H), 4.06 (t, J = 6.4 Hz, 2H, -O-CH_2-), 4.03 (t, J = 6.4 Hz, 2H, -O-CH_2-), 1.87-1.81 (m, 4H -O-C-CH_2- X 2), 1.51-1.31 (m, 10H, -O-C-C-(CH_2)$_5$-); **^{13}C NMR (400MHz, $CDCl_3$): δ (In ppm):** 161.93 (Ar C-O-), 159.99, 159.78, 150.00, 145.27, 134.17, 132.60, 131.26, 129.07, 128.36, 127.74, 127.08, 126.36, 125.18, 121.38, 119.19, 117.55, 115.07, 114.73, 110.00, 68.15 (Ar-O-C-), 29.48, 29.31, 29.17, 26.03; **Elemental Analysis**: $C_{39}H_{38}N_2O_2$:(cal): C, 82.65; H, 7.12; N, 4.71; found C, 82.59; H, 7.03; N, 4.67; %;

***(E)-4'-((10-(4-((naphthalen-2-ylimino)methyl)phenoxy)decyl)oxy)-[1,1'-biphenyl]-4-carbonitrile* (*VI-10*):**

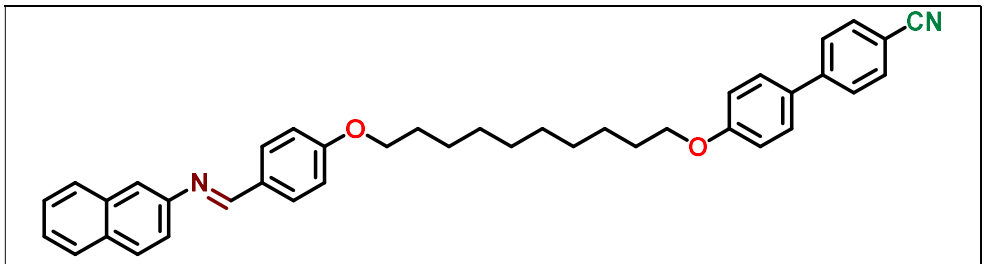

(*E*)-4'-((10-(4-((naphthalen-2-ylimino)methyl)phenoxy)decyl)oxy)-[1,1'-biphenyl]-4-carbonitrile

Orange crystals, Yield: 65%; **IR** ν_{max}/cm^{-1}: 3057.34, 2935.36 (C_{sp3}-H), 2853.29 2237.45 (C≡N), 1604.82 (-CH=N-), 1249.96 (C-O), 1171.12 (C-N), 1044.15, 822.33; **^{1}H NMR (400 MHz, $CDCl_3$): δ (In ppm)**: 8.53 (s, 1H, -N=CH), 7.91 (d, *J* = 8.4 Hz, 2H, Ar-H), 7.88 (d, *J* = 8.0 Hz, 2H, Ar-H), 7.70 (d, *J* = 8.0 Hz, 2H, Ar-H), 7.65 (d, *J* = 8.4 Hz, 2H, Ar-H), 7.60 (s, 1H, Ar-H), 7.54 (d, *J* = 8.4 Hz, 2H, Ar-H), 7.49 (d, *J* = 8.0 Hz, 2H, Ar-H), 7.46 (d, *J* = 8.0 Hz, 2H, Ar-H), 7.07 (d, *J* = 9.4 Hz, 2H, Ar-H), 7.01 (d, *J* = 8.0 Hz,

2H, Ar-H), 4.05 (t, J = 6.4 Hz, 2H, -O-CH$_2$-), 4.02 (t, J = 6.0 Hz, 2H, -O-CH$_2$-), 1.85-1.83 (m, 4H, -O-C-CH$_2$- X 2), 1.51-1.28 (m, 12H, -O-C-C-(CH$_2$)$_6$-) **^{13}C NMR (400MHz, CDCl$_3$): δ (In ppm):** 161.96 (Ar C-O-), 159.92, 159.83, 150.03, 145.27, 134.20, 132.57, 131.25, 129.12, 128.34, 127.74, 127.06, 126.35, 125.17, 121.38, 119.16, 117.56, 115.10, 114.75, 110.03, 68.15 (Ar-O-C-), 29.50, 29.38, 29.25, 26.04; **Elemental Analysis**: $C_{40}H_{40}N_2O_2$:(cal): C, 82.72; H, 6.94; N, 4.82; found C, 82.69; H, 6.91; N, 4.79; %;

***(E)-4'-((11-(4-((naphthalen-2-ylimino)methyl)phenoxy)undecyl)oxy)-[1,1'-biphenyl]-4-carbonitrile* (*VI-11*):**

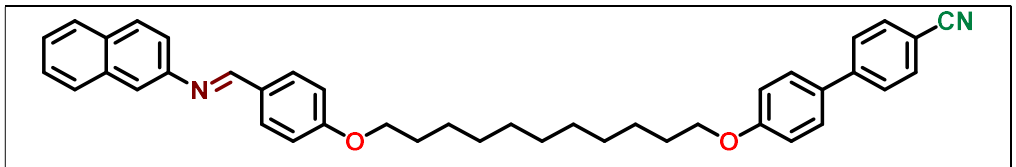

(*E*)-4'-((11-(4-((naphthalen-2-ylimino)methyl)phenoxy)undecyl)oxy)-[1,1'-biphenyl]-4-carbonitrile

Orange crystals, Yield: 68%; **IR** ν_{max}/cm^{-1}: 3064.96, 2919.72 (C_{sp3}-H), 2866.18, 2220.02 (C≡N), 1604.01 (-CH=N-), 1245.90 (C-O), 1176.30 (C-N), 1040.39, 822.20; **^{1}H NMR (400 MHz, CDCl$_3$): δ (In ppm)**: 8.53 (s, 1H, -N=CH), 7.91 (d, *J* = 8.8 Hz, 2H, Ar-H), 7.89 (d, *J* = 8.4 Hz, 2H, Ar-H), 7.70 (d, *J* = 8.0 Hz, 2H, Ar-H), 7.65 (d, *J* = 8.4 Hz, 2H, Ar-H), 7.60 (s, 1H, Ar-H), 7.55 (d, *J* = 8.4 Hz, 2H, Ar-H), 7.49 (d, *J* = 8.0 Hz, 2H, Ar-H), 7.46 (d, *J* = 8.0 Hz, 2H, Ar-H), 7.03 (d, *J* = 8.4 Hz, 2H, Ar-H), 7.01 (d, *J* = 8.0 Hz, 2H, Ar-H), 4.09 (t, J = 6.0 Hz, 2H, -O-CH$_2$-), 4.09 (t, J = 6.0 Hz, 2H, -O-CH$_2$-), 1.74-1.73 (m, 4H, -O-C-CH$_2$- X 2), 1.50-1.34 (m, 14H, -O-C-C-(CH$_2$)$_7$-); **^{13}C NMR (400MHz, CDCl$_3$): δ (In ppm):** 161.99 (Ar C-O-), 159.91, 159.82, 150.05, 145.26, 134.20, 132.56, 131.25, 129.10, 128.34, 127.74, 127.06, 126.35, 125.17, 121.38, 119.17, 117.56, 115.11, 114.75, 110.04, 68.50 (Ar-O-C-), 29.52, 29.36, 29.22, 26.03; **Elemental Analysis**: $C_{41}H_{42}N_2O_2$:(cal): C, 82.79; H, 7.12; N, 4.71; found C, 82.74; H, 7.13; N, 4.70; %;

***(E)-4'-((12-(4-((naphthalen-2-ylimino)methyl)phenoxy)dodecyl)oxy)-[1,1'-biphenyl]-4-carbonitrile* (*VI-12*):**

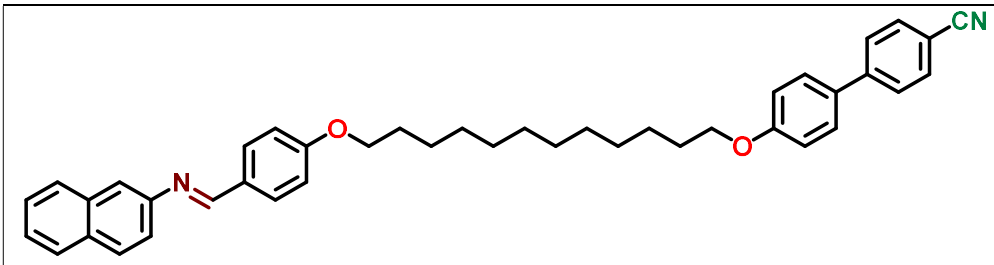

(*E*)-4'-((12-(4-((naphthalen-2-ylimino)methyl)phenoxy)dodecyl)oxy)-[1,1'-biphenyl]-4-carbonitrile

Orange crystals, Yield: 67%; **IR** ν_{max}/cm^{-1}: 3058.46, 2919.54 (C_{sp3}-H), 2851.29, 2236.18 (C≡N), 1605.70 (-CH=N-), 1253.82 (C-O), 1171.03 (C-N), 1053.73, 820.14; **^{1}H NMR (400 MHz, $CDCl_3$): δ (In ppm)**: 8.53 (s, 1H, -N=CH), 7.91 (d, *J* = 8.4 Hz, 2H, Ar-H), 7.88 (d, *J* = 8.0 Hz, 2H, Ar-H), 7.70 (d, *J* = 8.0 Hz, 2H, Ar-H), 7.65 (d, *J* = 8.4 Hz, 2H, Ar-H), 7.60 (s, 1H, Ar-H), 7.54 (d, *J* = 8.4 Hz, 2H, Ar-H), 7.49 (d, *J* = 8.0 Hz, 2H, Ar-H), 7.46 (d, *J* = 8.0 Hz, 2H, Ar-H), 7.02 (d, *J* = 9.4 Hz, 2H, Ar-H), 7.00 (d, *J* = 9.2 Hz, 2H, Ar-H), 4.05 (t, J = 6.4 Hz, 2H, -O-CH_2-), 4.02 (t, J = 6.0 Hz, 2H, -O-CH_2-), 1.75-1.72 (m, 4H, -O-C-CH_2- X 2), 1.51-1.38 (m, 16H, -O-C-C-$(CH_2)_8$-); **^{13}C NMR (400MHz, $CDCl_3$): δ (In ppm):** 161.95 (Ar C-O-), 160.03, 159.80, 150.01, 145.28, 134.16, 132.60, 131.24, 129.04, 128.35, 127.74, 127.09, 126.36, 125.18, 121.39, 119.21, 117.54, 115.07, 114.73, 109.99, 68.19 (Ar-O-C-), 29.59, 29.41, 29.22, 26.05; **Elemental Analysis**: $C_{42}H_{44}N_2O_2$:(cal): C, 82.86; H, 7.28; N, 4.60; found C, 82.82; H, 7.22; N, 4.57; %;

4.6 Spectras

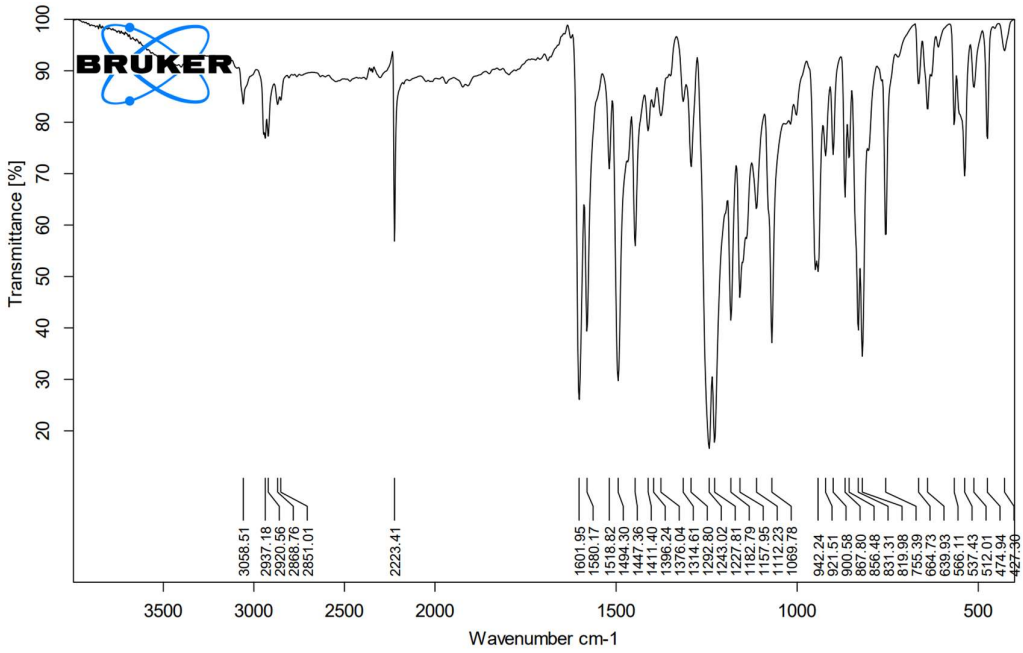

Fig. S4.1: FT-IR spectra of *V-2*

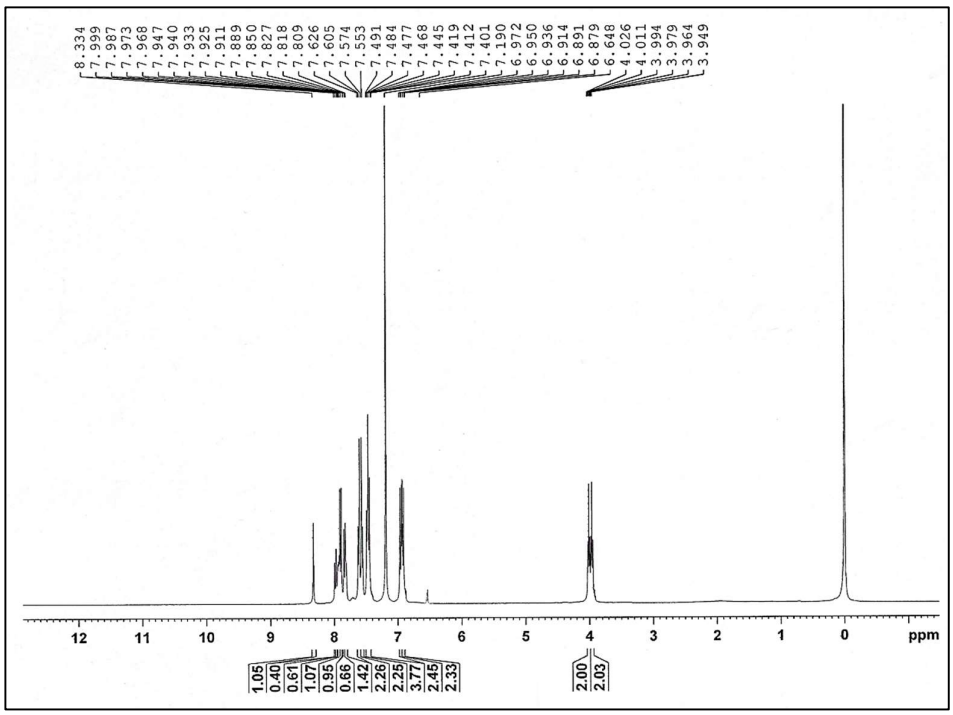

Fig. S4.2: ^{1}H-NMR spectra of *V-2*

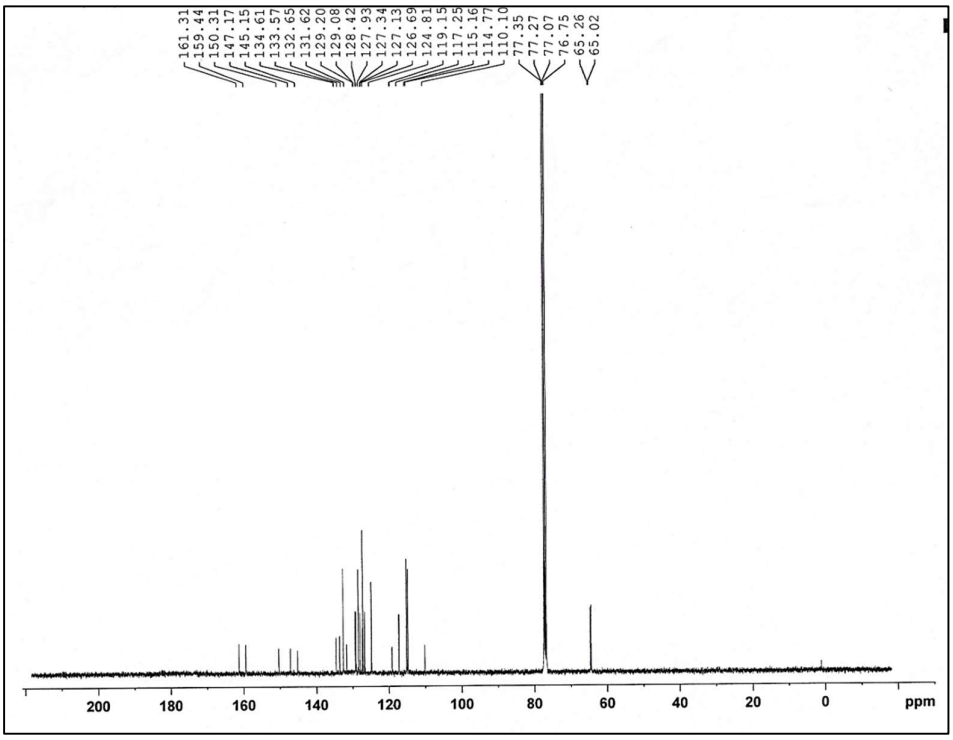

Fig. S4.3: ^{13}C-NMR spectra of *V-2*

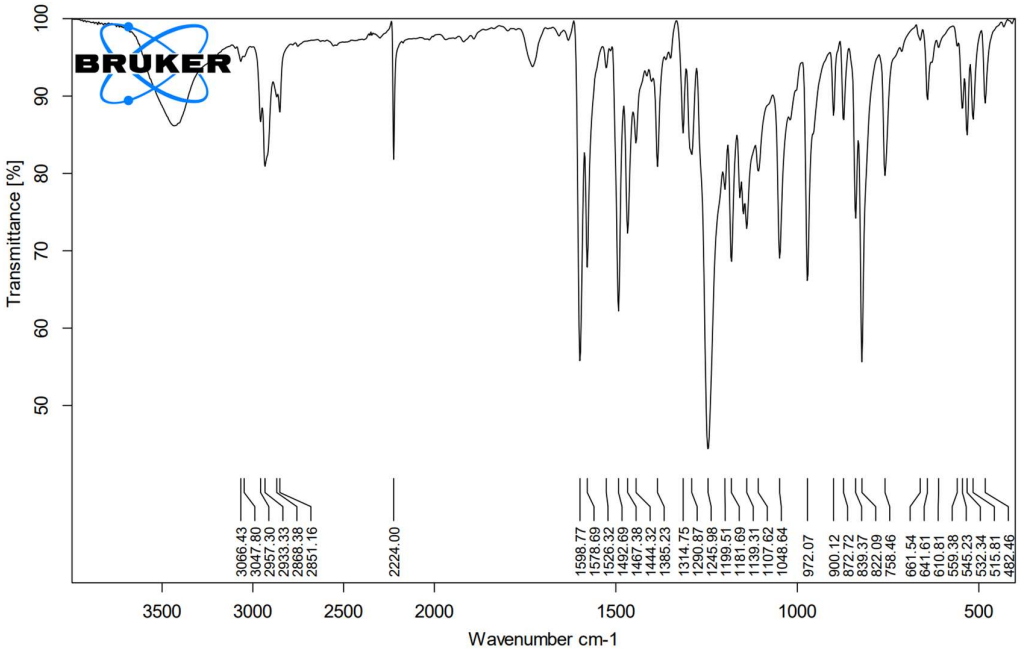

Fig. S4.4: FT-IR spectra of *V-3*

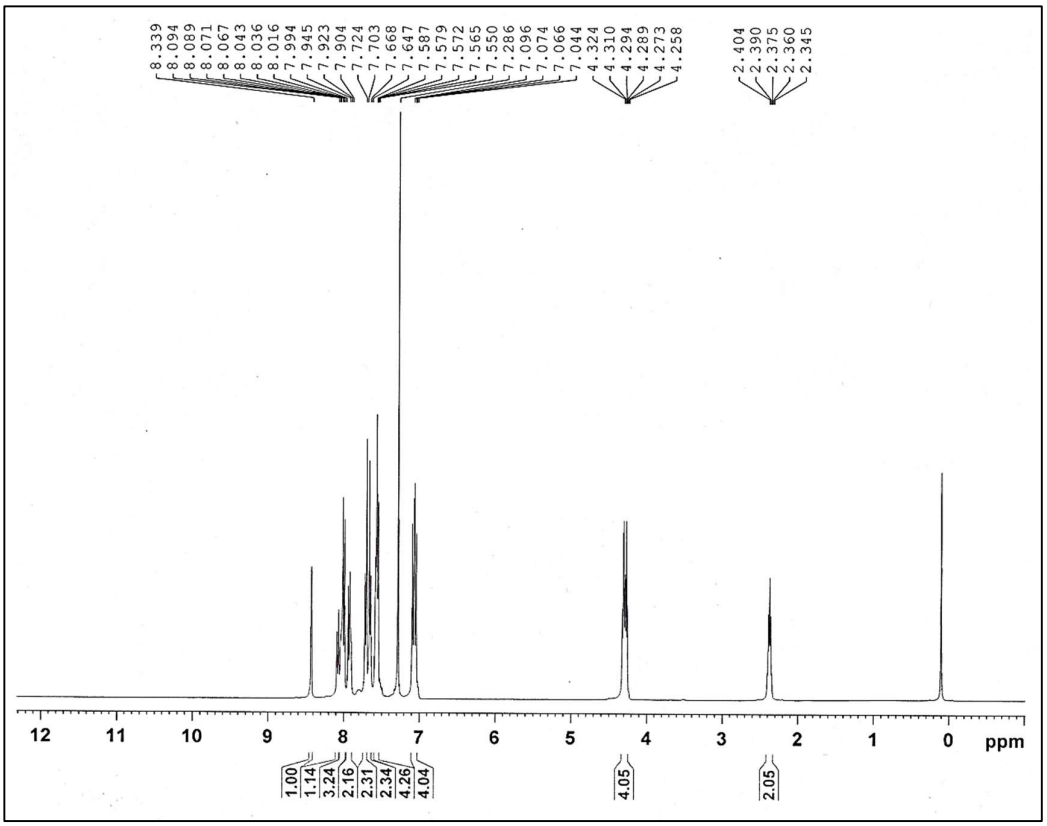

Fig. S4.5: ^{1}H-NMR spectra of *V-3*

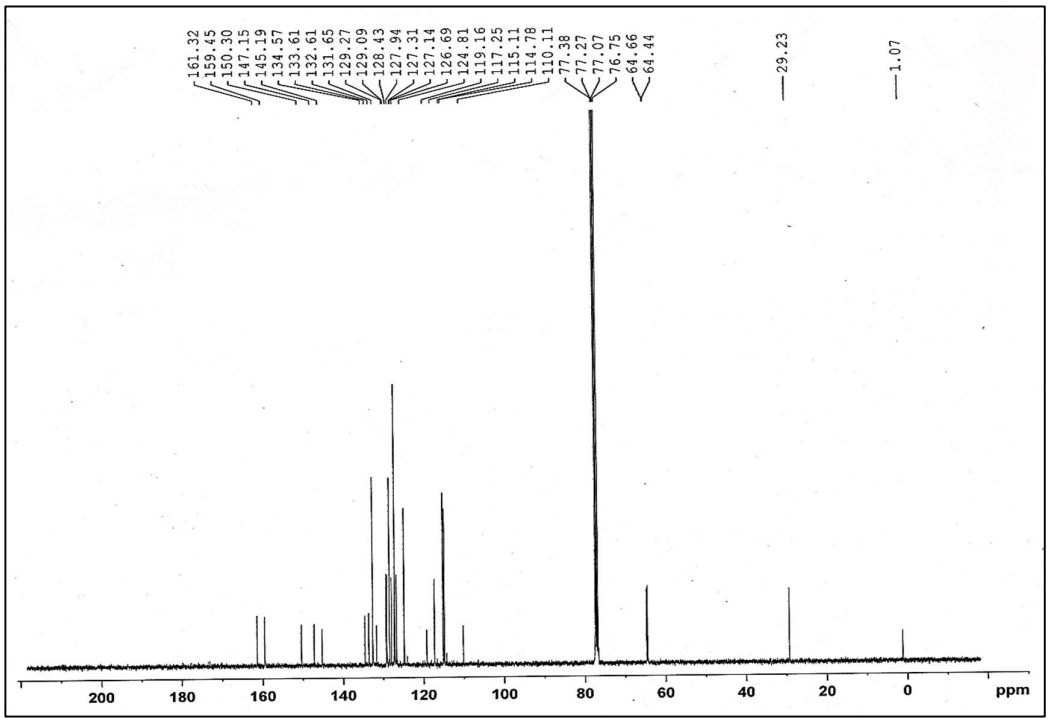

Fig. S4.6: ^{13}C-NMR spectra of *V-3*

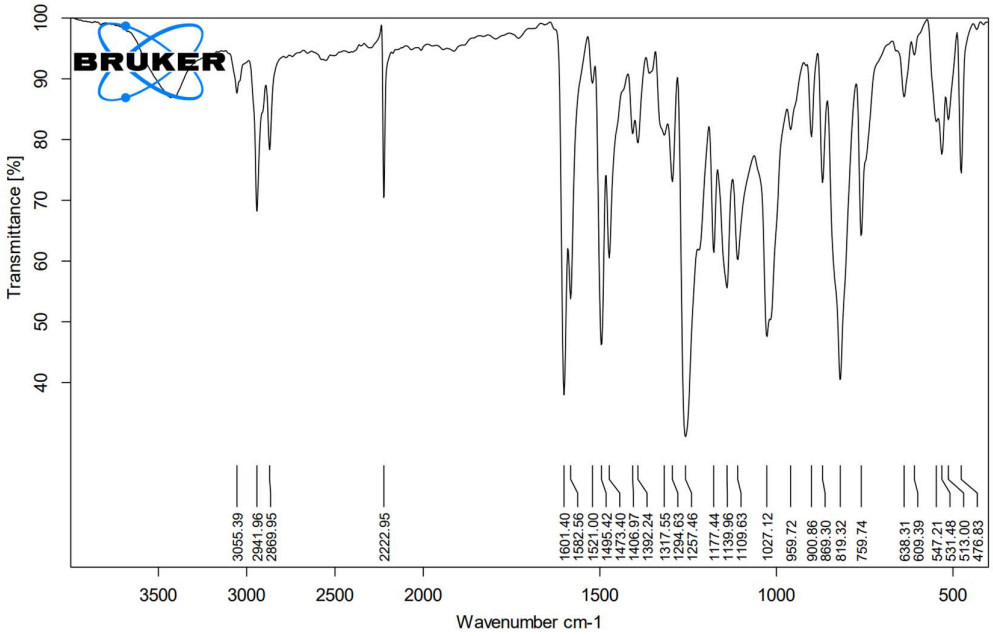

Fig. S4.7: FT-IR spectra of *V-4*

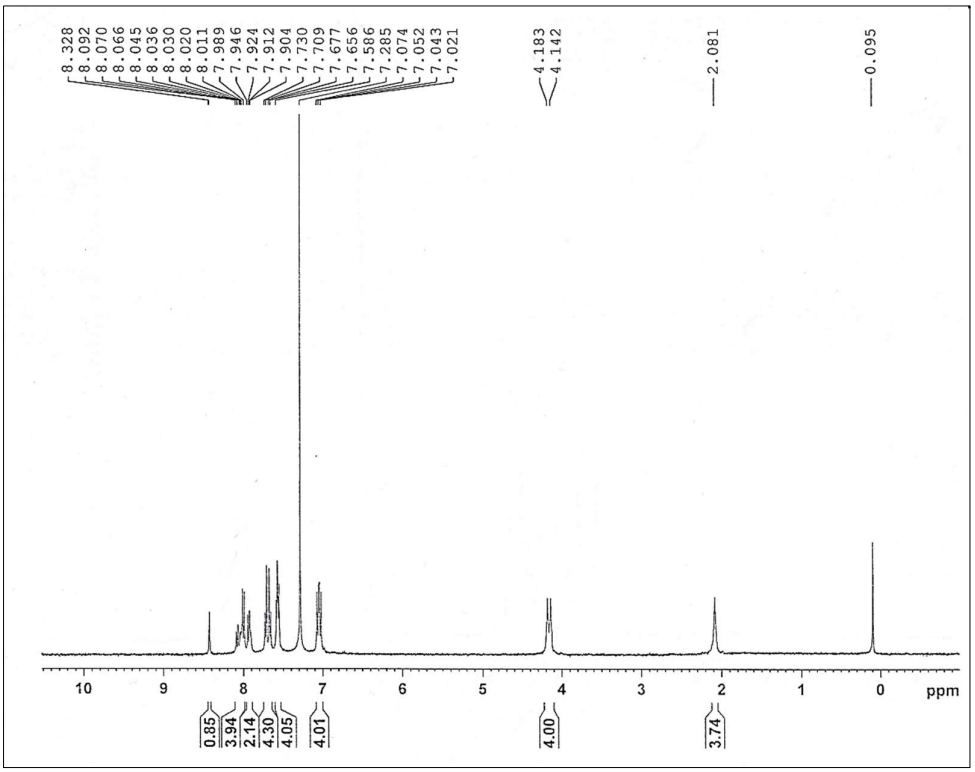

Fig. S4.8: ^{1}H-NMR spectra of *V-4*

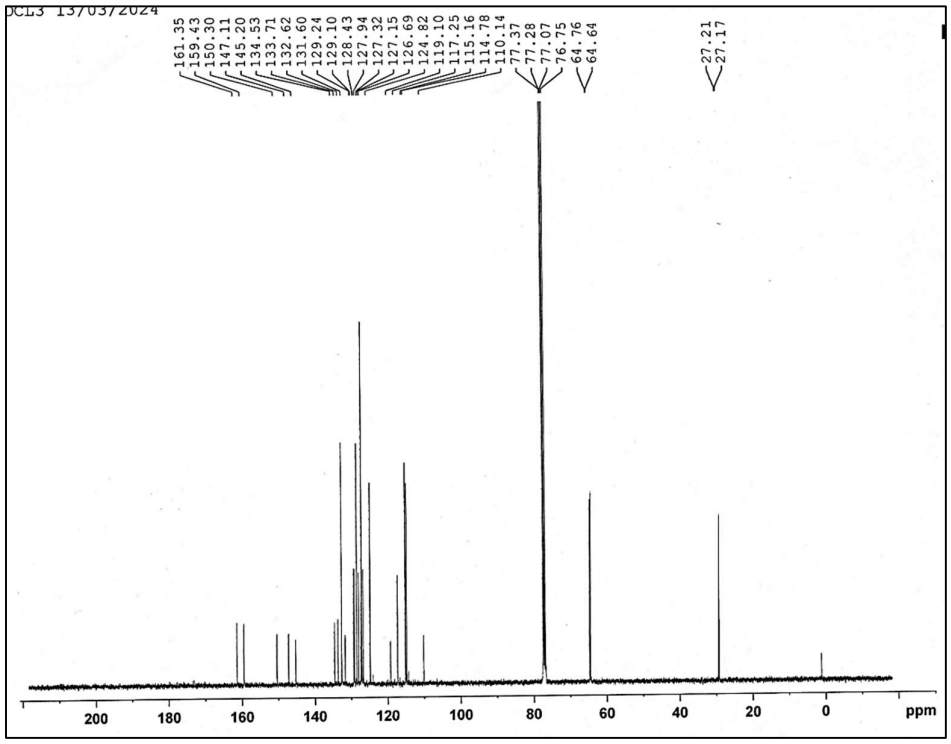

Fig. S4.9: ^{13}C-NMR spectra of *V-4*

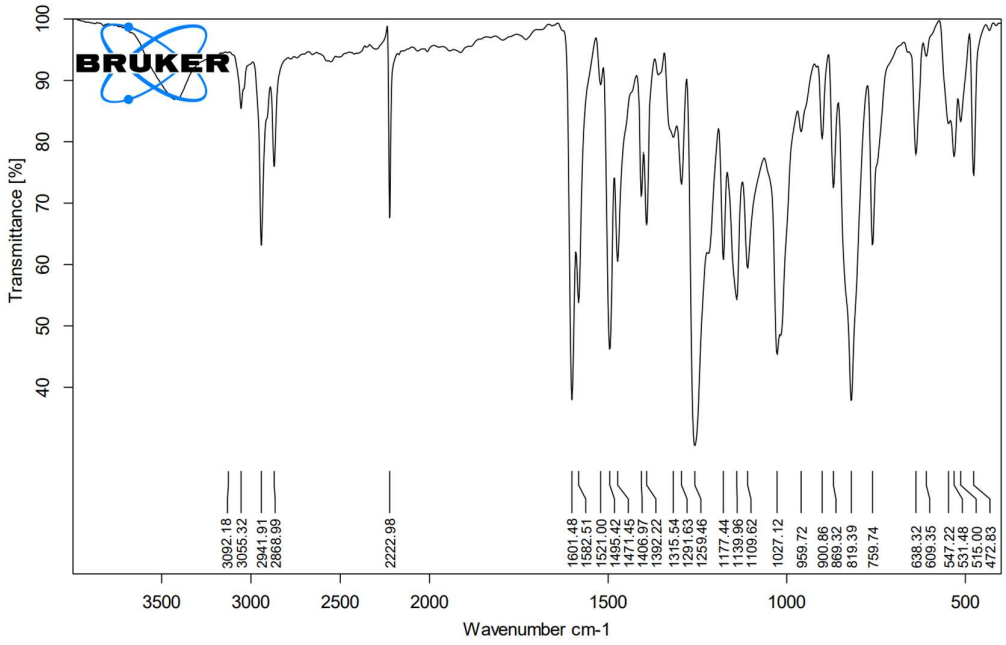

Fig. S4.10: FT-IR spectra of *V-5*

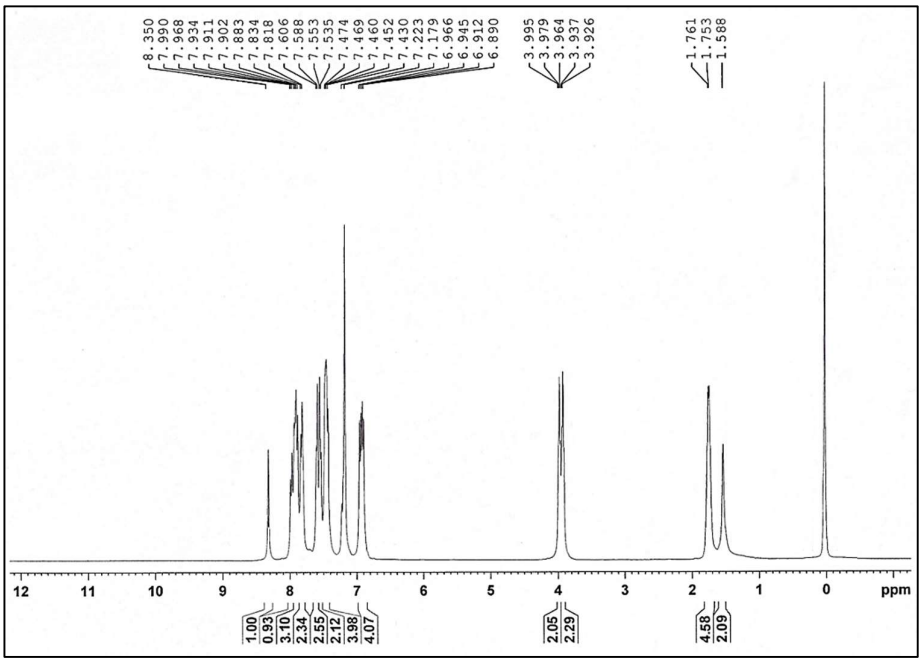

Fig. S4.11: ^{1}H-NMR spectra of *V-5*

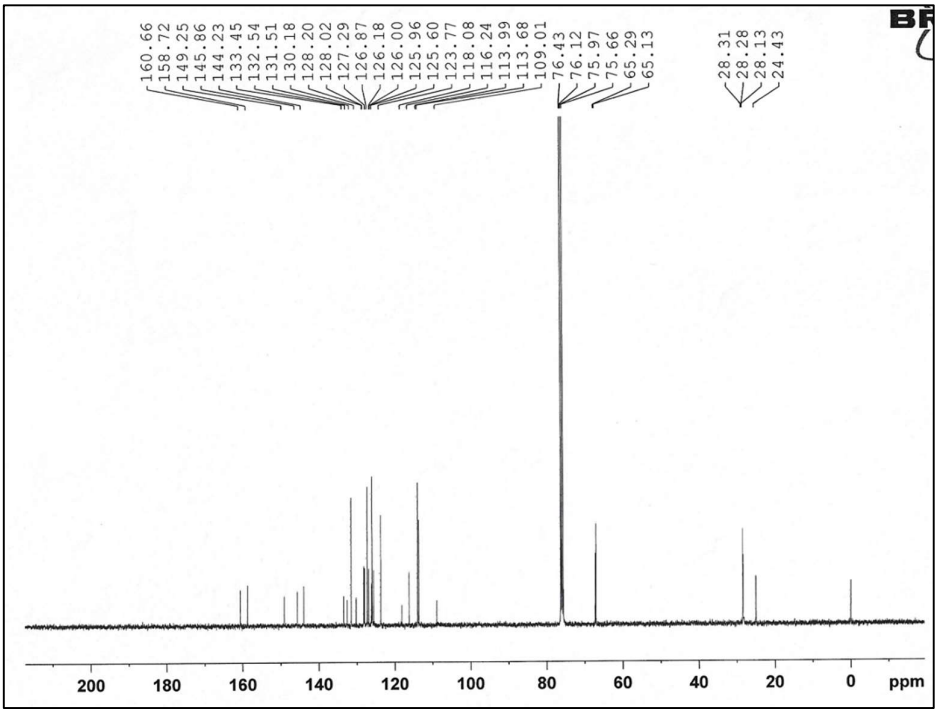

Fig. S4.12: ^{13}C-NMR spectra of *V-5*

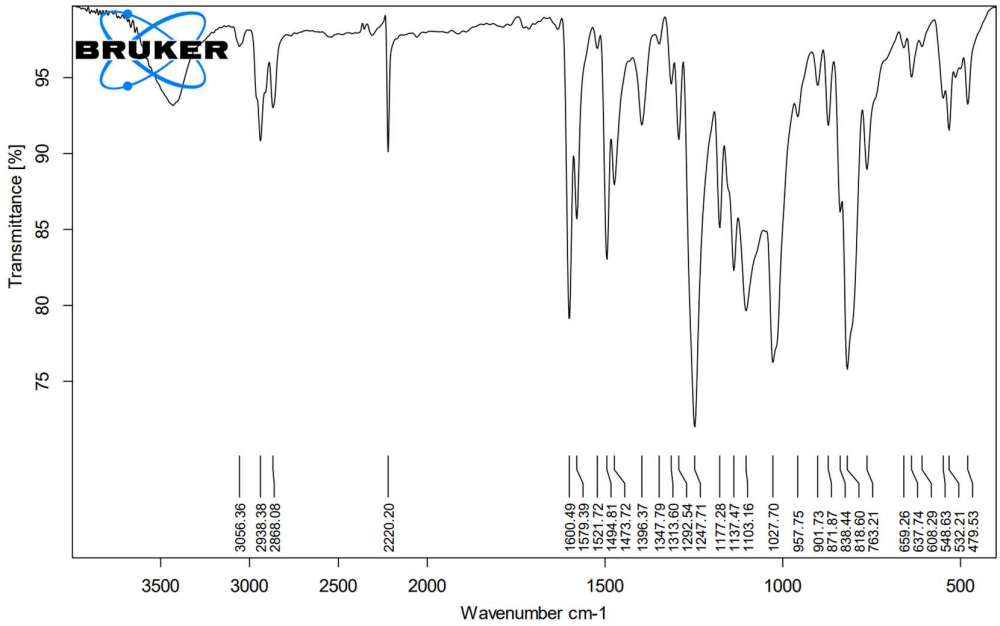

Fig. S4.13: FT-IR spectra of *V-6*

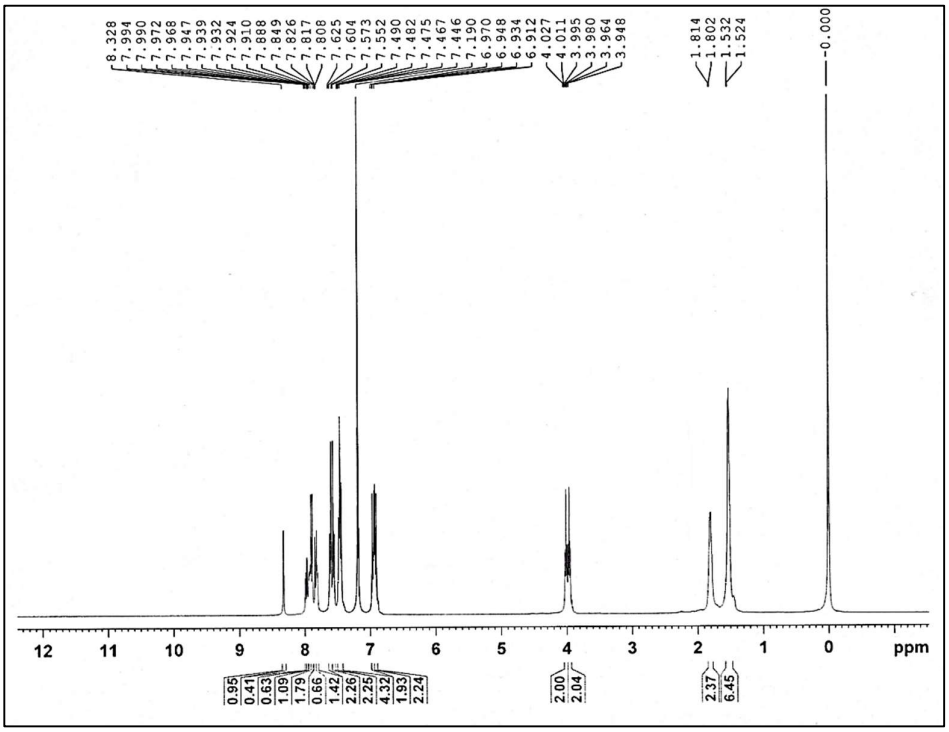

Fig. S4.14: ^{1}H-NMR spectra of *V-6*

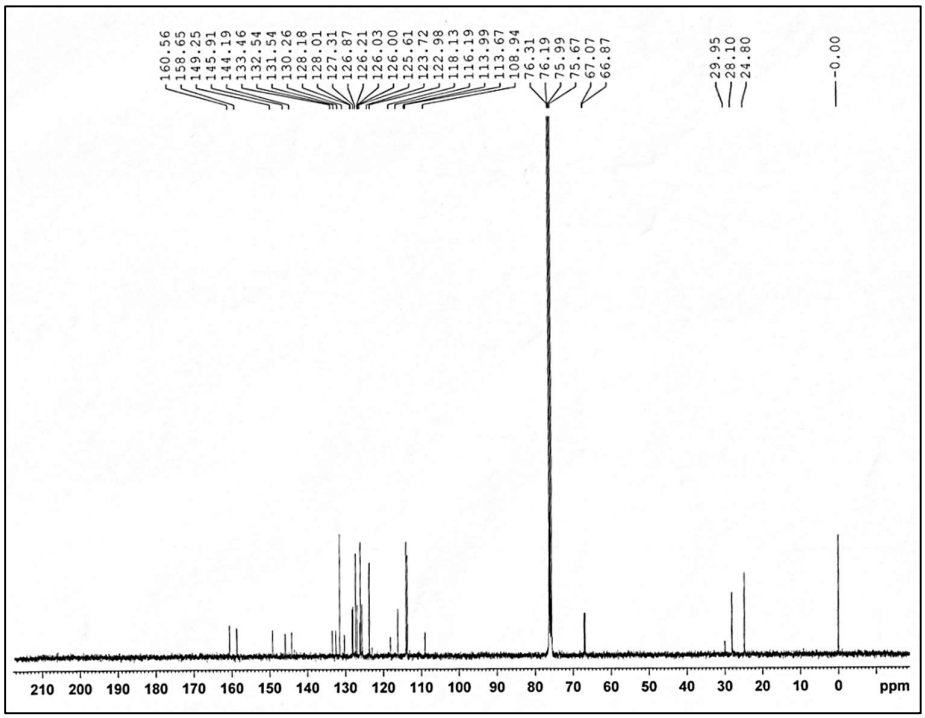

Fig. S4.15: ^{13}C-NMR spectra of *V-6*

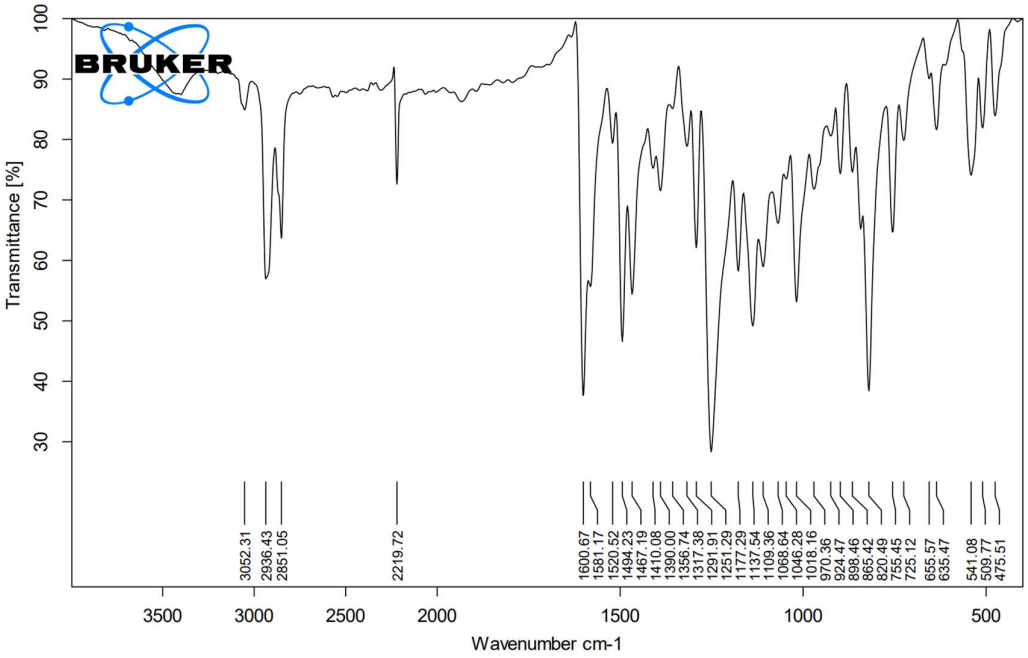

Fig. S4.16: FT-IR spectra of *V-8*

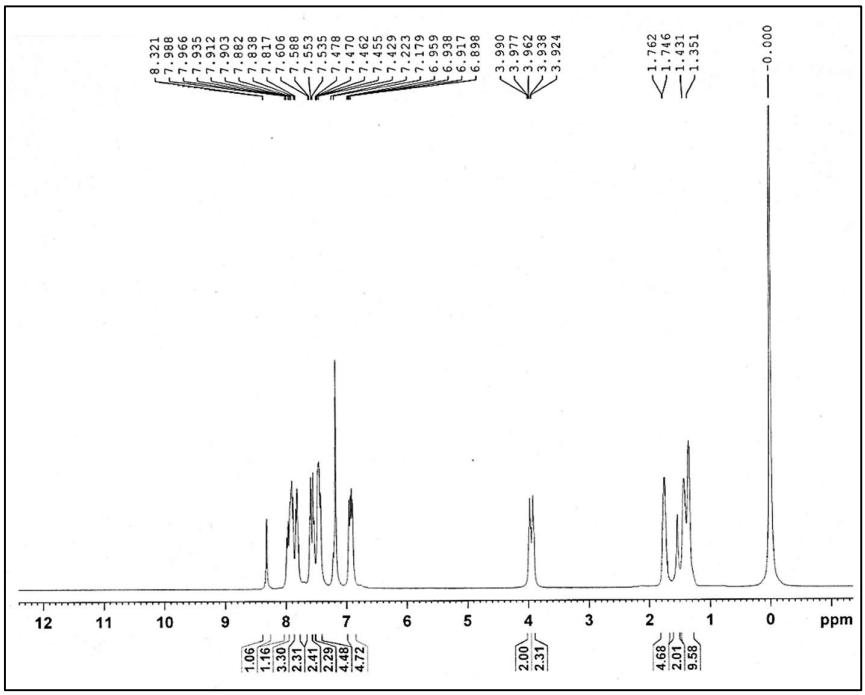

Fig. S4.17: ^{1}H-NMR spectra of *V-8*

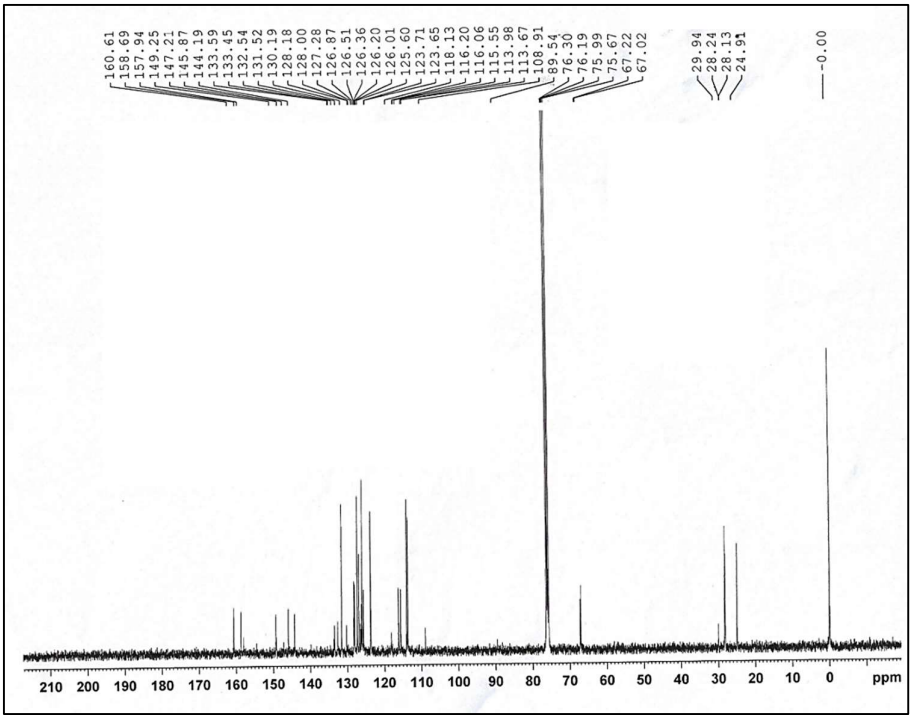

Fig. S4.18: ^{13}C-NMR spectra of *V-8*

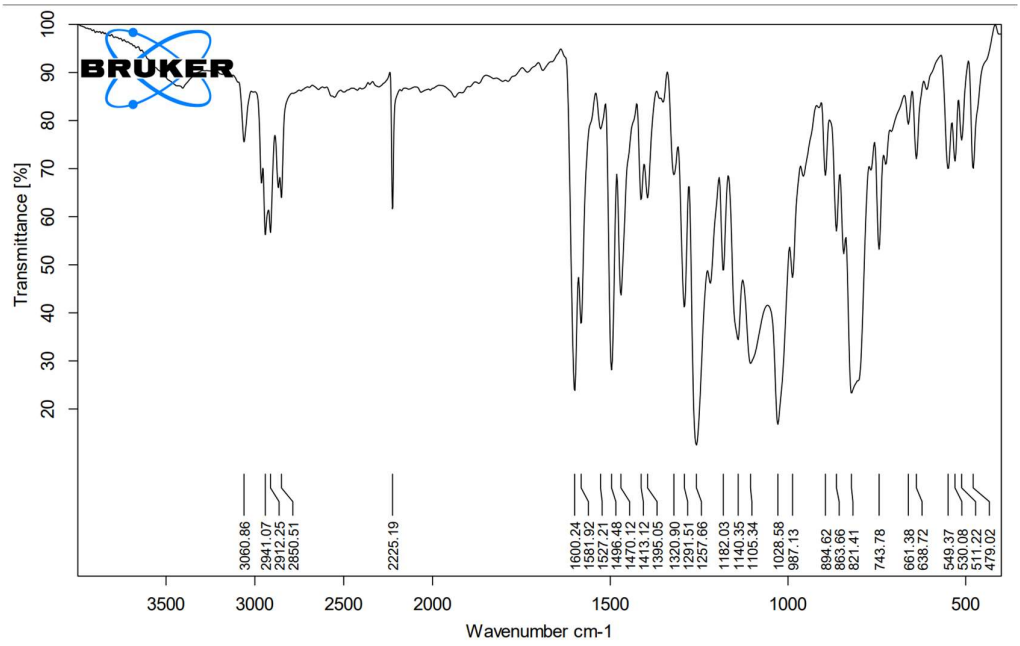

Fig. S4.19: FT-IR spectra of *V-9*

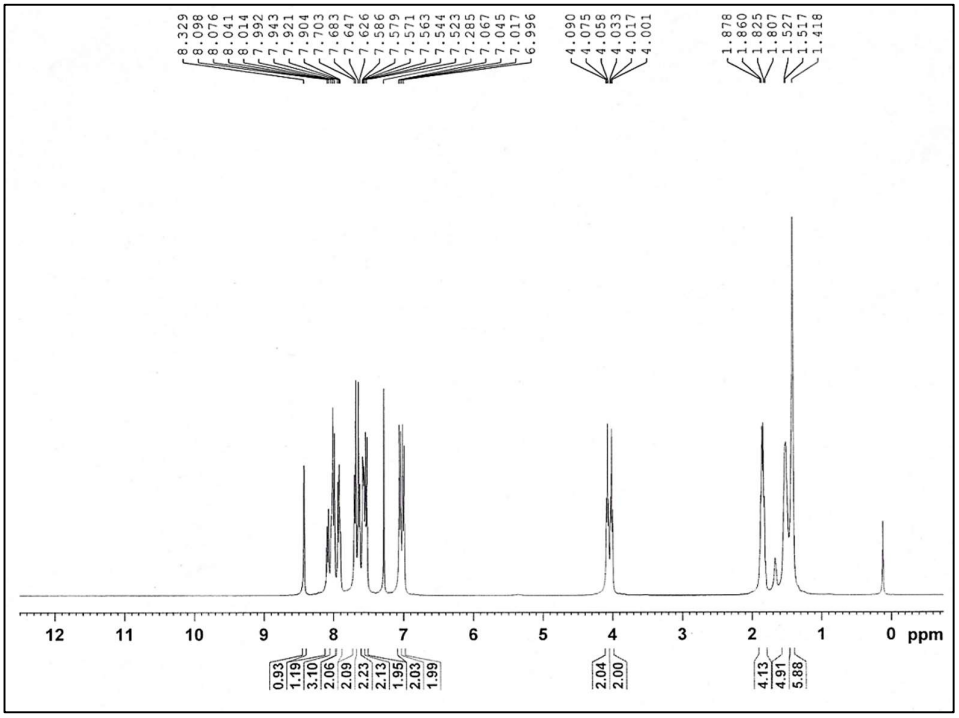

Fig. S4.20: ^{1}H-NMR spectra of *V-9*

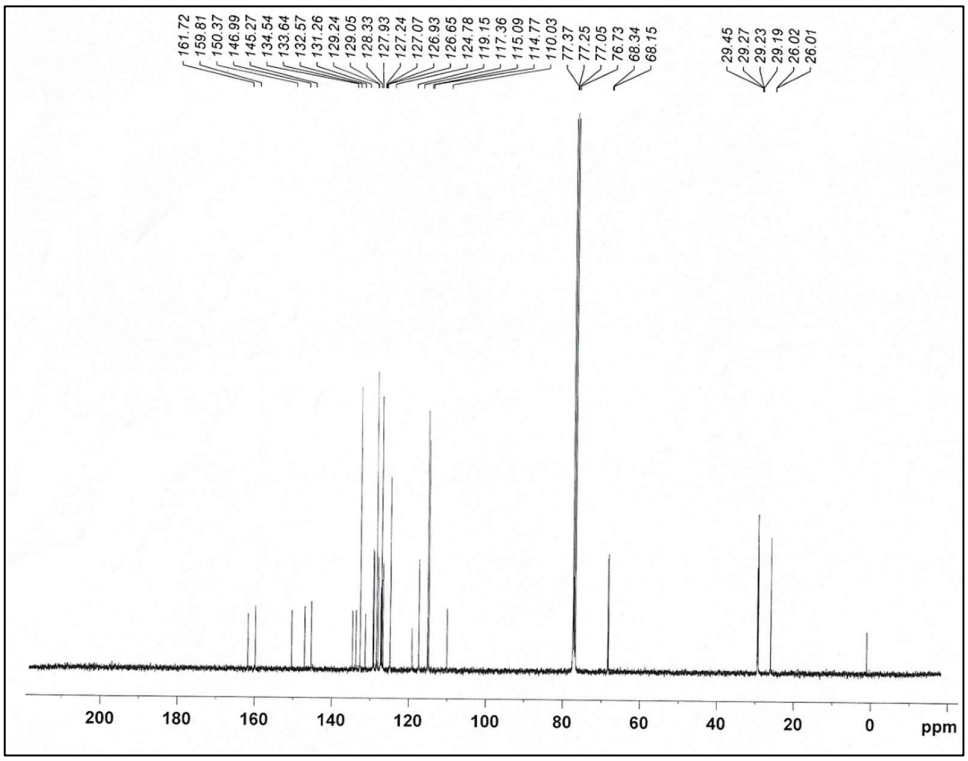

Fig. S4.21: ^{13}C-NMR spectra of *V-9*

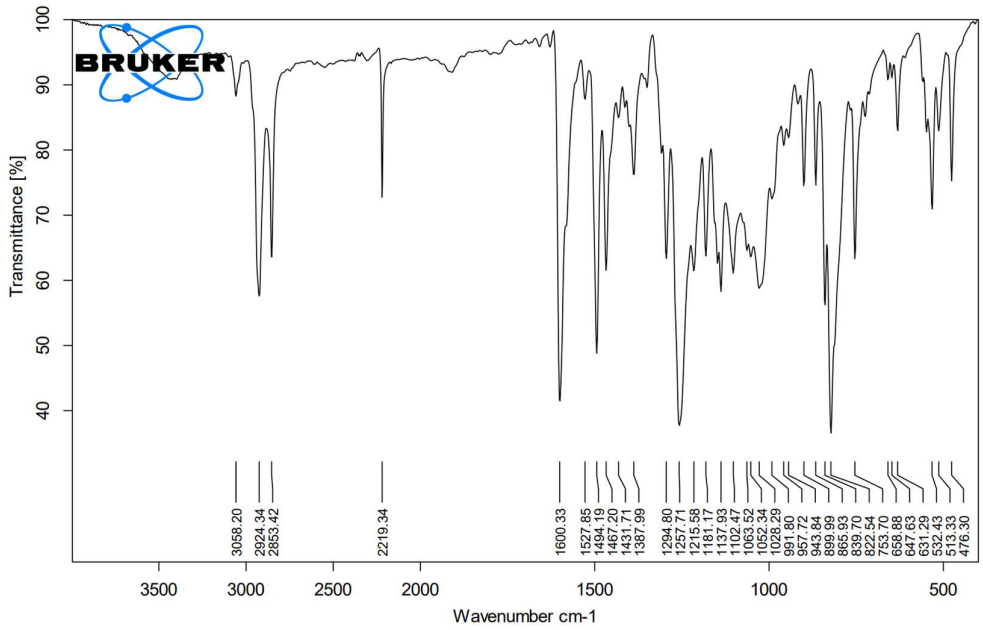

Fig. S4.22: FT-IR spectra of *V-10*

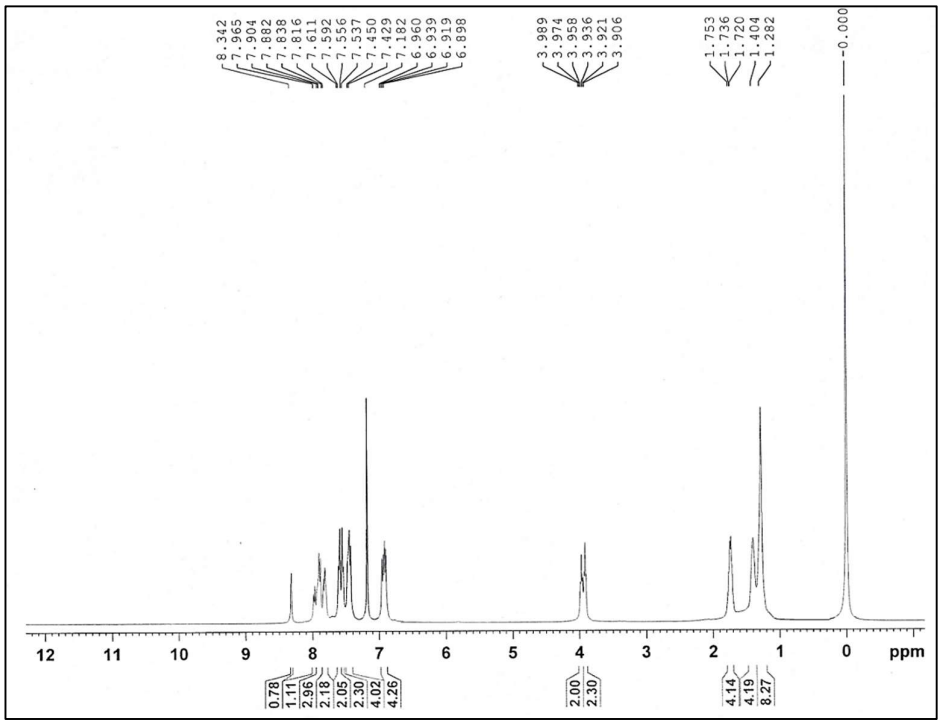

Fig. S4.23: ^{1}H-NMR spectra of *V-10*

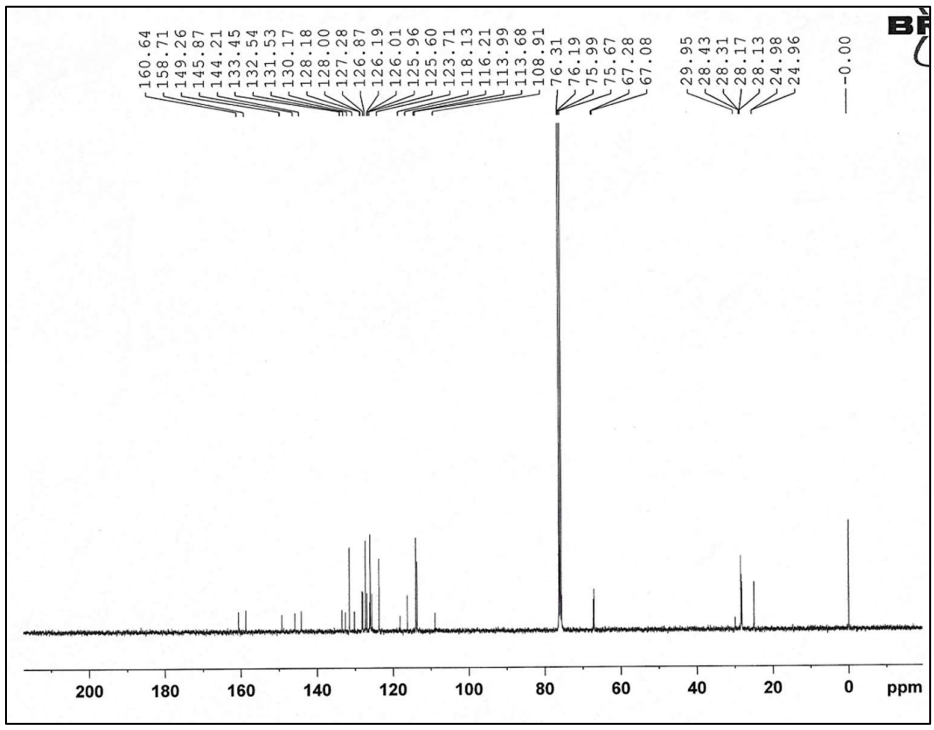

Fig. S4.24: ^{13}C-NMR spectra of *V-10*

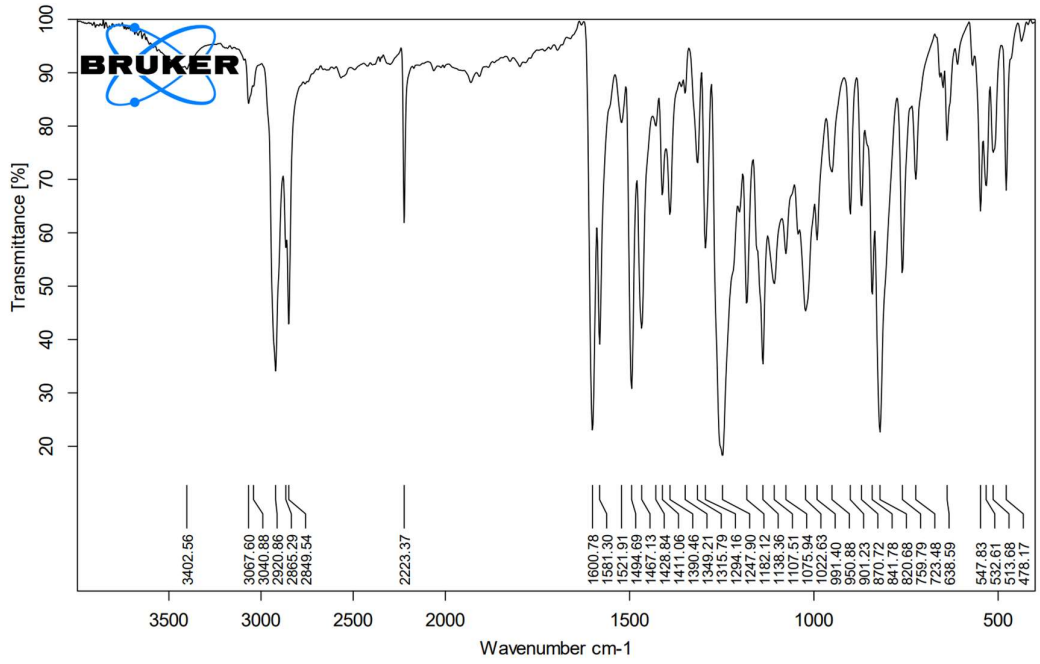

Fig. S4.25: FT-IR spectra of *V-11*

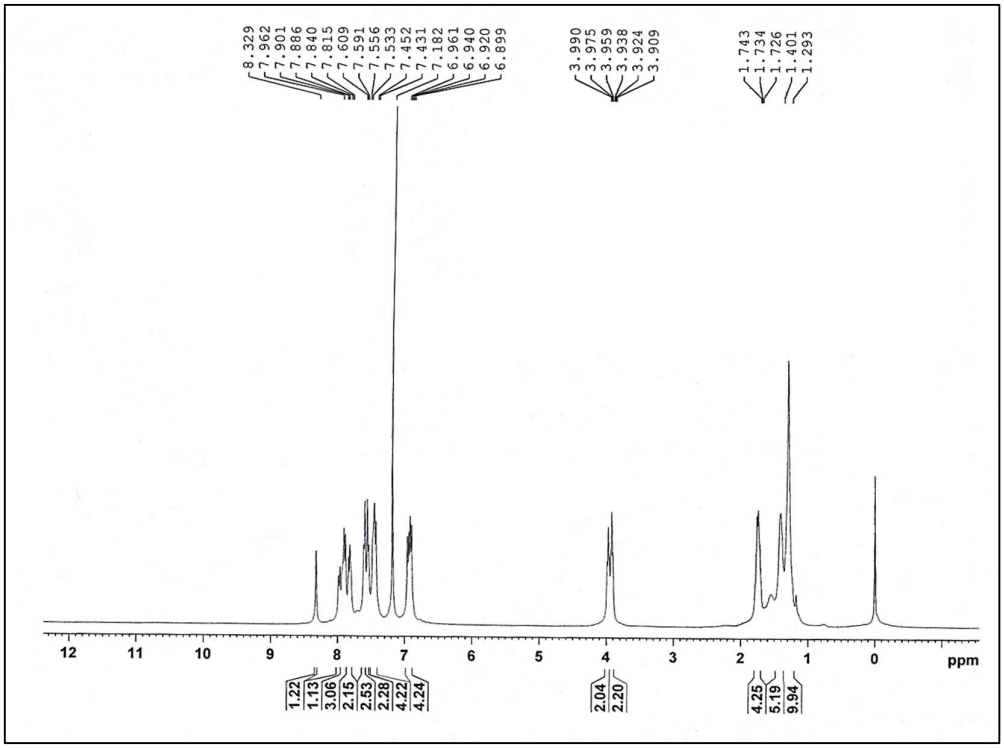

Fig. S4.26: ^{1}H-NMR spectra of *V-11*

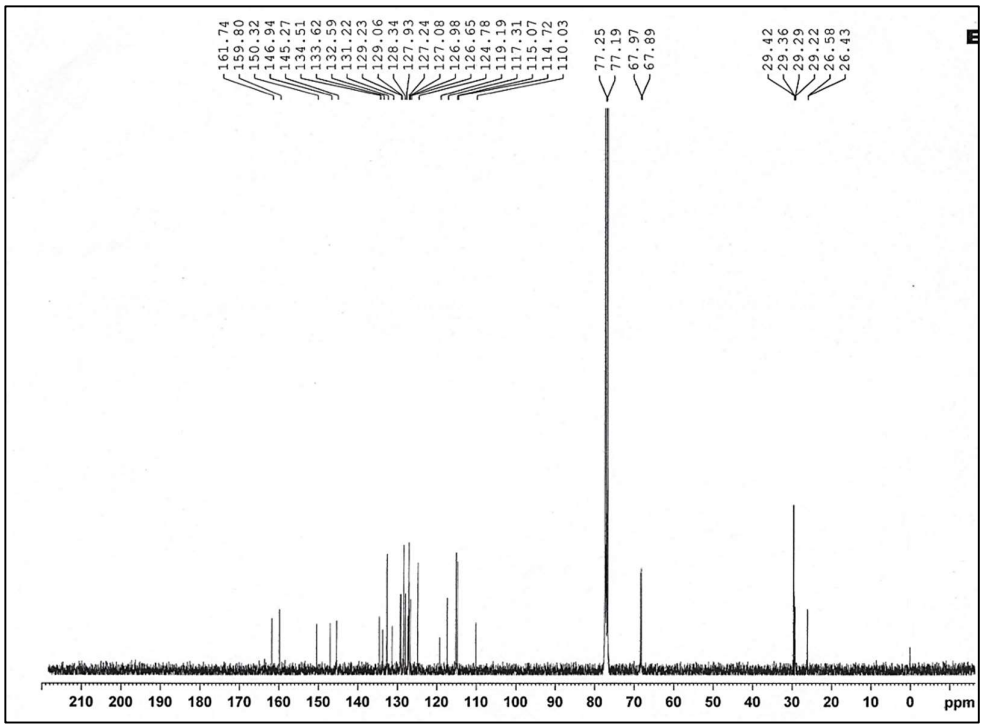

Fig. S4.27: ^{13}C-NMR spectra of *V-11*

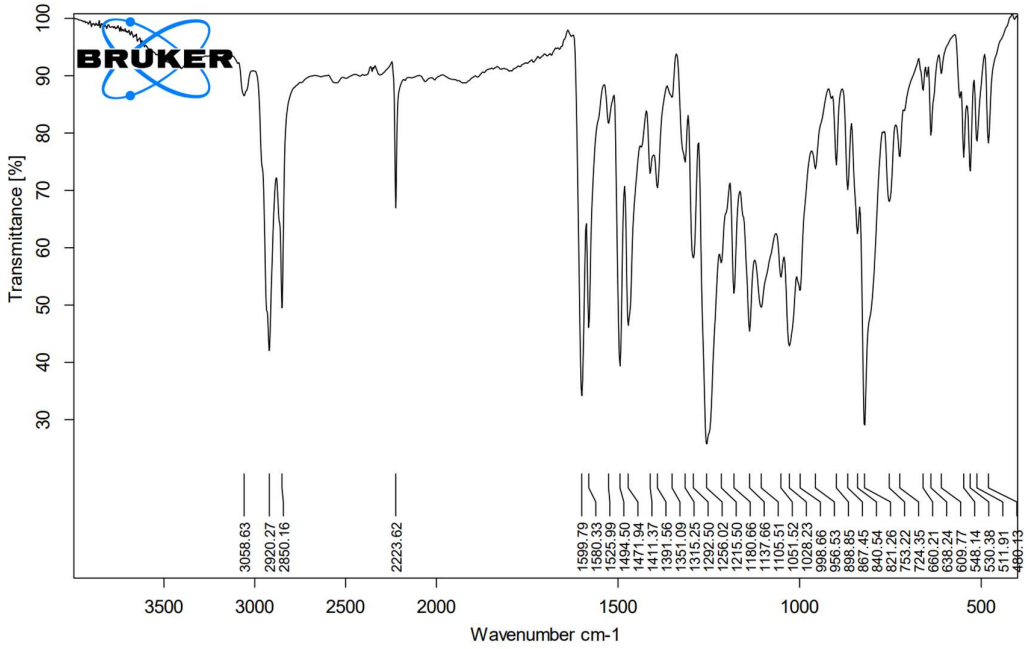

Fig. S4.28: FT-IR spectra of *V-12*

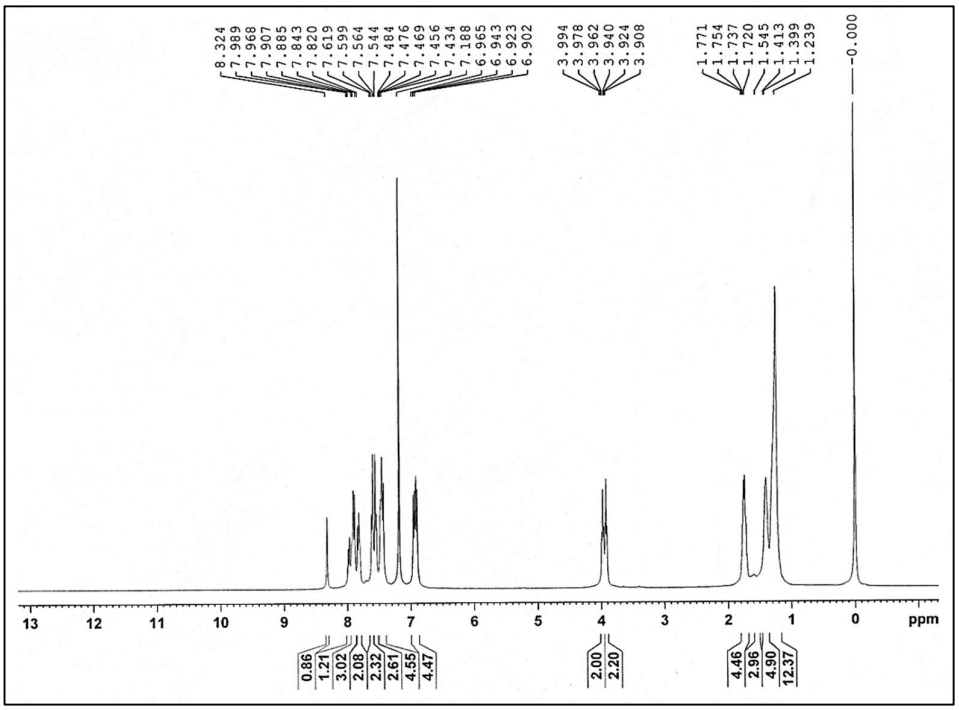

Fig. S4.29: ^{1}H-NMR spectra of *V-12*

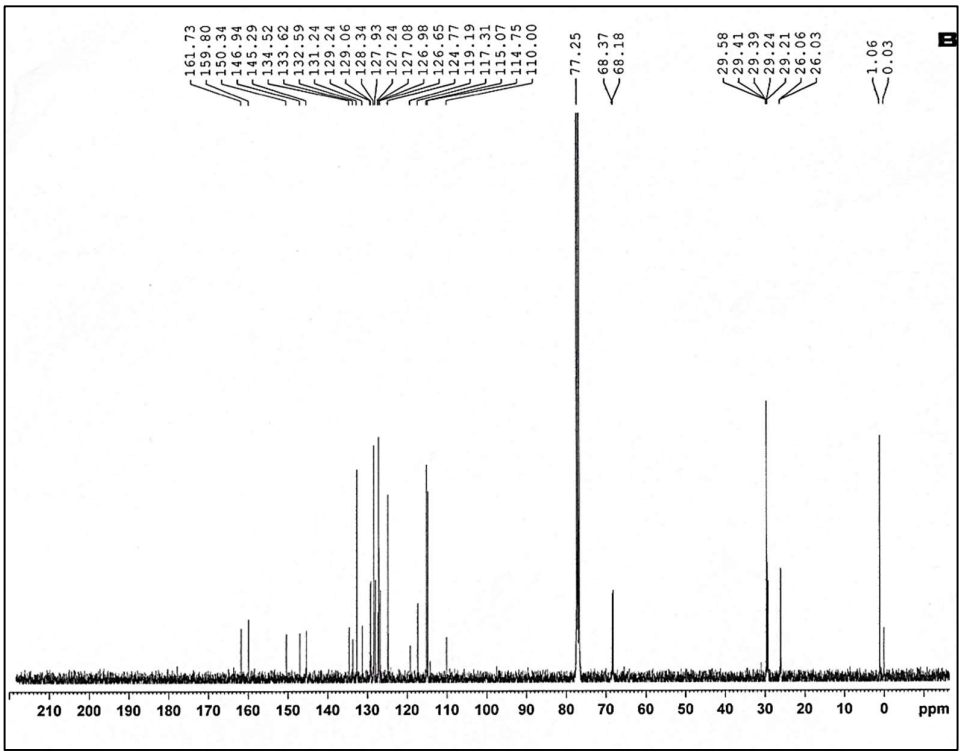

Fig. S4.30: ^{13}C-NMR spectra of *V-12*

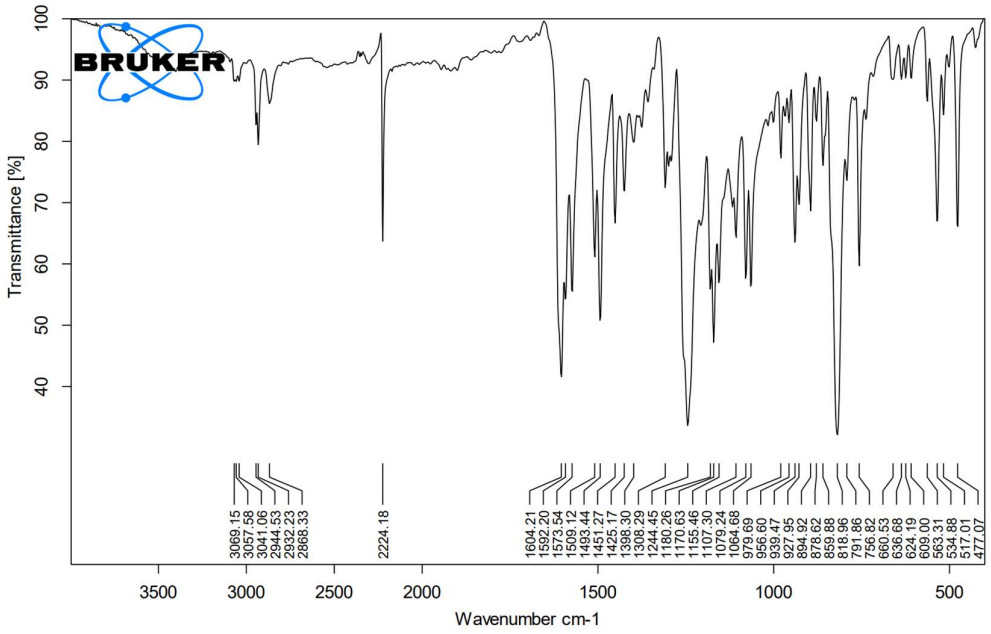

Fig. S4.31: FT-IR spectra of *VI-2*

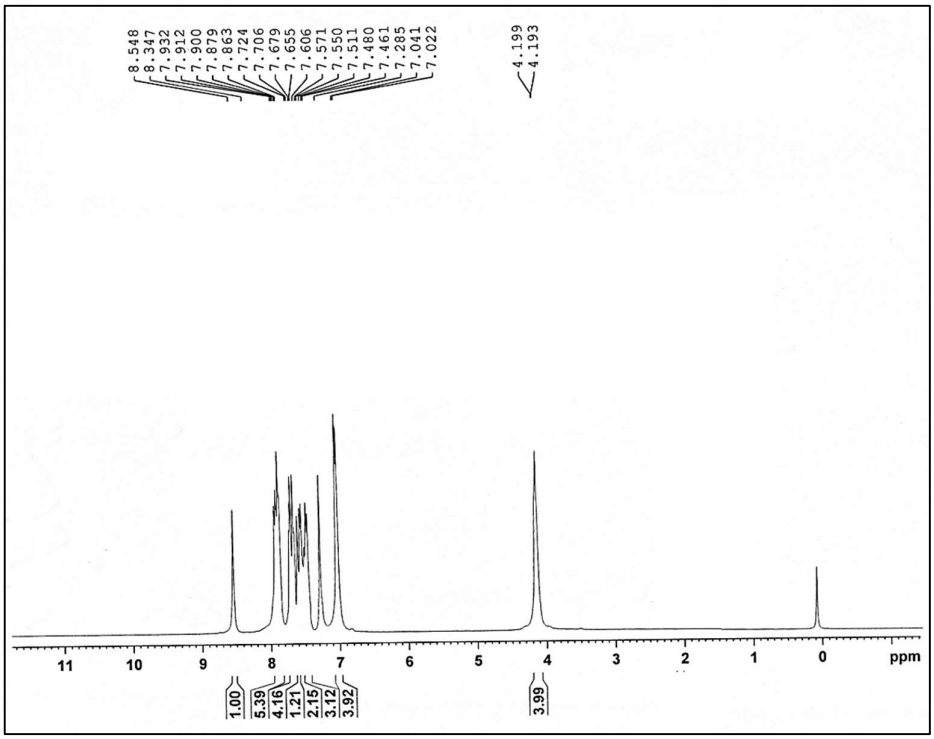

Fig. S4.32: ^{1}H-NMR spectra of *VI-2*

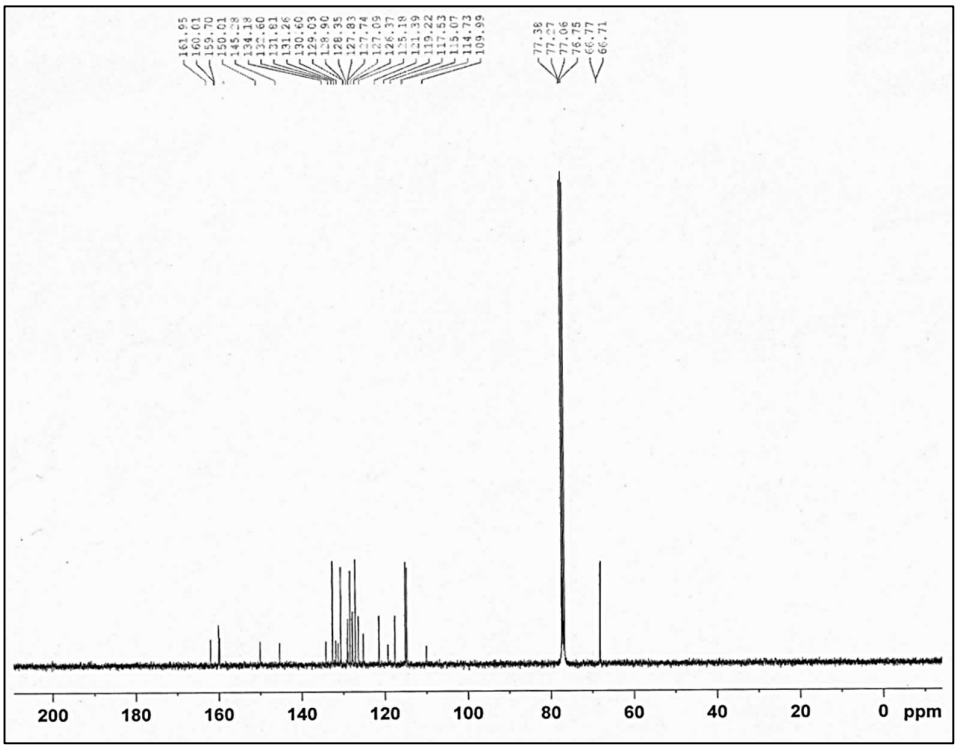

Fig. S4.33: ^{13}C-NMR spectra of *VI-2*

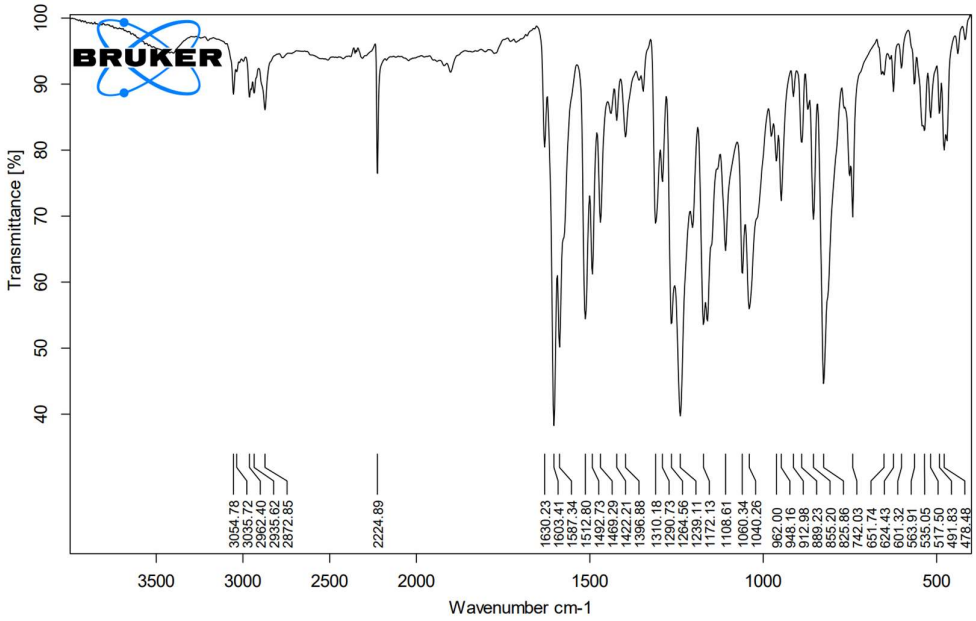

Fig. S4.34: FT-IR spectra of *VI-3*

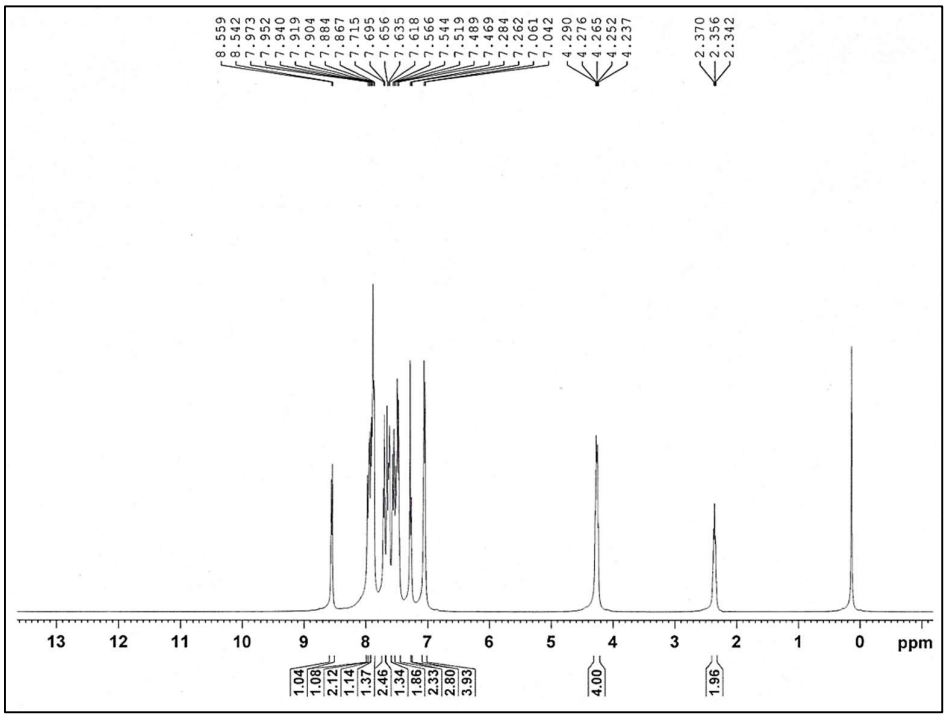

Fig. S4.35: ^{1}H-NMR spectra of *VI-3*

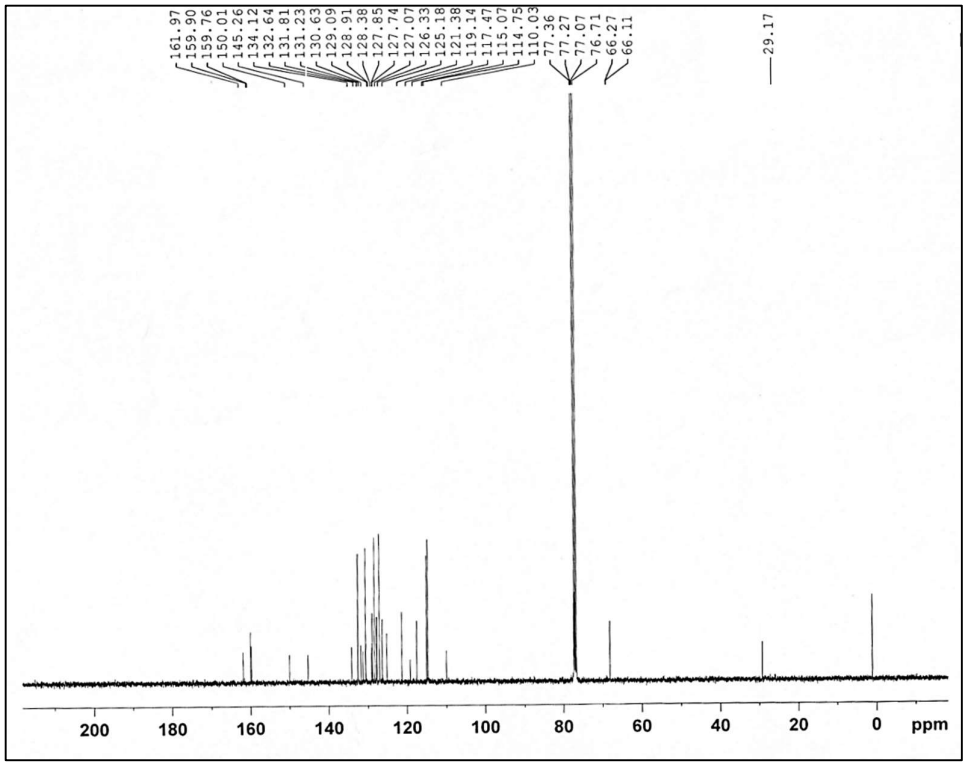

Fig. S4.36: ^{13}C-NMR spectra of *VI-3*

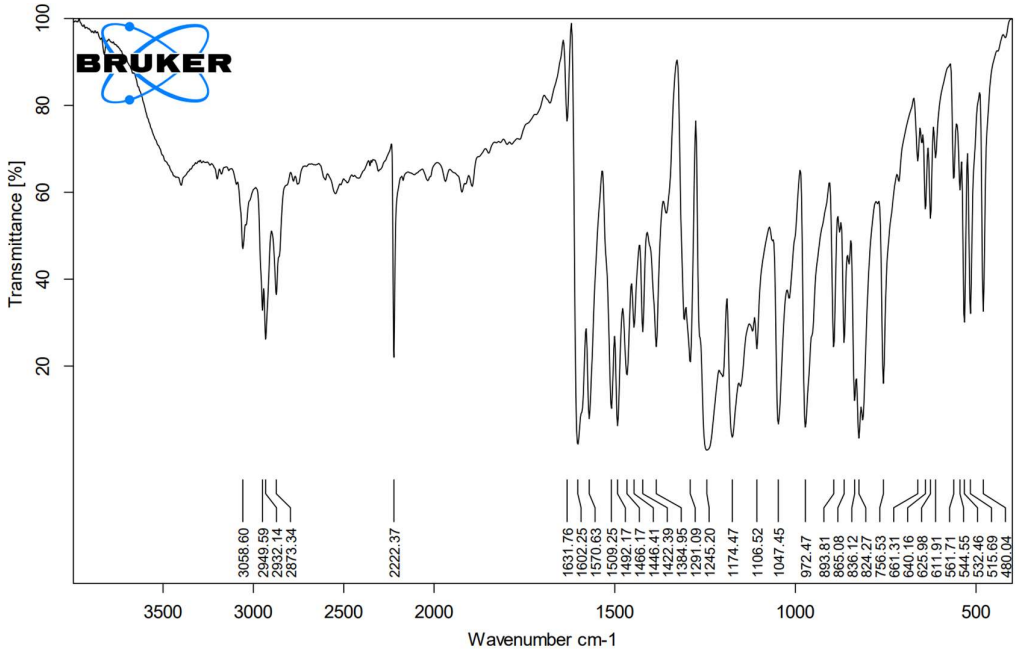

Fig. S4.37: FT-IR spectra of *VI-4*

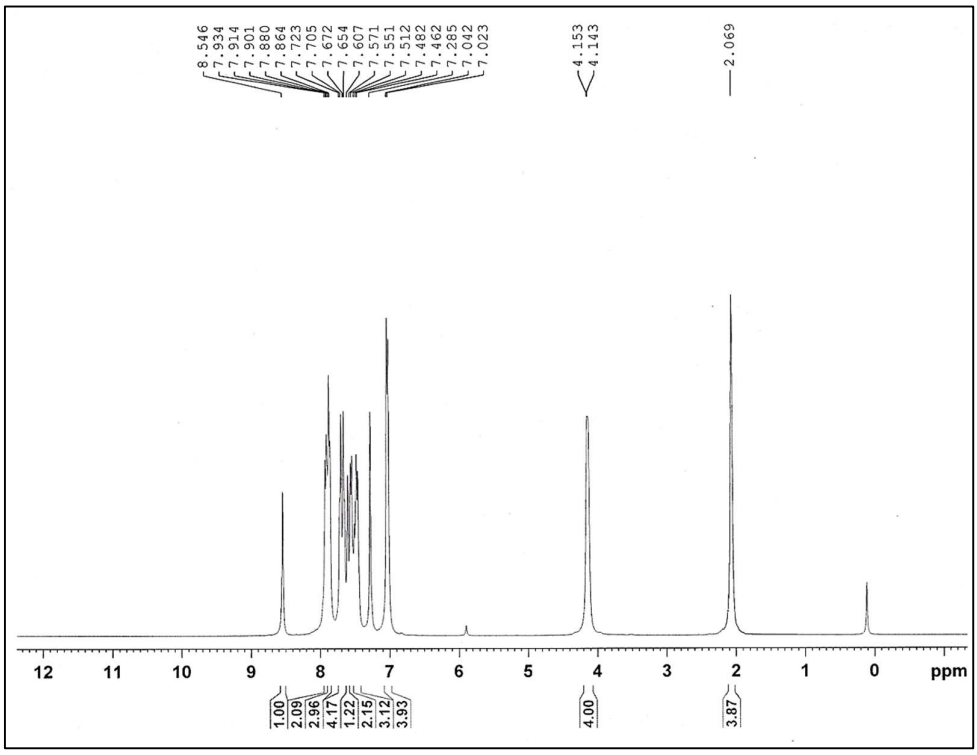

Fig. S4.38: ^{1}H-NMR spectra of *VI-4*

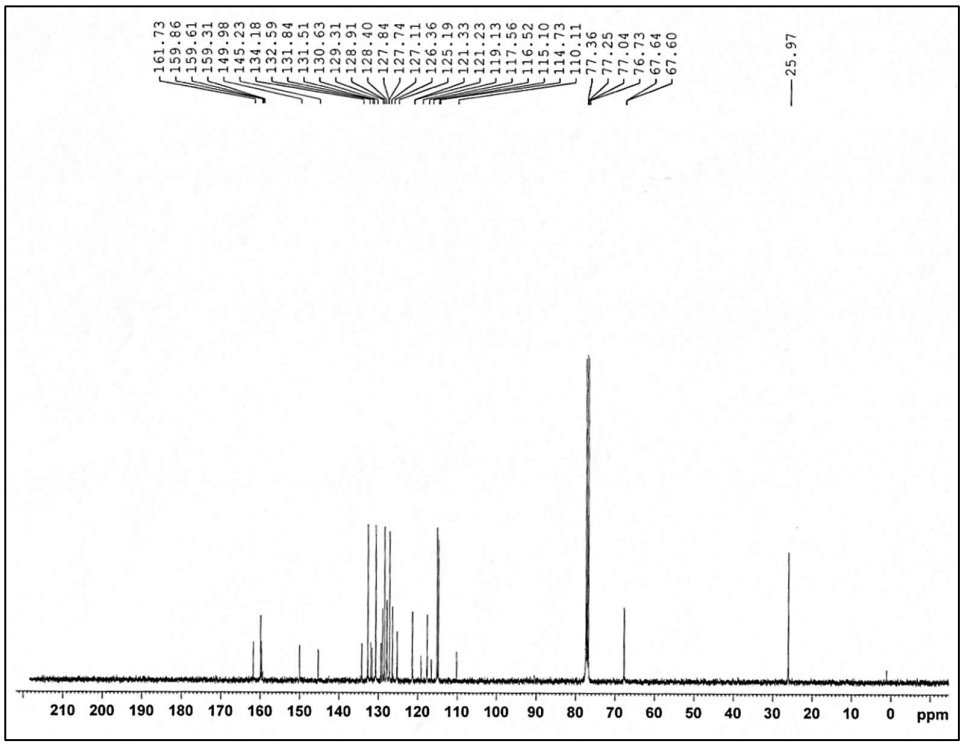

Fig. S4.39: ^{13}C-NMR spectra of *VI-4*

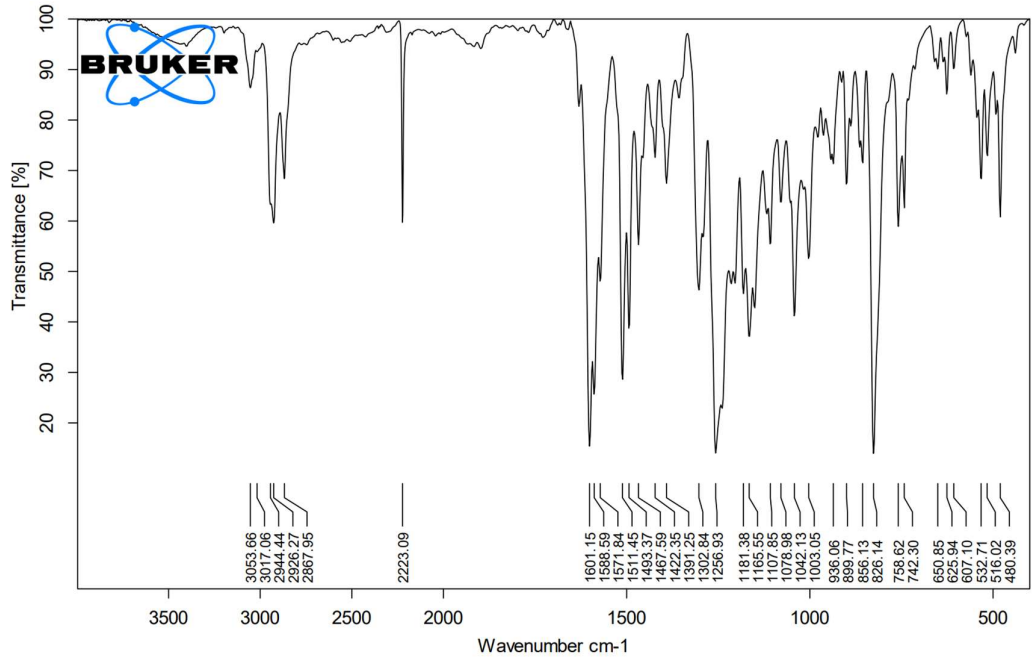

Fig. S4.40: FT-IR spectra of *VI-5*

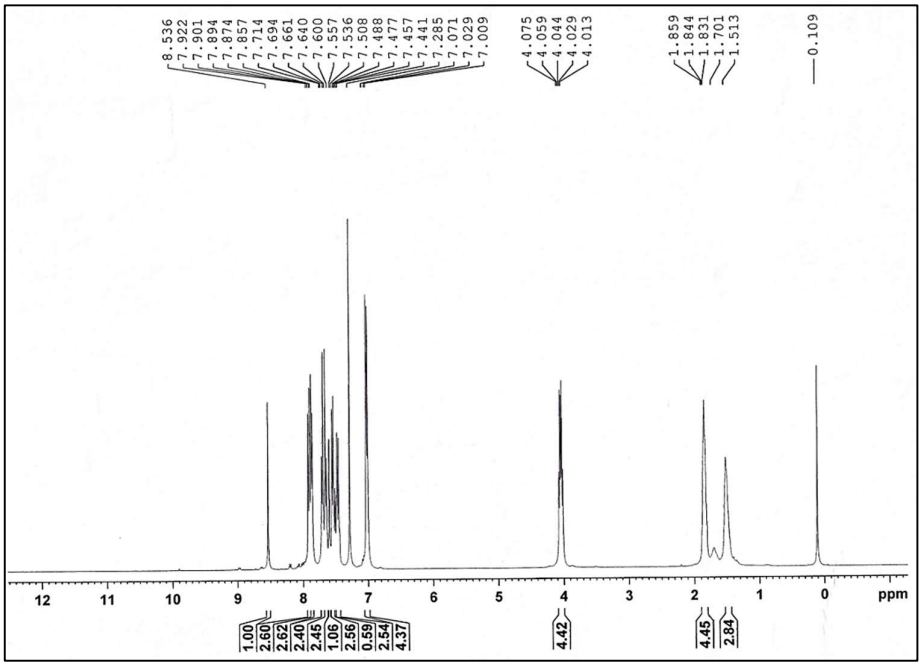

Fig. S4.41: ^{1}H-NMR spectra of *VI-5*

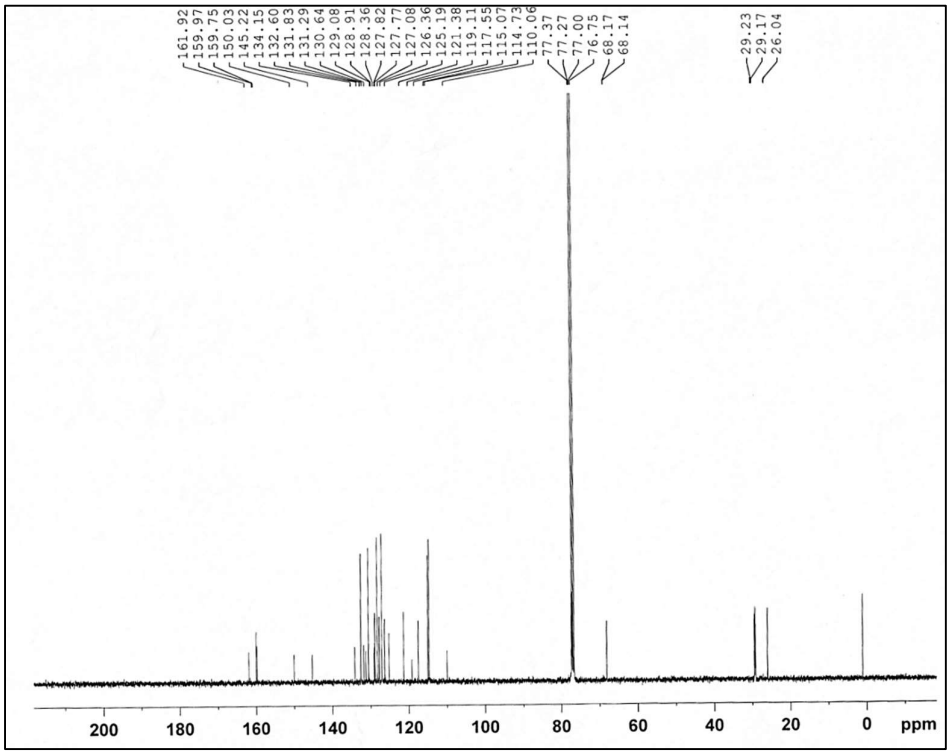

Fig. S4.42: ^{13}C-NMR spectra of *VI-5*

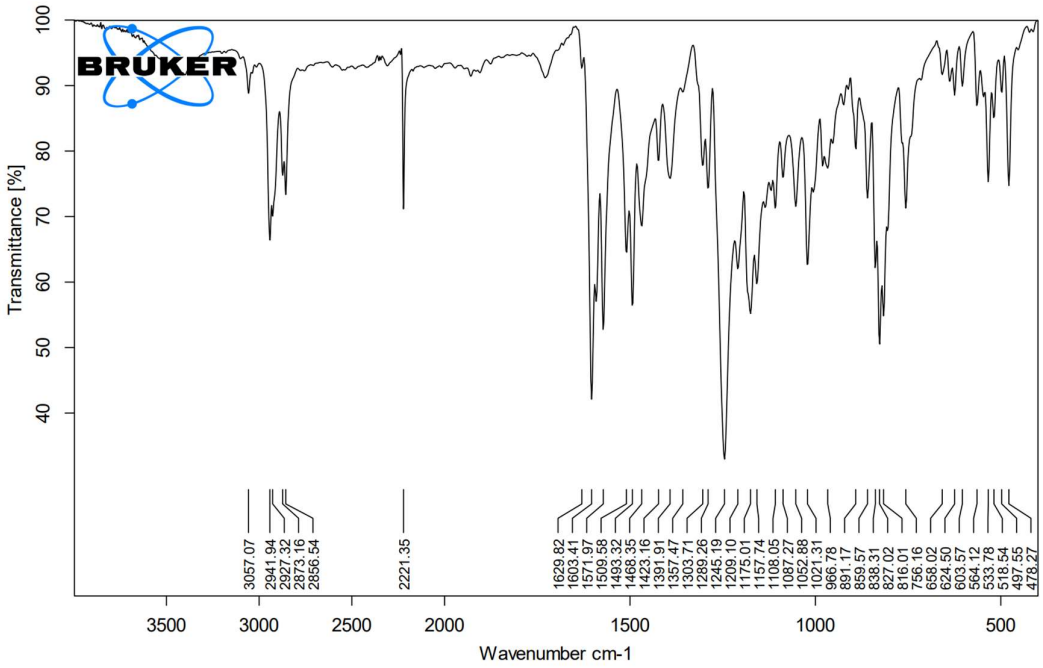

Fig. S4.43: FT-IR spectra of *VI-6*

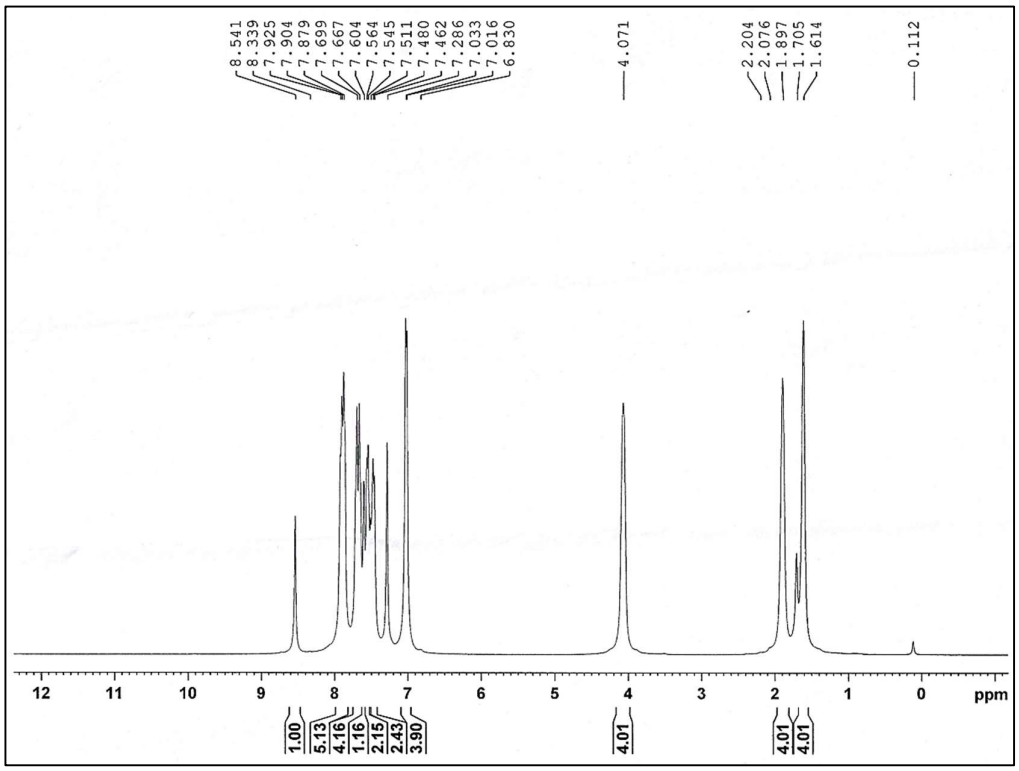

Fig. S4.44: ^{1}H-NMR spectra of *VI-6*

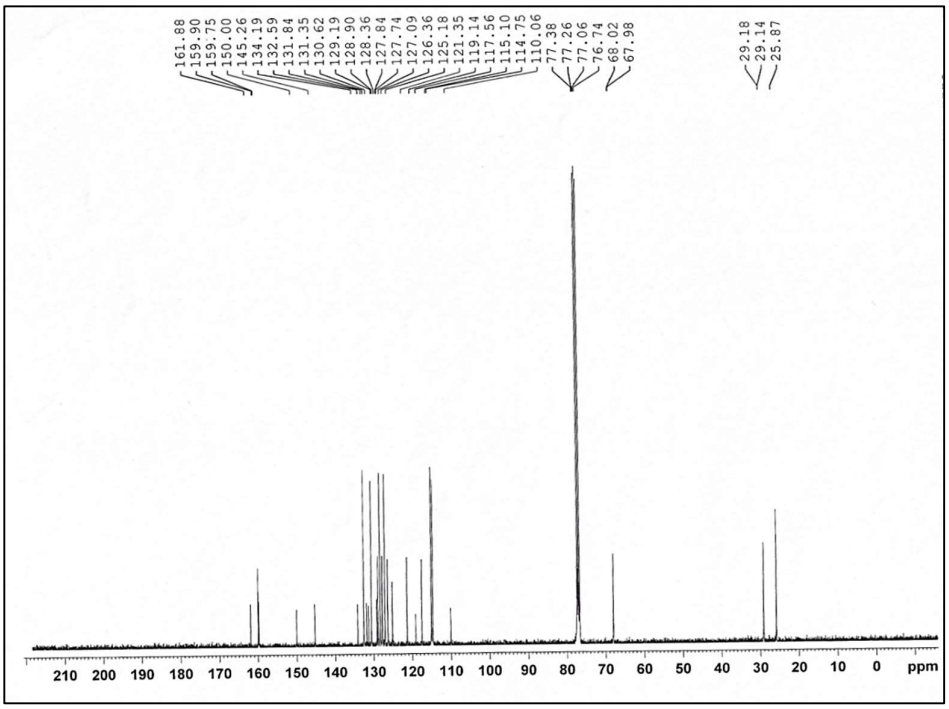

Fig. S4.45: ^{13}C-NMR spectra of *VI-6*

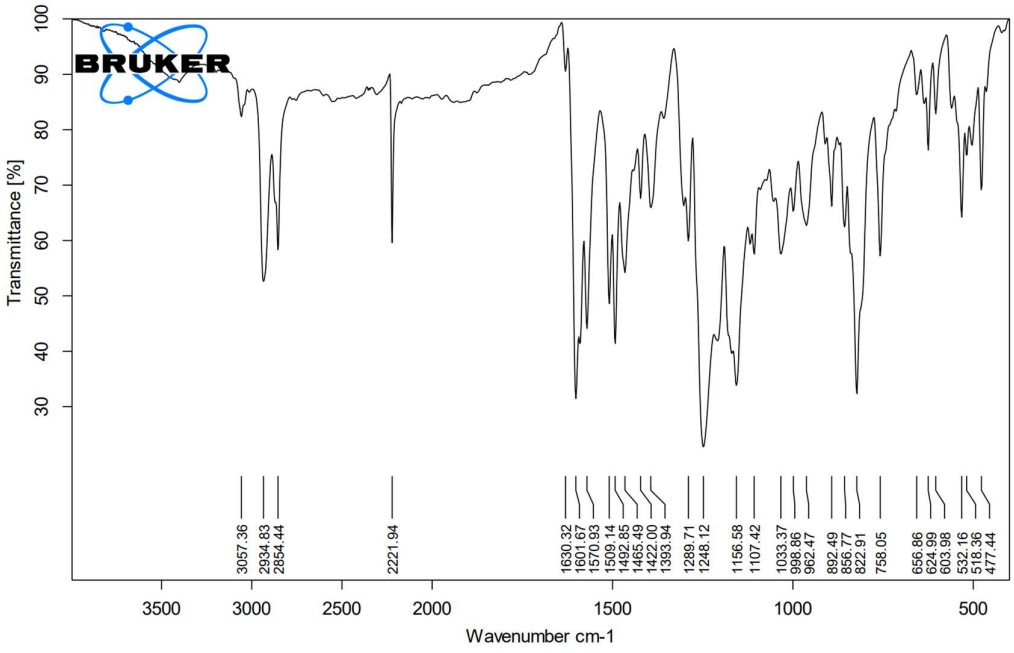

Fig. S4.46: FT-IR spectra of *VI-8*

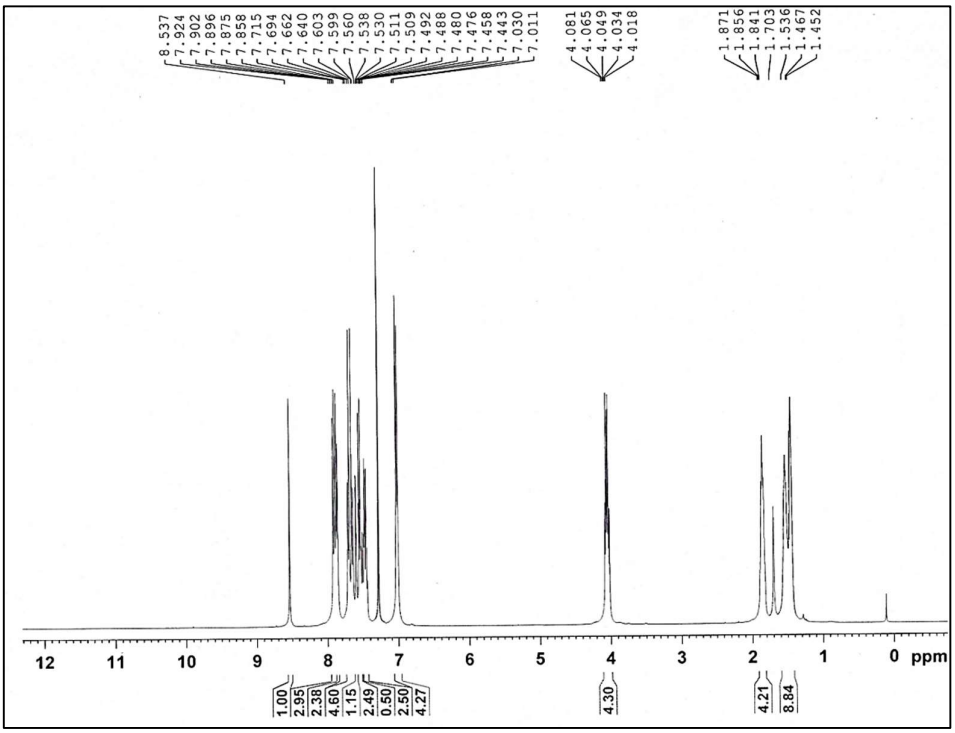

Fig. S4.47: ^{1}H-NMR spectra of *VI-8*

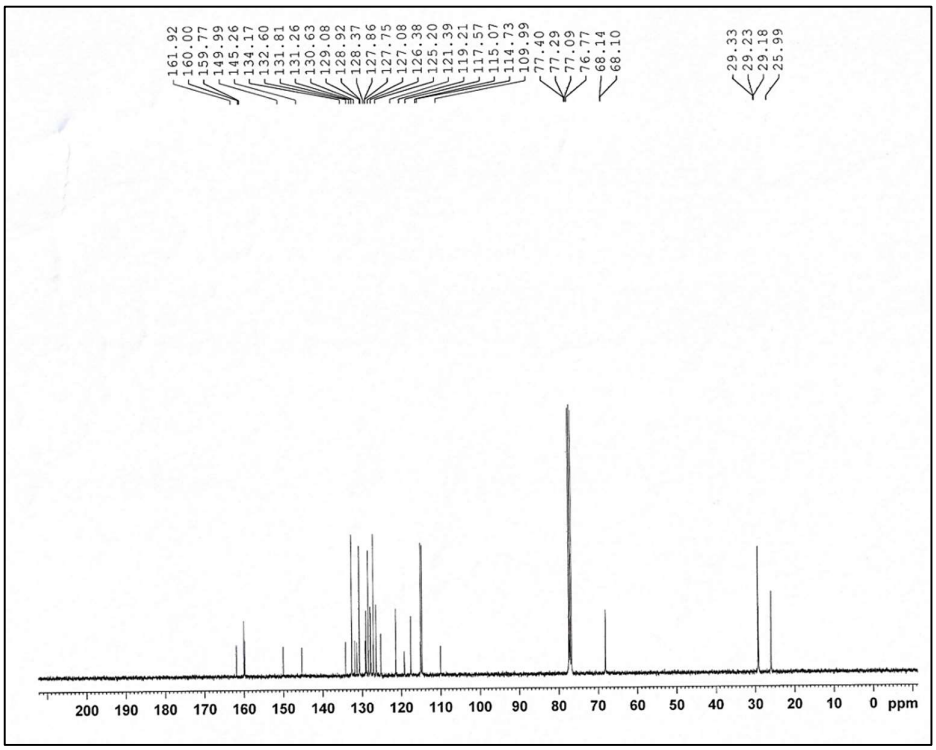

Fig. S4.48: ^{13}C-NMR spectra of *VI-8*

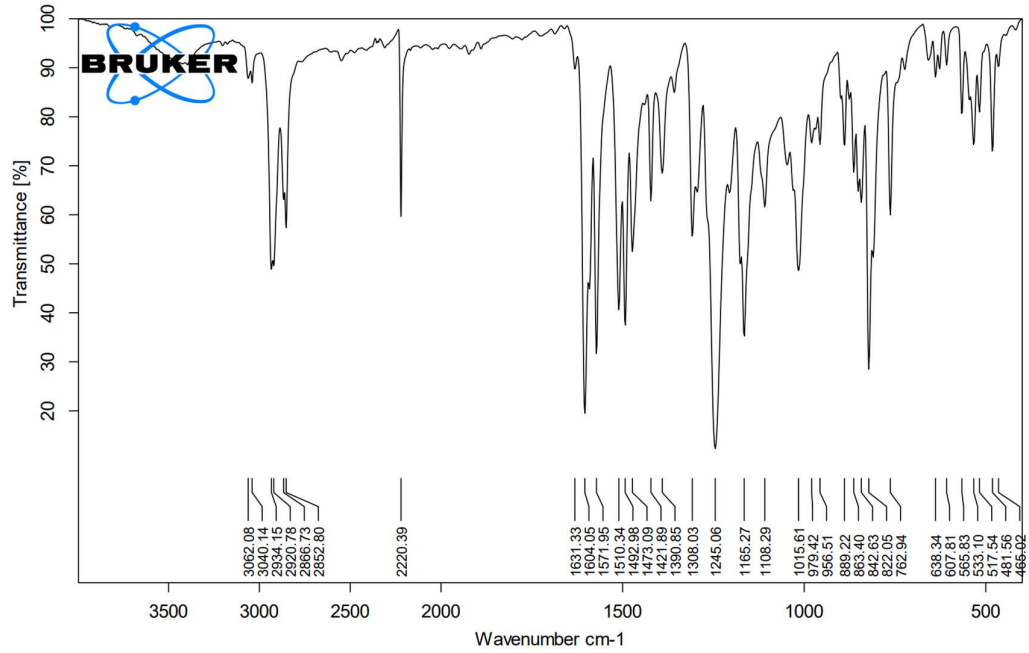

Fig. S4.49: FT-IR spectra of *VI-9*

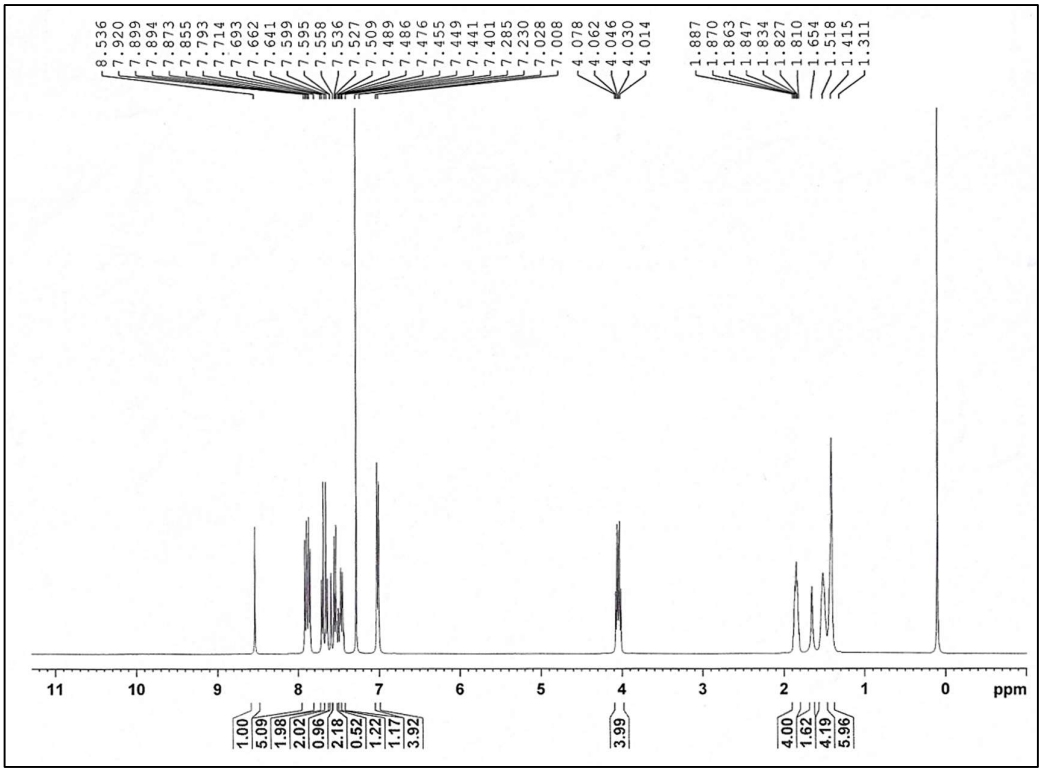

Fig. S4.50: ^{1}H-NMR spectra of *VI-9*

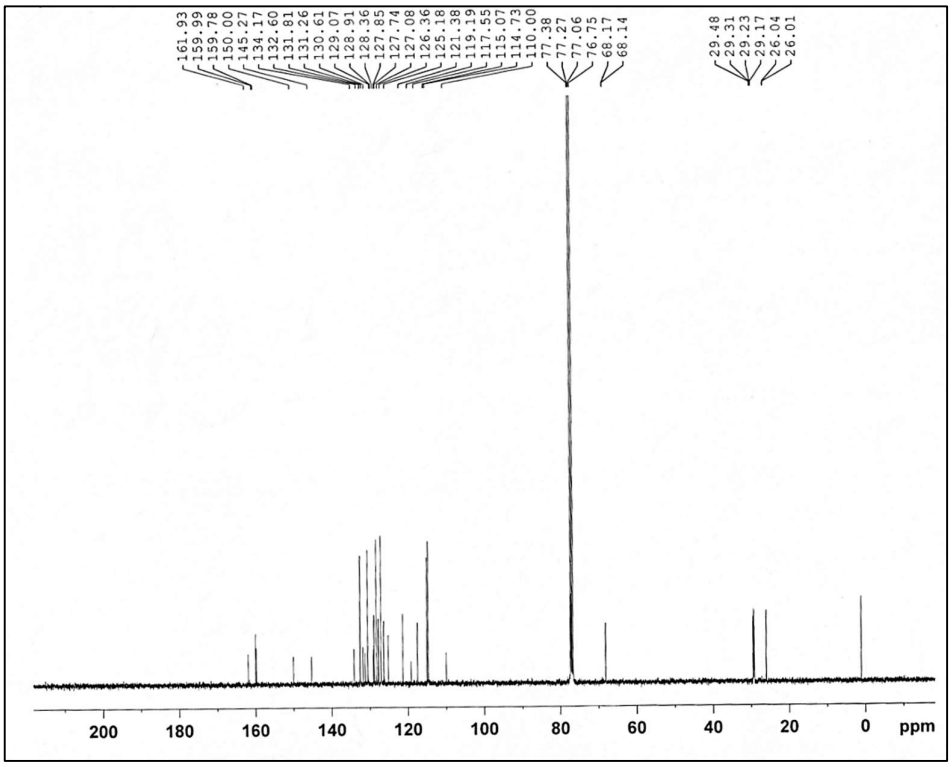

Fig. S4.51: ^{13}C-NMR spectra of *VI-9*

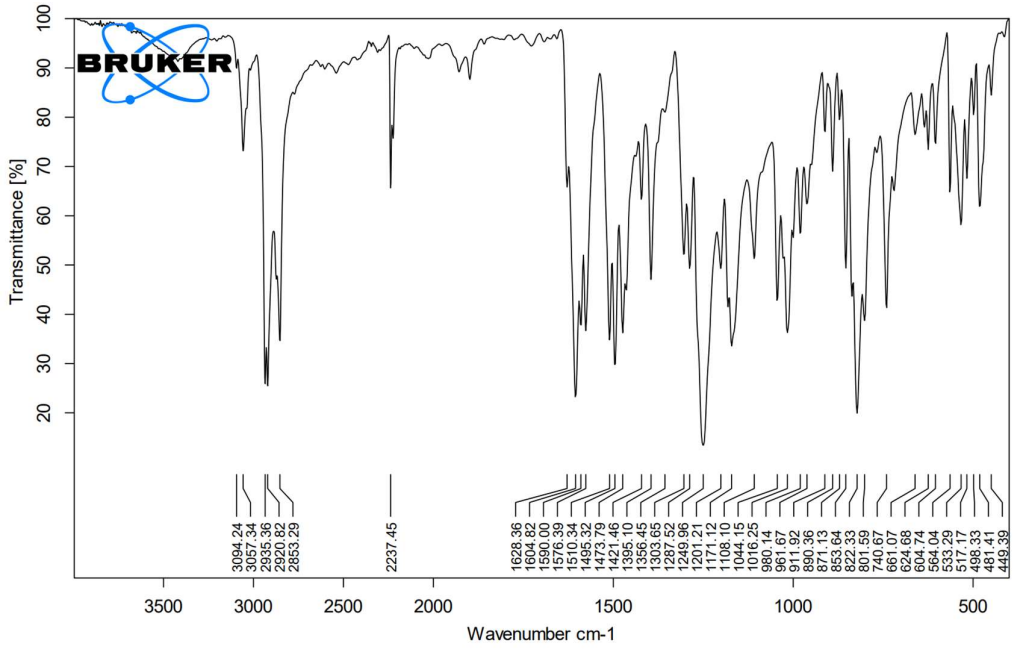

Fig. S4.52: FT-IR spectra of *VI-10*

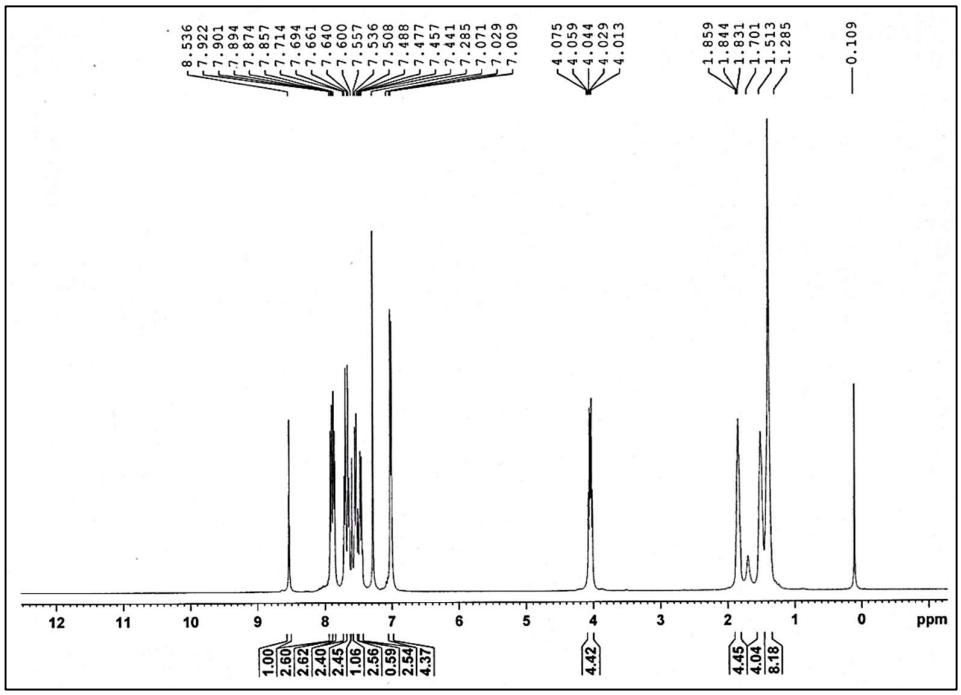

Fig. S4.53: ^{1}H-NMR spectra of *VI-10*

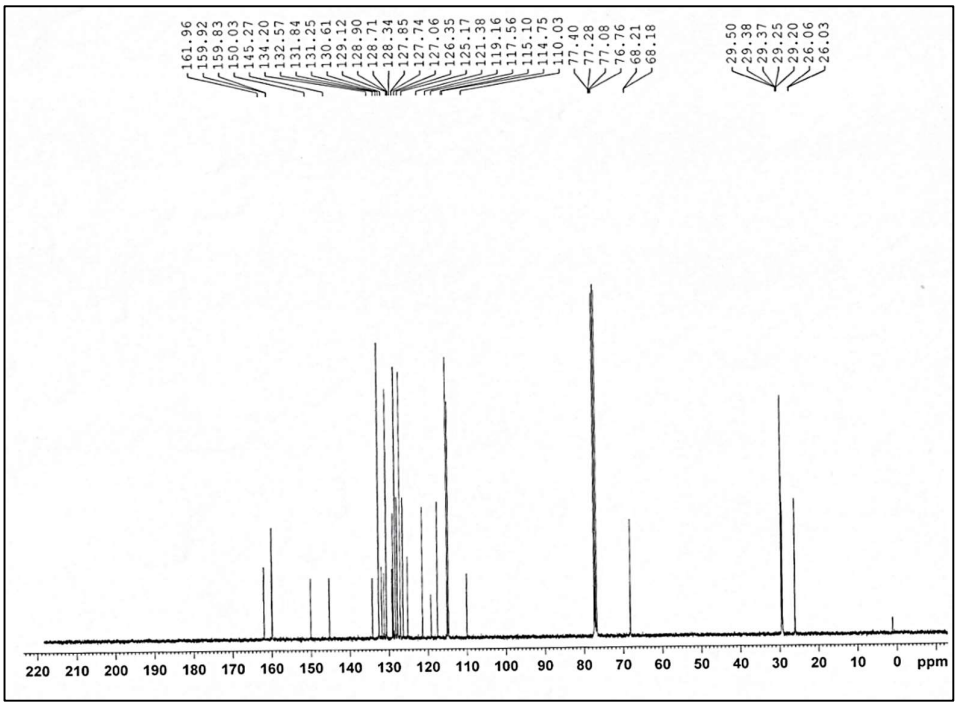

Fig. S4.54: ^{13}C-NMR spectra of *VI-10*

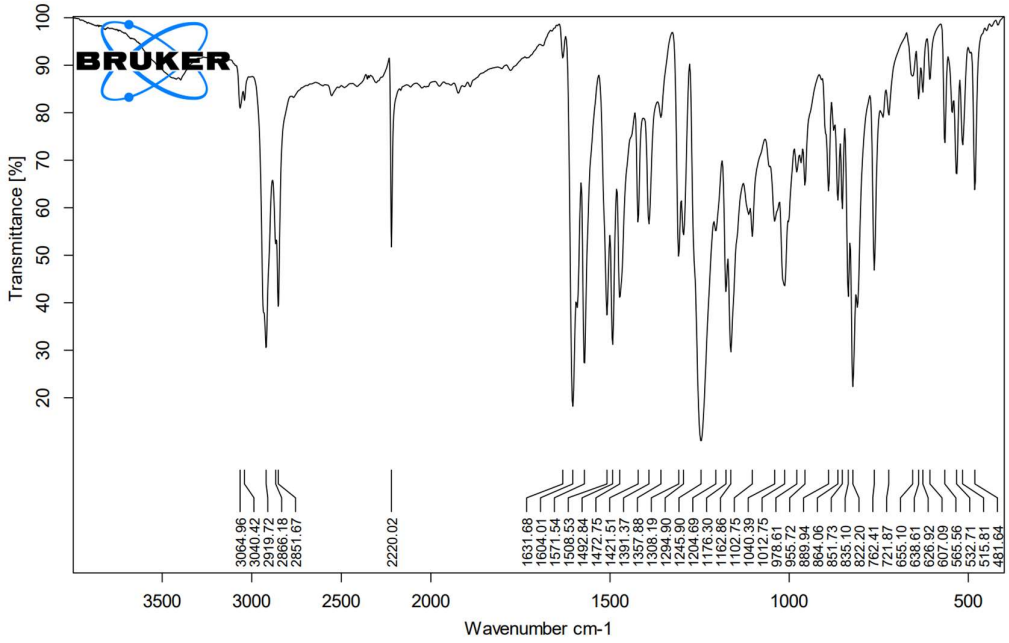

Fig. S4.55: FT-IR spectra of *VI-11*

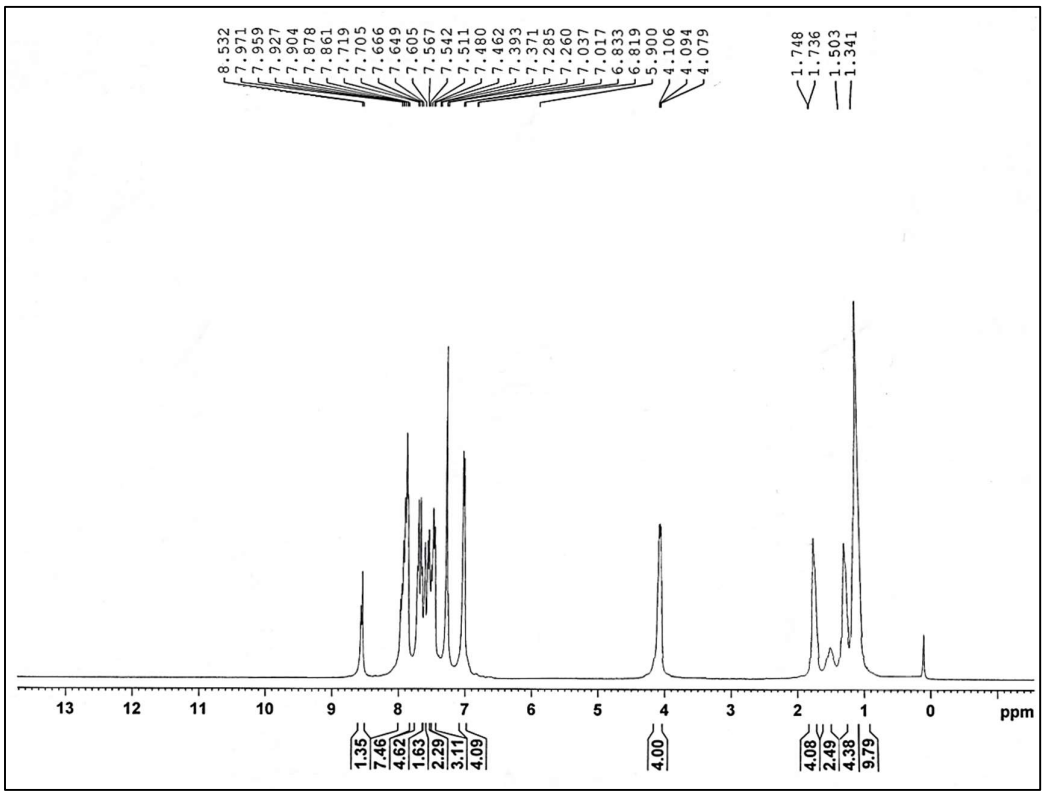

Fig. S4.56: ^{1}H-NMR spectra of *VI-11*

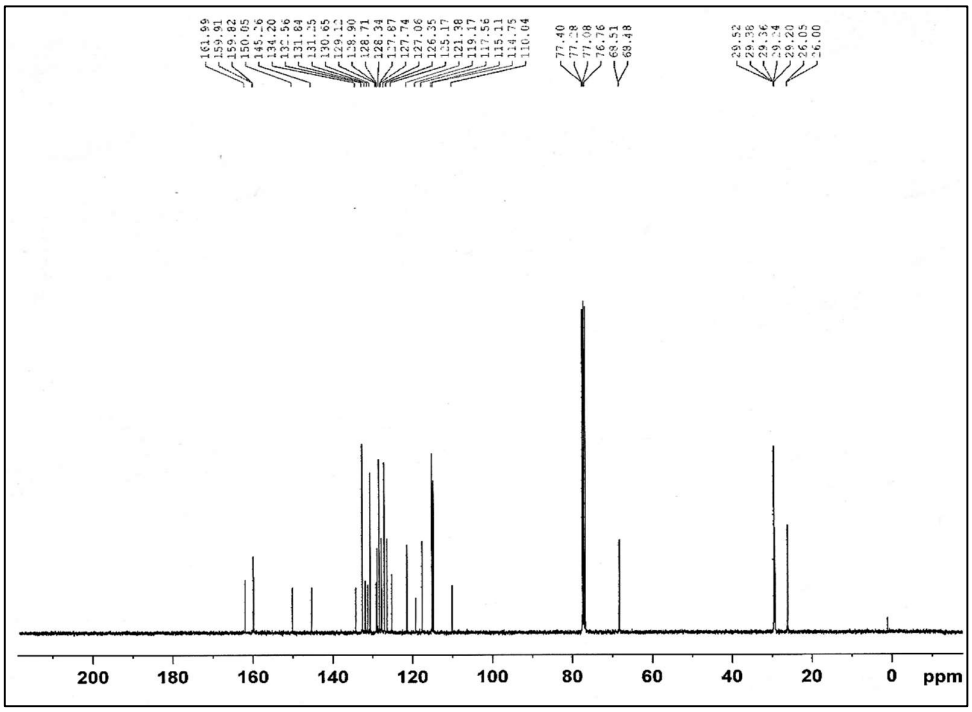

Fig. S4.57: ^{13}C-NMR spectra of *VI-11*

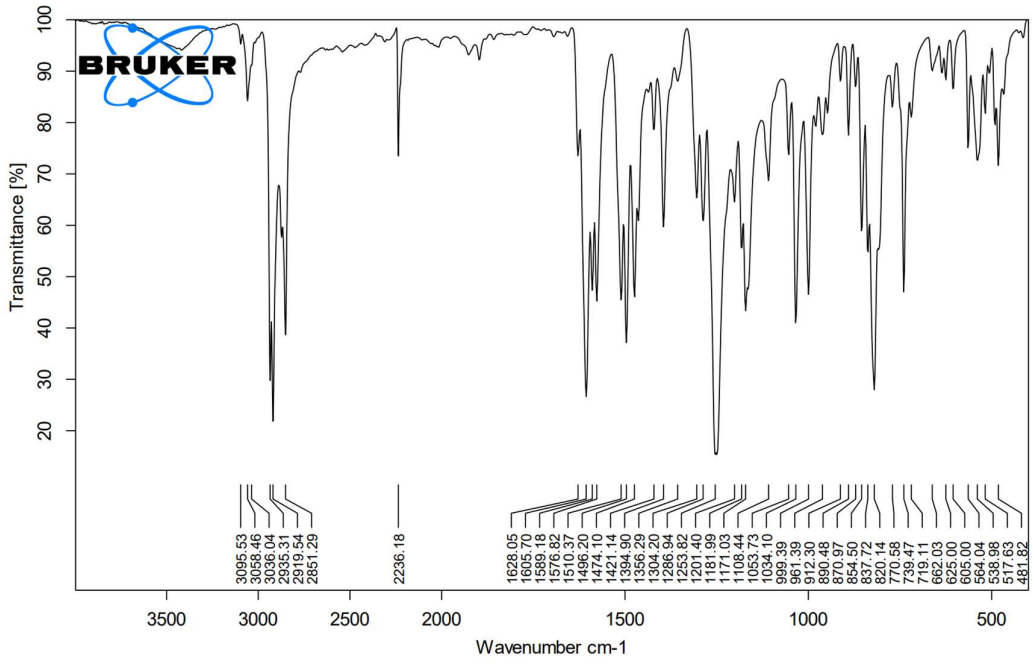

Fig. S4.58: FT-IR spectra of *VI-12*

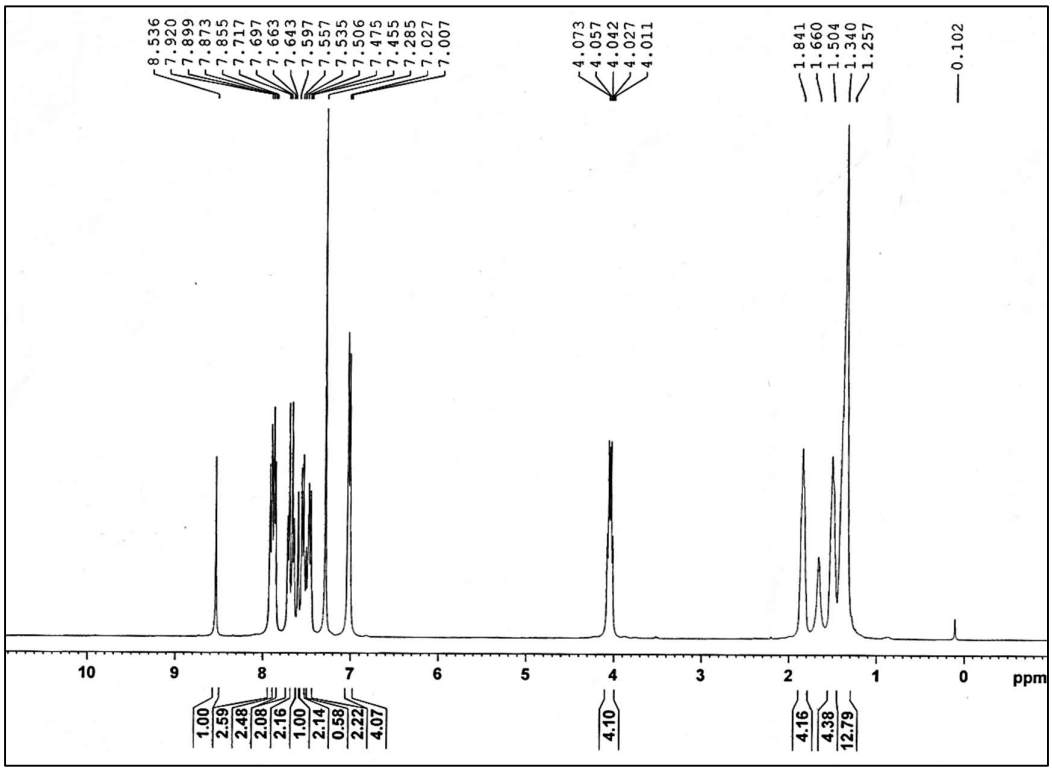

Fig. S4.59: ^{1}H-NMR spectra of *VI-12*

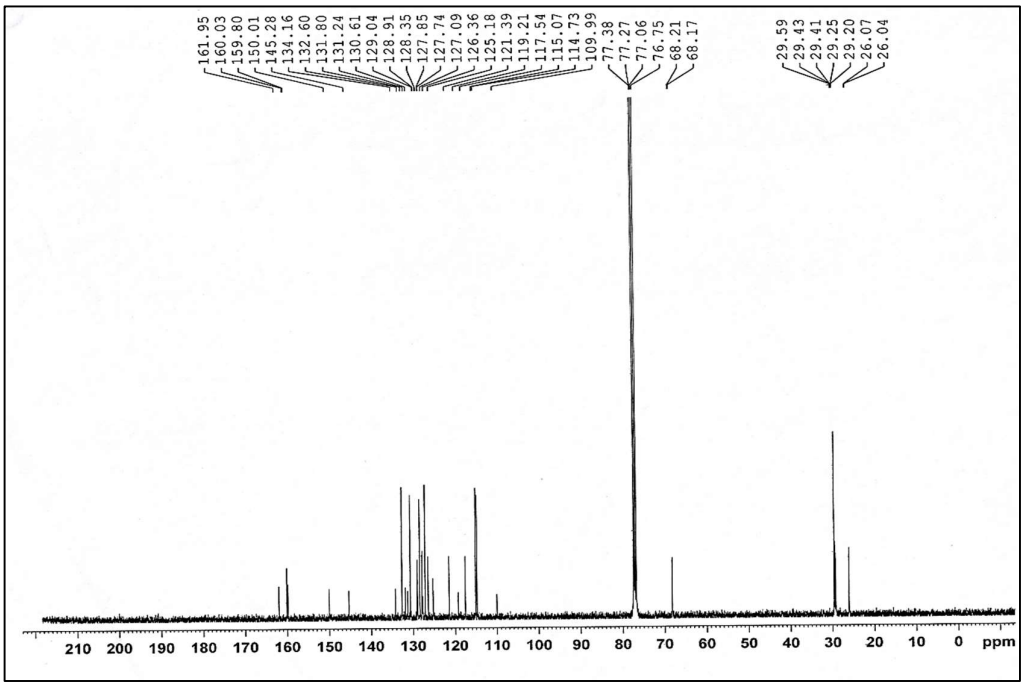

Fig. S4.60: ^{13}C-NMR spectra of *VI-12*

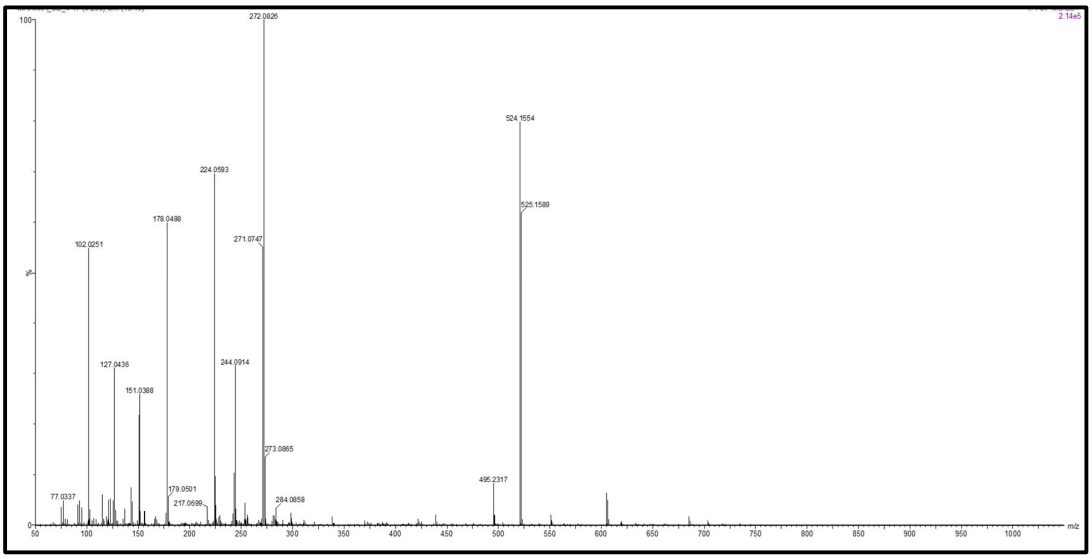

Fig. S4.61: ***Mass spectra of V-6***

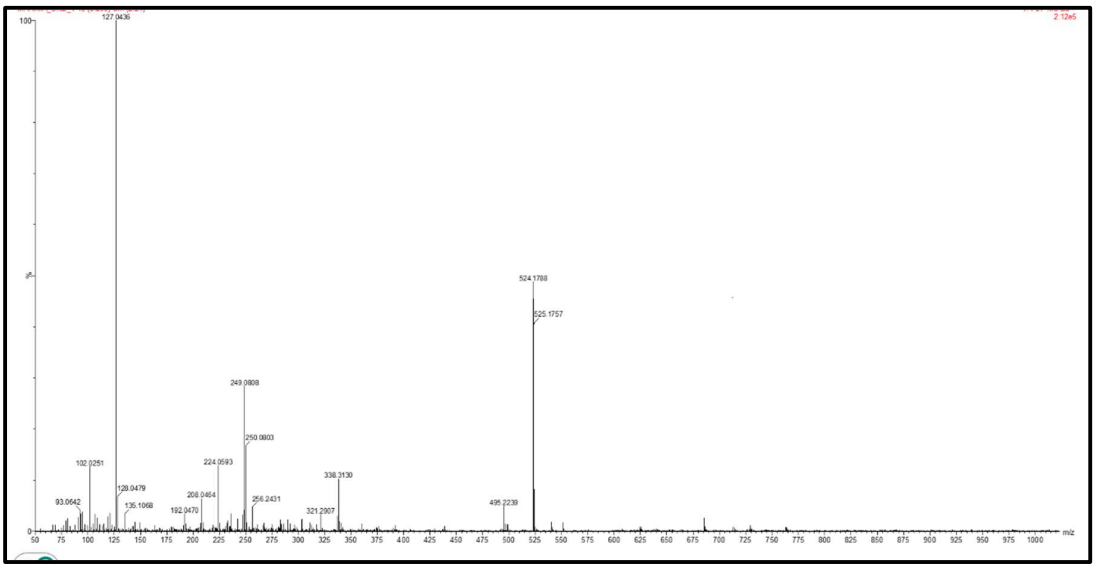

Fig. S4.62: ***Mass spectra of VI-6***

4.7 DSC thermograms of the prepared dimers

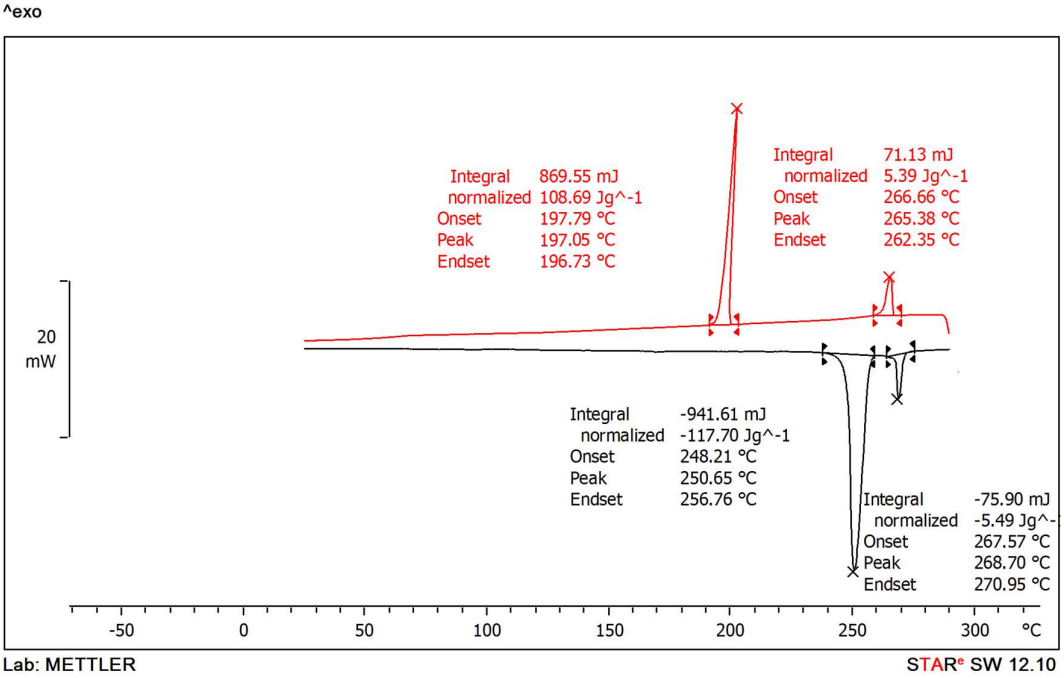

Fig. S4.63: DSC thermogram of *V-2*

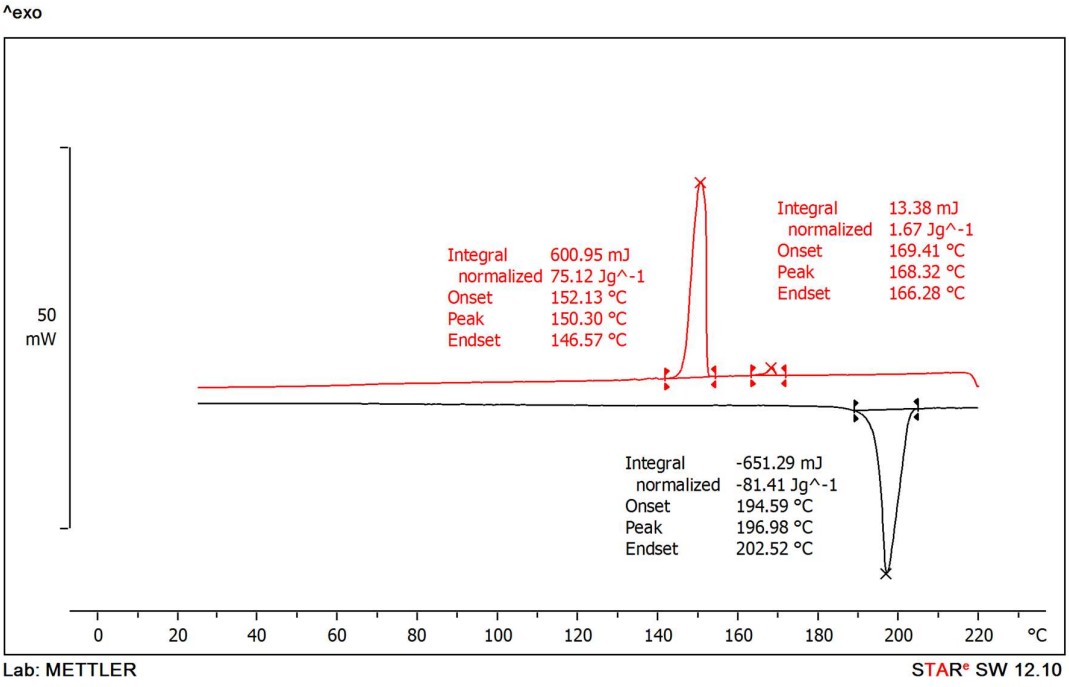

Fig. S4.64: DSC thermogram of *V-3*

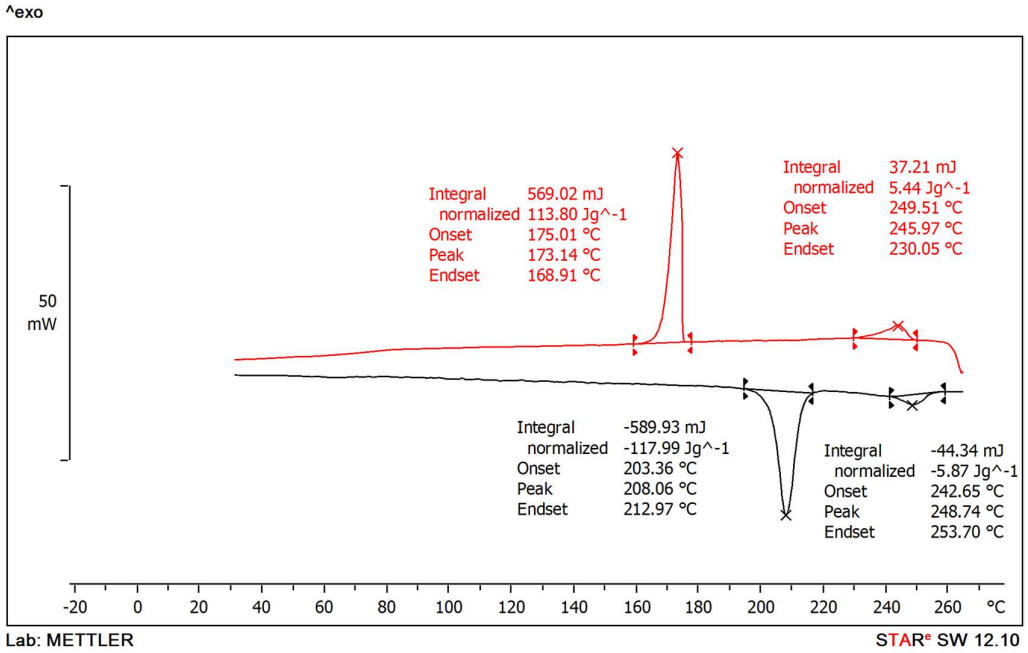

Fig. S4.65: DSC thermogram of *V-4*

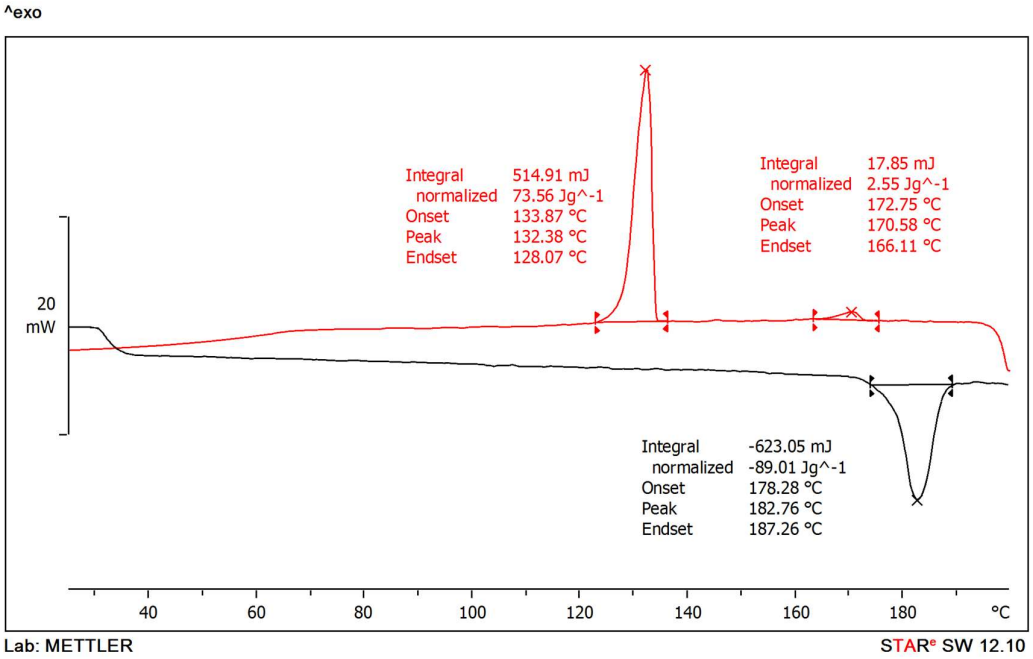

Fig. S4.66: DSC thermogram of *V-5*

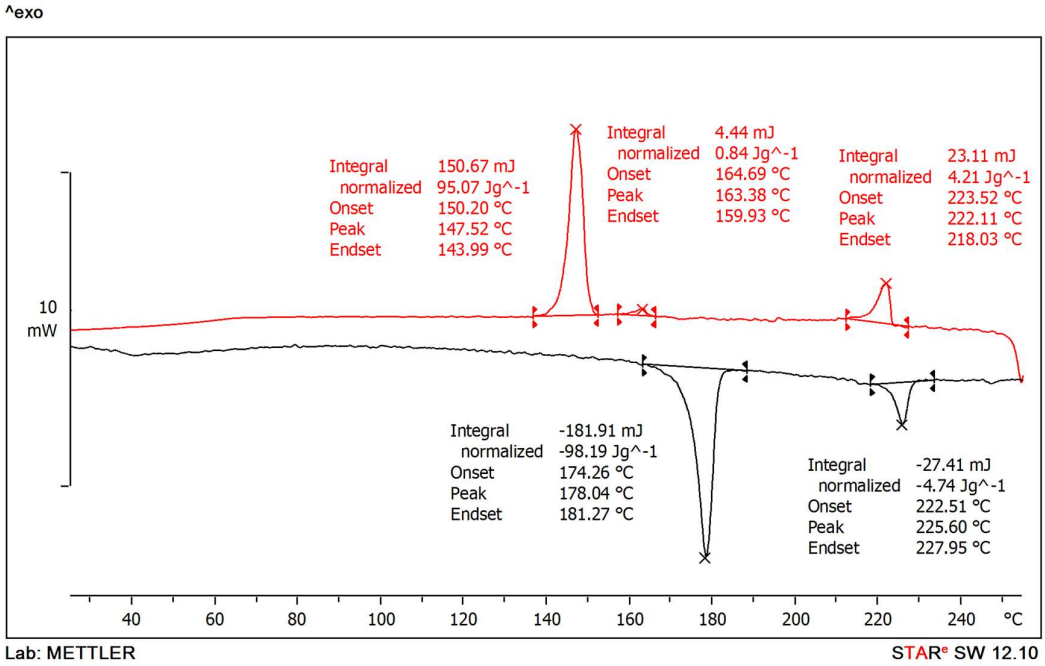

Fig. S4.67: DSC thermogram of *V-6*

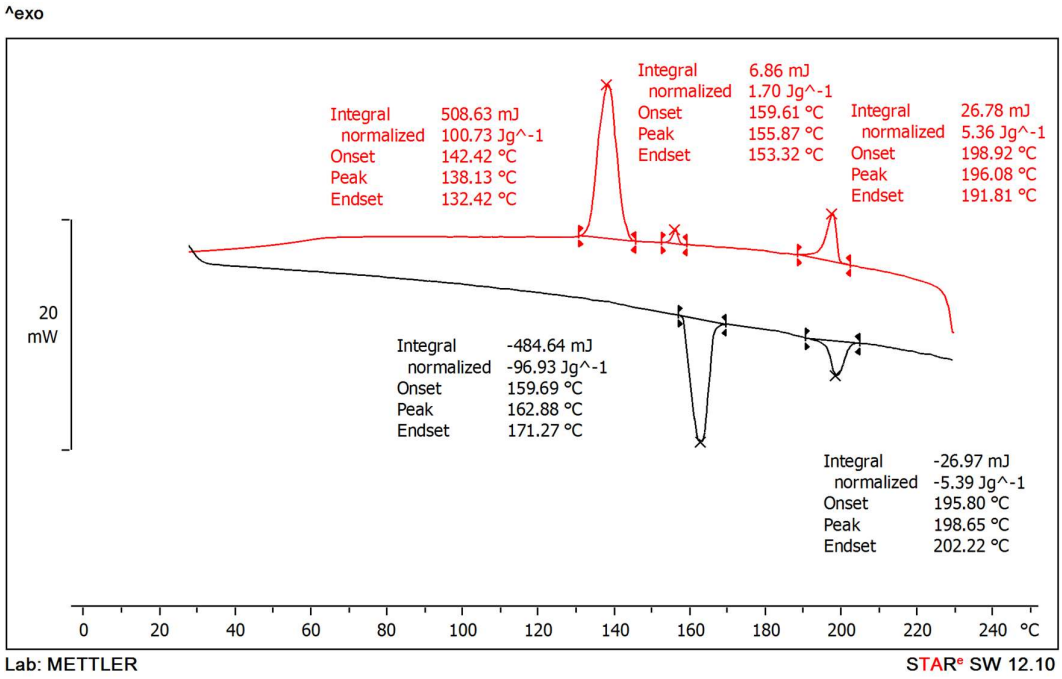

Fig. S4.68: DSC thermogram of *V-8*

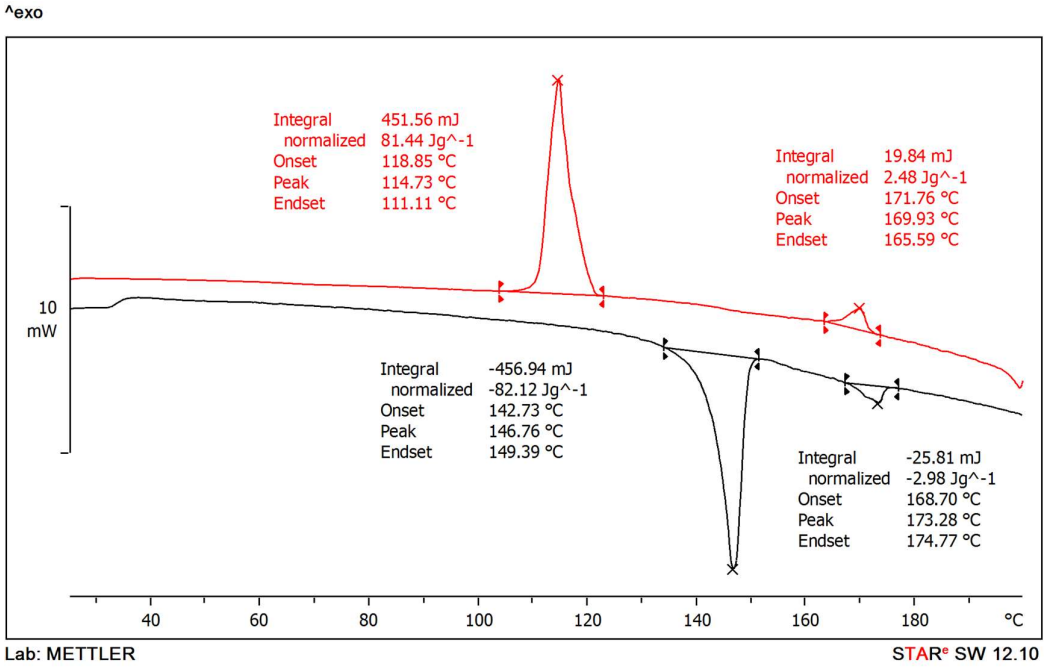

Fig. S4.69: DSC thermogram of *V-9*

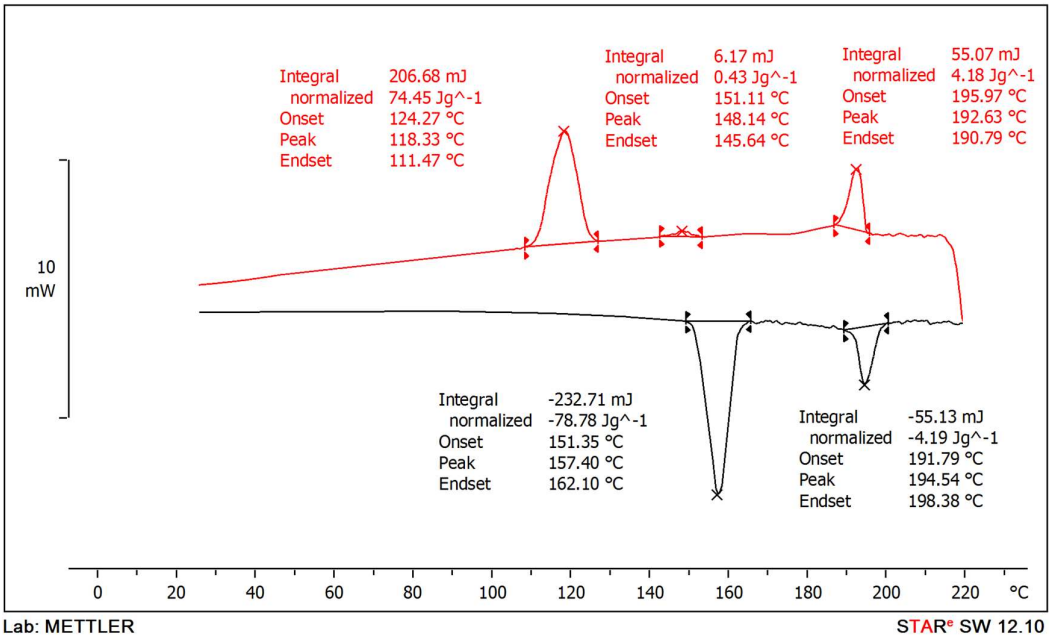

Fig. S4.70: DSC thermogram of *V-10*

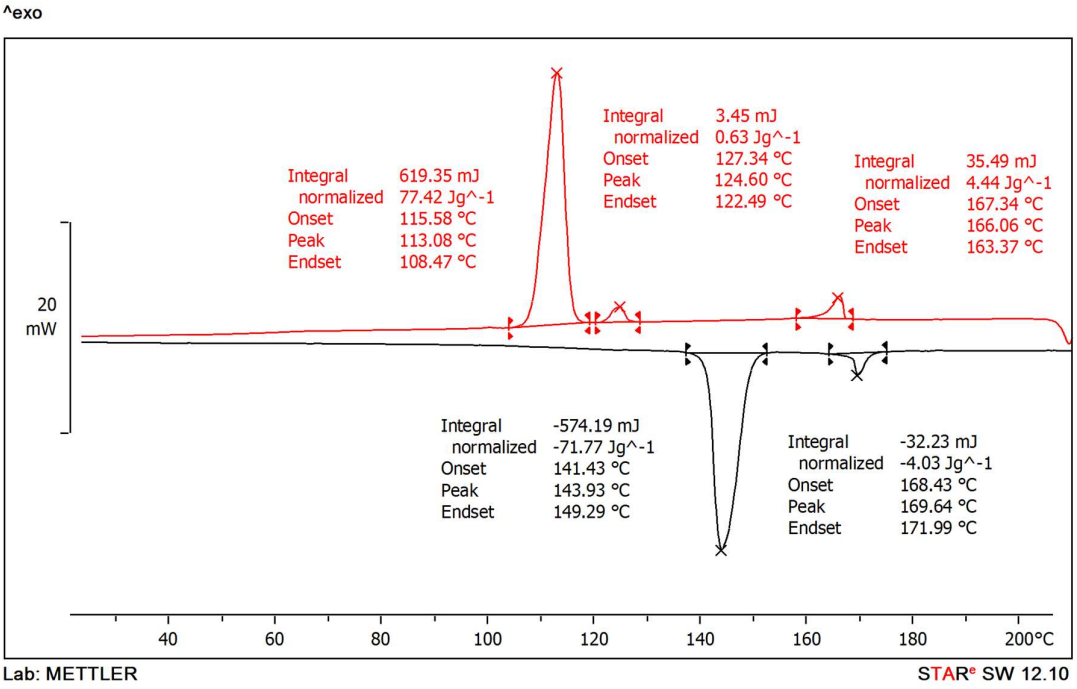

Fig. S4.71: DSC thermogram of *V-11*

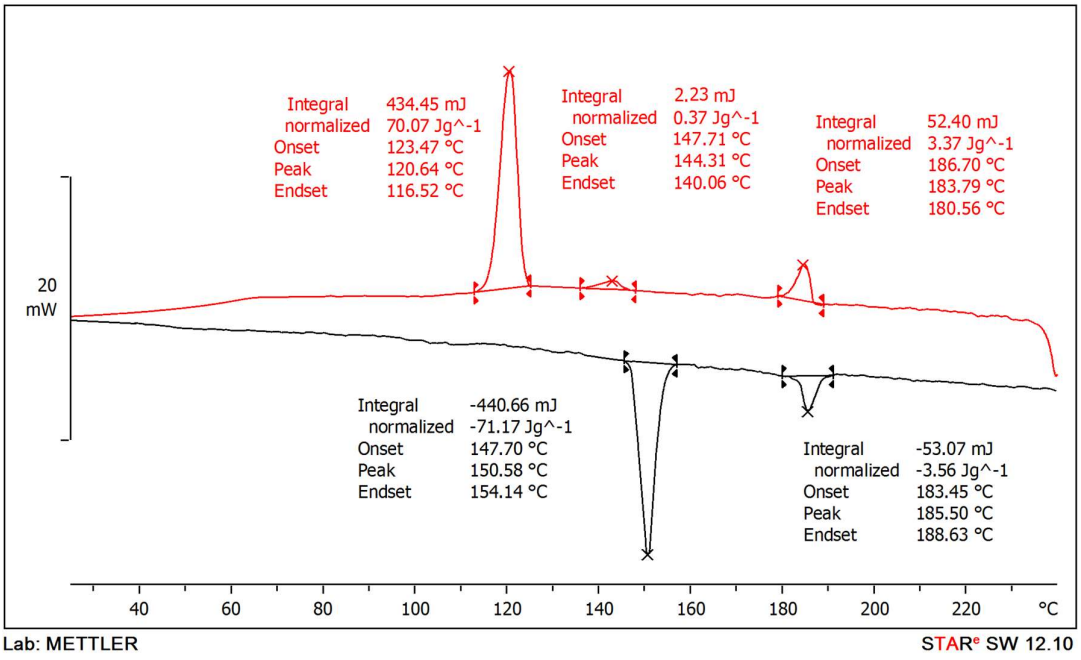

Fig. S4.72: DSC thermogram of *V-12*

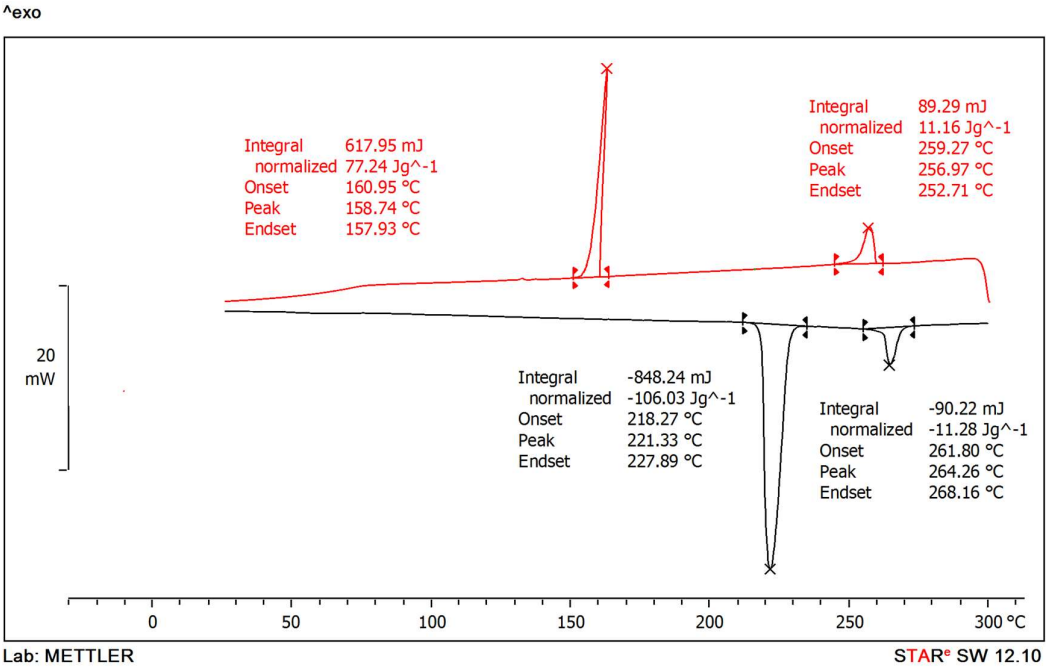

Fig. S4.73: DSC thermogram of *VI-2*

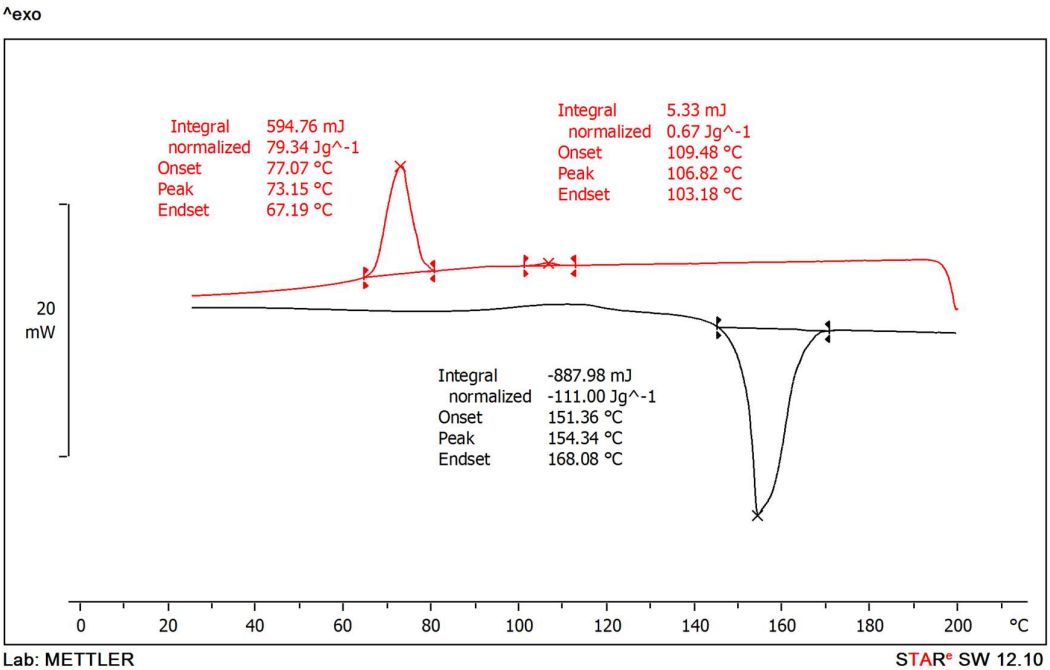

Fig. S4.74: DSC thermogram of *VI-3*

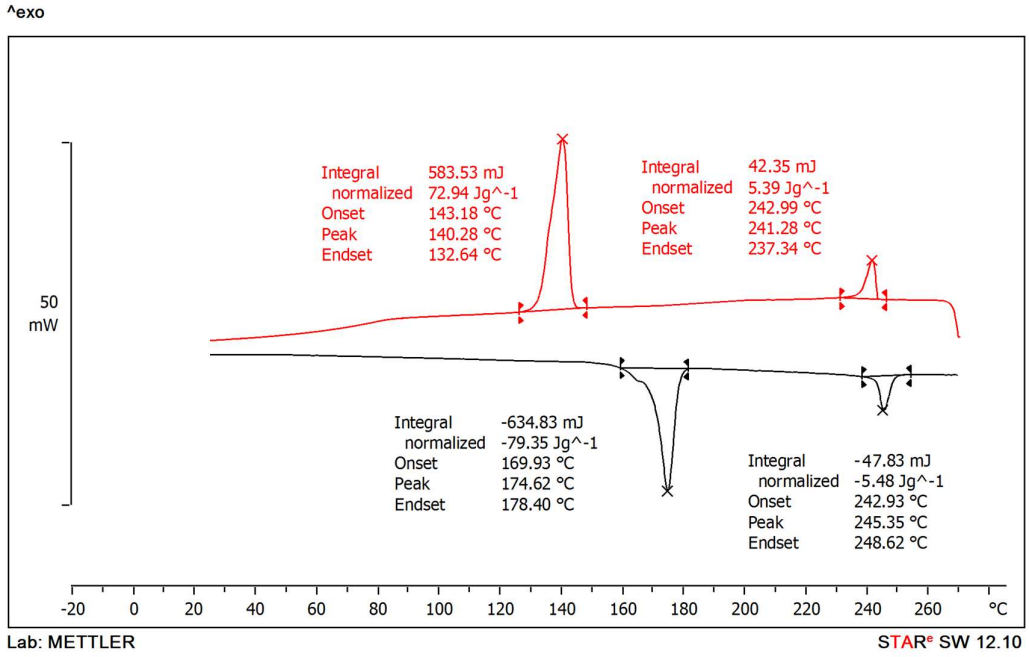

Fig. S4.75: DSC thermogram of *VI-4*

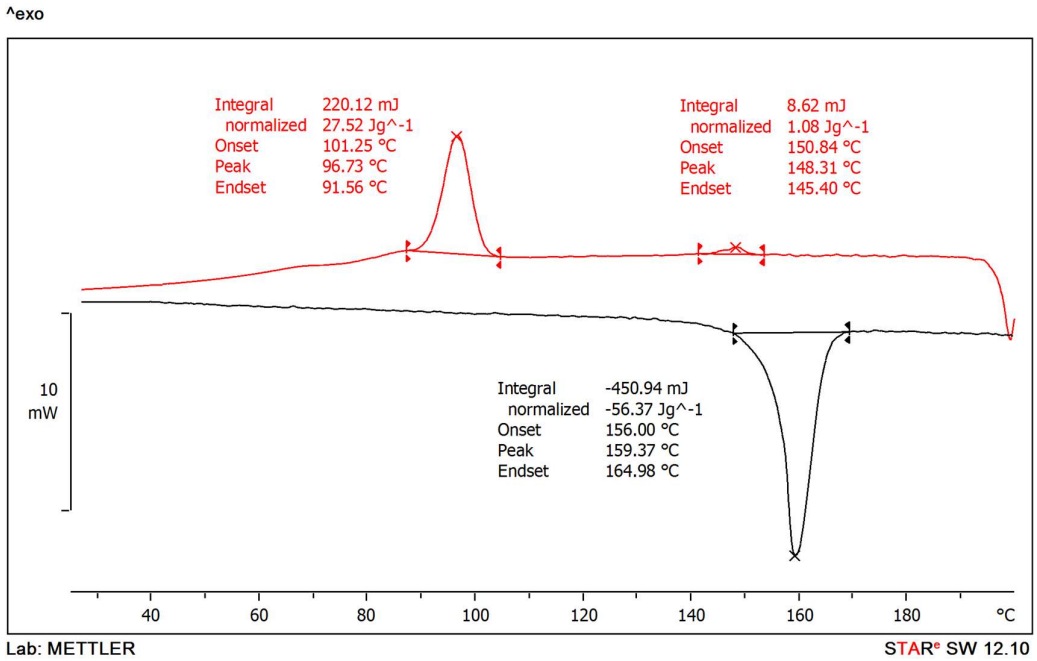

Fig. S4.76: DSC thermogram of *VI-5*

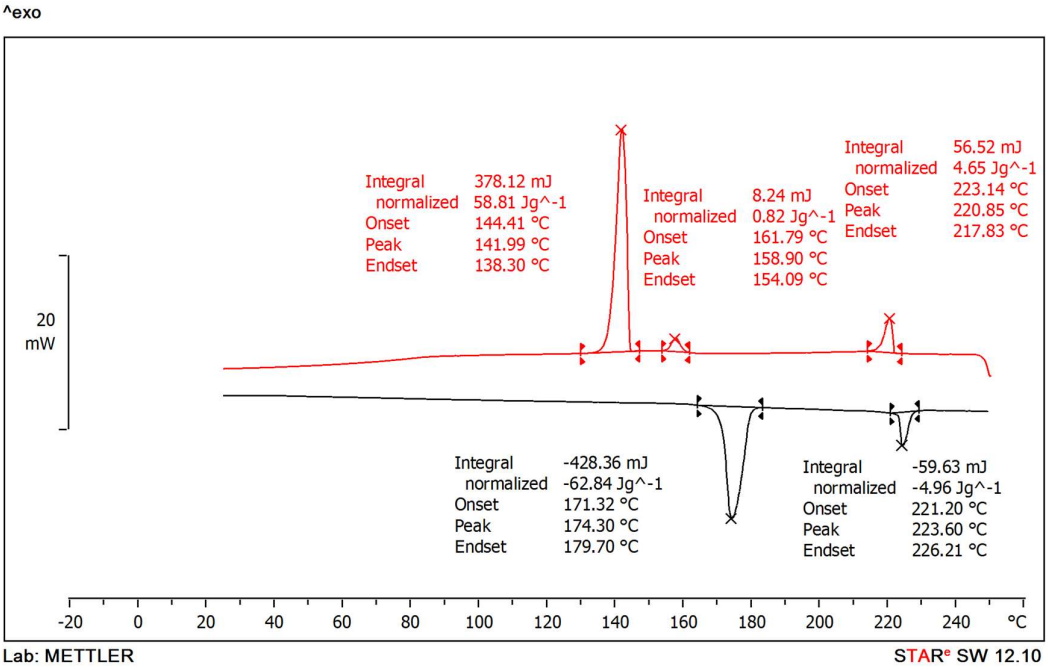

Fig. S4.77: DSC thermogram of *VI-6*

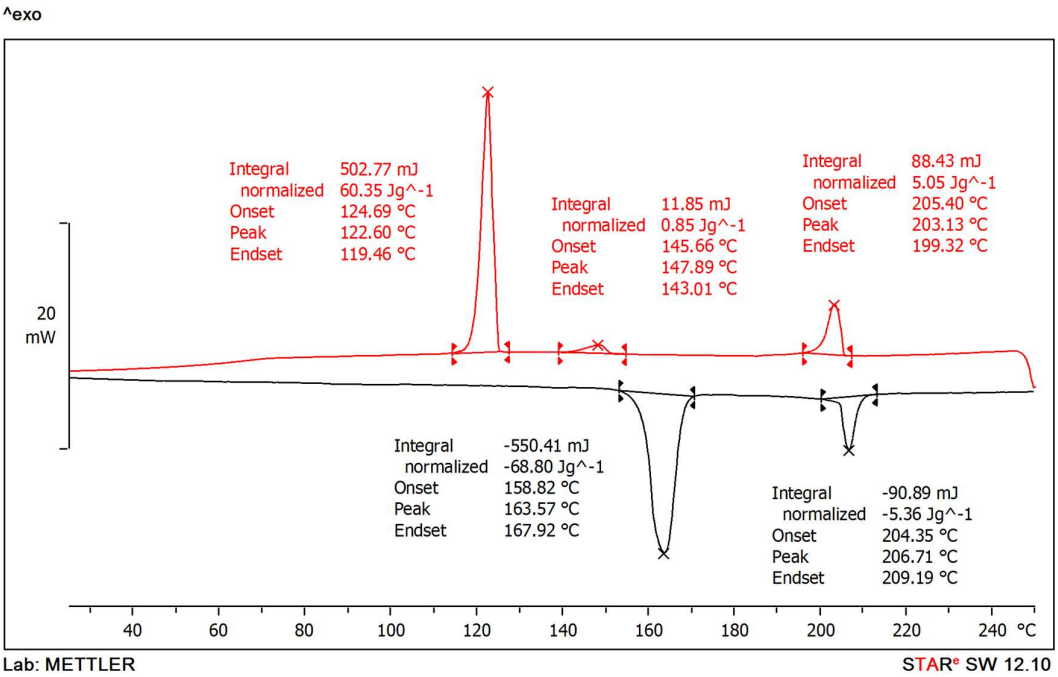

Fig. S4.78: DSC thermogram of *VI-8*

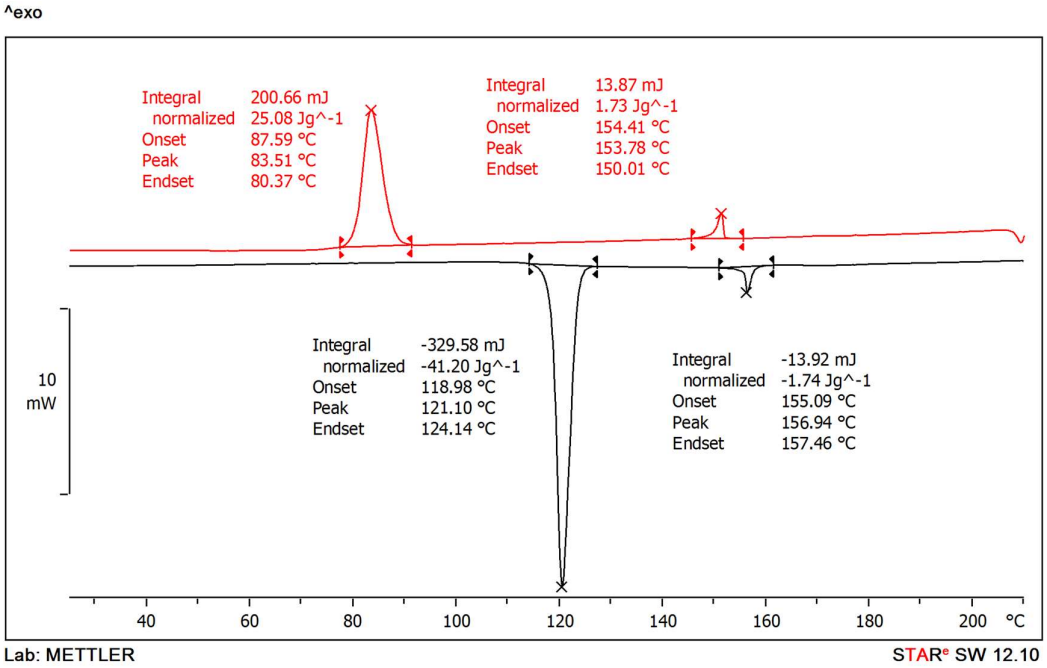

Fig. S4.79: DSC thermogram of *VI-9*

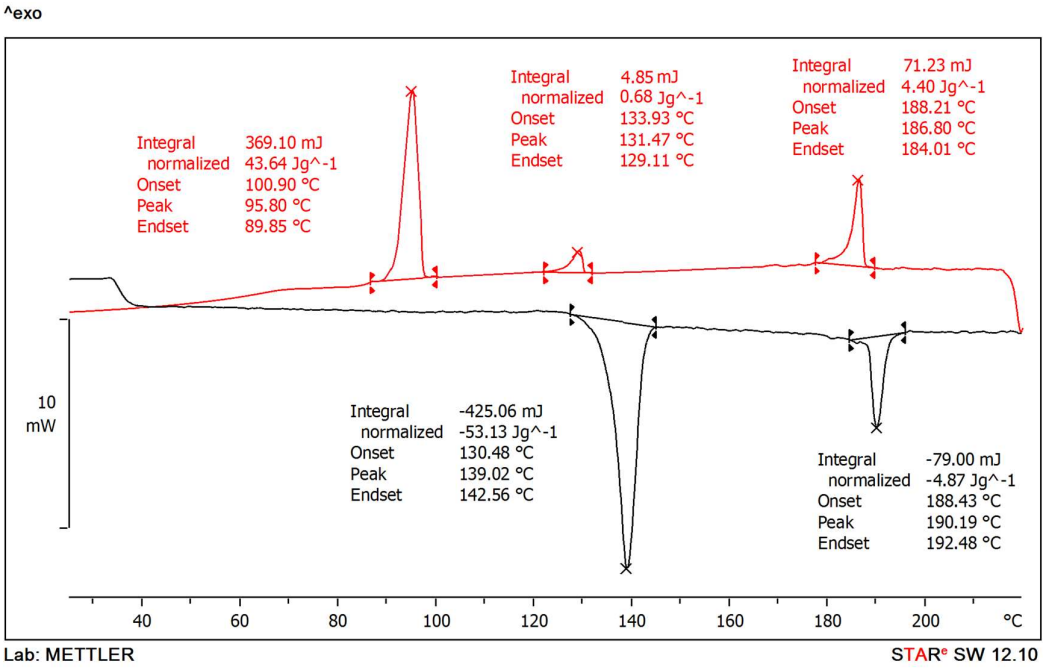

Fig. S4.80: DSC thermogram of *VI-10*

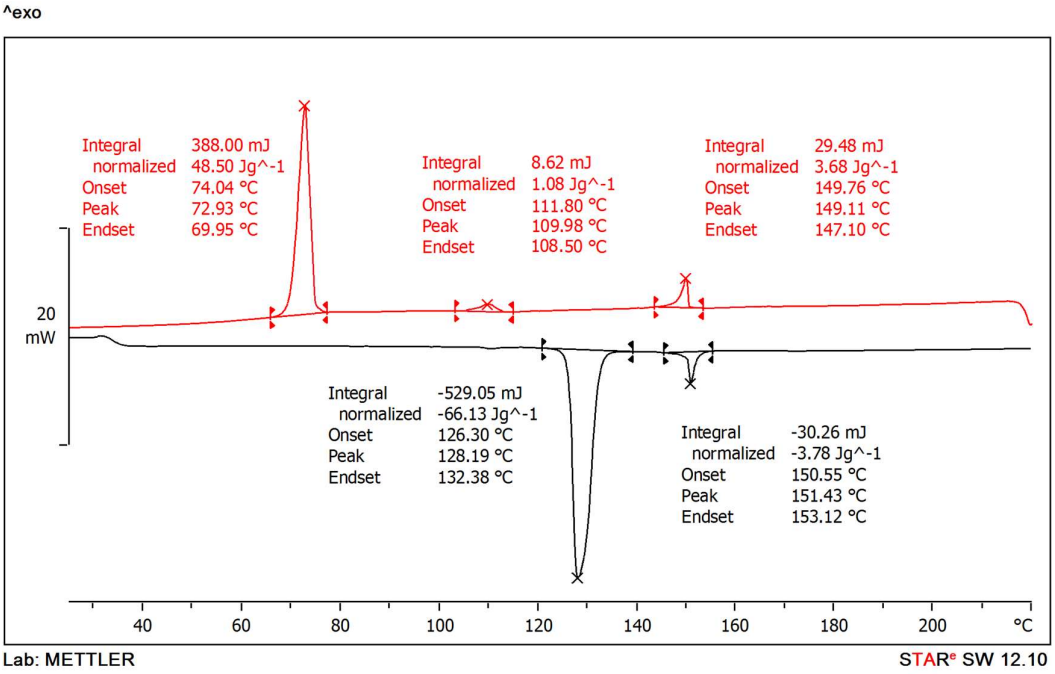

Fig. S4.81: DSC thermogram of *VI-11*

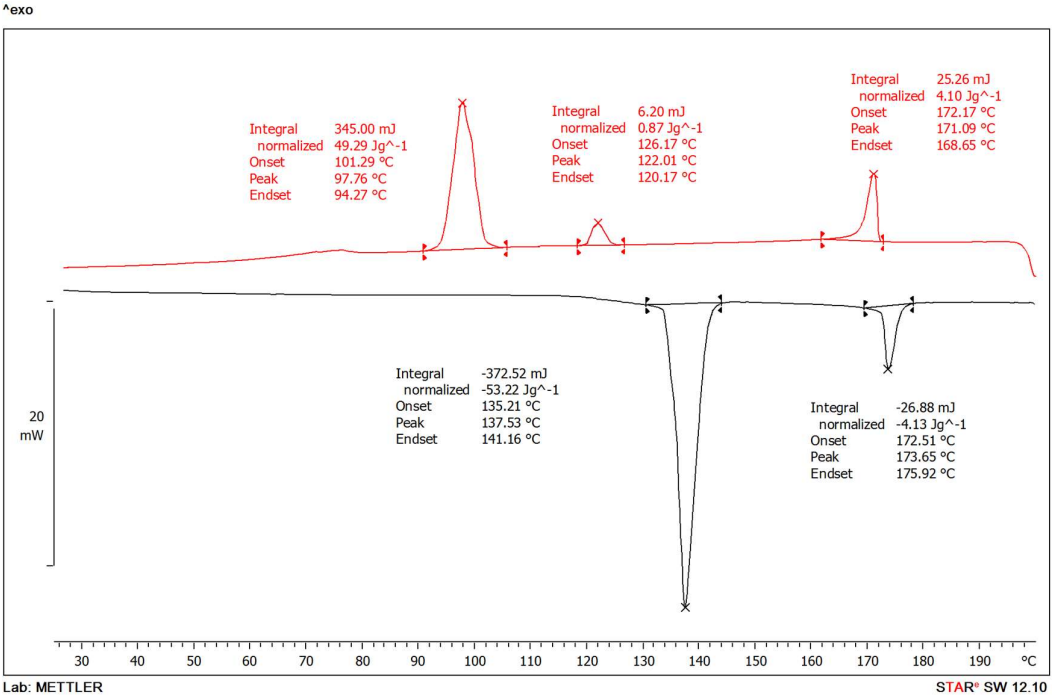

Fig. S4.82: DSC thermogram of *VI-12*

4.8 References

1 E. J. Davis, R. J. Mandle, B. K. Russell, P. Y. Foeller, M. S. Cook, S. J. Cowling and J. W. Goodby, *Liq. Cryst.*, 2014, **41**, 1635–1646.

2 K. Wang, P. Rai, A. Fernando, T. Szilvási, H. Yu, N. L. Abbott, M. Mavrikakis and R. J. Twieg, *Liq. Cryst.*, 2020, **47**, 3–16.

3 J. P. F. Lagerwall, *Liq. Cryst.*, 2024, **51**, 1296–1310.

4 G. W. Gray, *Mol. Cryst.*, 1969**, 7,** 127–151.

5 R. J. Mandle and J. W. Goodby, *RSC Adv.*, 2016, **6**, 34885–34893.

6 D. Dunmur, *Crystals*, 2022, **12**, 309.

7 I. Dozov, *Europhys. Lett.*, 2001, **56**, 247.

8 R. Memmer, *Liq. Cryst.*, 2002, **29**, 483–496.

9 V. P. Panov, M. Nagaraj, J. K. Vij, Y. P. Panarin, A. Kohlmeier, M. G. Tamba, R. A. Lewis and G. H. Mehl, *Phys. Rev. Lett.*, 2010, **105**, 167801.

10 Y. Cao, J. Feng, A. Nallapaneni, Y. Arakawa, K. Zhao, H. Zhang, G. H. Mehl, C. Zhu and F. Liu, *J. Mater. Chem. C*, 2021, **9**, 10020–10028.

11 V. Borshch, Y.-K. Kim, J. Xiang, M. Gao, A. Jákli, V. P. Panov, J. K. Vij, C. T. Imrie, M. G. Tamba, G. H. Mehl and O. D. Lavrentovich, *Nat. Commun.*, 2013, **4**, 2635.

12 D. Chen, J. H. Porada, J. B. Hooper, A. Klittnick, Y. Shen, M. R. Tuchband, E. Korblova, D. Bedrov, D. M. Walba, M. A. Glaser, J. E. Maclennan and N. A. Clark, *Proc. Natl. Acad. Sci.*, 2013, **110**, 15931–15936.

13 P. K. Challa, V. Borshch, O. Parri, C. T. Imrie, S. N. Sprunt, J. T. Gleeson, O. D. Lavrentovich and A. Jákli, *Phys. Rev. E*, 2014, **89**, 60501.

14 K. Merkel, B. Loska, Y. Arakawa, G. H. Mehl, J. Karcz and A. Kocot, *Int. J. Mol. Sci.*, 2022, **23**, 11018.

15 J. Zhou, W. Tang, Y. Arakawa, H. Tsuji and S. Aya, *Phys. Chem. Chem. Phys.*, 2020, **22**, 9593–9599.

16 M. P. Kumar, P. Kula and S. Dhara, *Phys. Rev. Mater.*, 2020, **4**, 115601.

17 D. A. Paterson, J. Xiang, G. Singh, R. Walker, D. M. Agra-Kooijman, A. Martínez-Felipe, M. Gao, J. M. D. Storey, S. Kumar, O. D. Lavrentovich and C. T. Imrie, *J. Am. Chem. Soc.*, 2016, **138**, 5283–5289.

18 J. P. Abberley, S. M. Jansze, R. Walker, D. A. Paterson, P. A. Henderson, A. T. M. Marcelis, J. M. D. Storey and C. T. Imrie, *Liq. Cryst.*, 2017, **44**, 68–83.

19 R. J. Mandle and J. W. Goodby, *RSC Adv.*, 2016, **6**, 34885–34893.

20 M. Šepelj, U. Baumeister, T. Ivšić and A. Lesac, *J. Phys. Chem. B*, 2013, **117**, 8918–8929.

21 N. Sebastián, D. O. López, B. Robles-Hernández, M. R. de la Fuente, J. Salud, M. A. Pérez-Jubindo, D. A. Dunmur, G. R. Luckhurst and D. J. B. Jackson, *Phys. Chem. Chem. Phys.*, 2014, **16**, 21391–21406.

22 T. Ivšić, M. Vinković, U. Baumeister, A. Mikleušević and A. Lesac, *RSC Adv.*, 2016, **6**, 5000–5007.

23 C. T. Archbold, E. J. Davis, R. J. Mandle, S. J. Cowling and J. W. Goodby, *Soft Matter*, 2015, **11**, 7547–7557.

24 K. Adlem, M., G. R. Luckhurst, A. Mertelj, O. Parri, R. M. Richardson, B. D. Snow, B. A. Timimi, R. P. Tuffin and D. Wilkes, *Phys. Rev. E*, 2013, **88**, 22503.

25 D. A. Paterson, M. Gao, Y.-K. Kim, A. Jamali, K. L. Finley, B. Robles-Hernández, S. Diez-Berart, J. Salud, M. R. de la Fuente, B. A. Timimi, H. Zimmermann, C. Greco, A. Ferrarini, J. M. D. Storey, D. O. López, O. D. Lavrentovich, G. R. Luckhurst and C. T. Imrie, *Soft Matter*, 2016, **12**, 6827–6840.

26 Z. Lu, P. A. Henderson, B. J. A. Paterson and C. T. Imrie, *Liq. Cryst.*, 2014, **41**, 471–483.

27 M. Cestari, S. Diez-Berart, D. A. Dunmur, A. Ferrarini, M. R. De Fuente, D. J. B. Jackson, D. O. Lopez, G. R. Luckhurst, M. A. Perez-Jubindo, R. M. Richardson, J. Salud, B. A. Timimi and H. Zimmermann, Phys Rev E 2011, **84,** 031704.

28 R. J. Mandle, E. J. Davis, S. A. Lobato, C.-C. A. Vol, S. J. Cowling and J. W. Goodby, *Phys. Chem. Chem. Phys.*, 2014, **16**, 6907–6915.

29 R. J. Mandle, C. C. A. Voll, D. J. Lewis and J. W. Goodby, *Liq. Cryst.*, 2016, **43**, 13–21.

30 A. A. Dawood, M. C. Grossel, G. R. Luckhurst, R. M. Richardson, B. A. Timimi, N. J. Wells and Y. Z. Yousif, *Liq. Cryst.*, 2017, **44**, 106–126.

31 Y. Arakawa, K. Komatsu, T. Shiba and H. Tsuji, *Mater. Adv.*, 2021, **2**, 1760–1773.

32 D. Wang, J. Liu, W. Zhao, Y. Zeng, J. Huang, J. Fang and D. Chen, *Chem. Eur. J.*, 2022, **28**, 70.

33 M. Alaasar and C. Tschierske, *Liq. Cryst.*, 2017, **44**, 387–393.

34 T. Hirose and A. Yoshizawa, *J. Mater. Chem. C*, 2016, **4**, 8565–8574.

35 H. T. Srinivasa and L. M. Rahman, *Liq. Cryst.*, 2024, **51**, 1610–1616.

36 H. T. Srinivasa, B. S. Palakshamurthy and M. A. Venkatesha, *Mater. Today Proc.*, 2019, **17**, 41–50.

37 K. Wang, M. S. Rahman, T. Szilvási, J. I. Gold, N. Bao, H. Yu, N. L. Abbott, M. Mavrikakis and R. J. Twieg, *Liq. Cryst.*, 2021, **48**, 672–688.

38 D. A. Paterson, R. Walker, J. P. Abberley, J. Forestier, W. T. A. Harrison, J. M. D. Storey, D. Pociecha, E. Gorecka and C. T. Imrie, *Liq. Cryst.*, 2017, **44**, 2060–2078.

39 D. A. Paterson, R. Walker, J. M. D. Storey and C. T. Imrie, *Liq. Cryst.*, 2023, **50**, 725–736.

40 Y. Arakawa, K. Komatsu, Y. Ishida and H. Tsuji, *Liq. Cryst.*, 2021, **48**, 641–652.

41 R. Walker, M. Majewska, D. Pociecha, A. Makal, J. M. D. Storey, E. Gorecka and C. T. Imrie, *ChemPhysChem*, 2021, **22**, 461–470.

42 A. E. Blatch, I. D. Fletcher and G. R. Luckhurst, *J. Mater. Chem.*, 1997, **7**, 9–17.

43 R. Walker, D. Pociecha, C. Faidutti, E. Perkovic, J. M. D. Storey, E. Gorecka and C. T. Imrie, *Liq. Cryst.*, 2022, **49**, 969–981.

44 A. F. Alshammari, D. Pociecha, R. Walker, J. M. D. Storey, E. Gorecka and C. T. Imrie, *Soft Matter*, 2022, **18**, 4679–4688.

45 E. Cruickshank, R. Walker, G. J. Strachan, C. H. F. Goode, M. M. Majewska, D. Pociecha, E. Gorecka, J. M. D. Storey and C. T. Imrie, *J. Mol. Liq.*, 2023, **391**, 123226.

46 Y. Arakawa, Y. Ishida, K. Komatsu, Y. Arai and H. Tsuji, *Tetrahedron*, 2021, **95**, 132351.

47 N. Éber, Á. Buka and K. S. Krishnamurthy, *Liq. Cryst.*, 2022, **49**, 1194–1222.

48 R. Walker, M. Majewska, D. Pociecha, A. Makal, J. Storey, E. Gorecka and C. Imrie, *ChemPhysChem*, 2021, **22,** 461-470.

49 M. Pande, P. K. Tripathi, S. K. Gupta, R. Manohar and S. Singh, *Liq. Cryst.*, 2015, **42**, 1465–1471.

50 S.-T. Wu, U. Efron and L. D. Hess, *Appl. Opt.*, 1984, **23**, 3911–3915.

51 E. E. Zavvou, E. Ramou, Z. Ahmed, C. Welch, G. H. Mehl, A. G. Vanakaras and P. K. Karahaliou, *Soft Matter*, 2023, **19**, 9224–9238.